Design of Liquid Cold Plates for Thermal Management of DC-DC Converters in Aerospace Applications

DESIGN OF LIQUID COLD PLATES FOR THERMAL MANAGEMENT OF DC-DC CONVERTERS IN AEROSPACE APPLICATIONS

BY

ROBERT VANGOOLEN, B.Sc.

A THESIS

SUBMITTED TO THE DEPARTMENT OF MECHANICAL ENGINEERING

AND THE SCHOOL OF GRADUATE STUDIES

OF MCMASTER UNIVERSITY

IN PARTIAL FULFILMENT OF THE REQUIREMENTS

FOR THE DEGREE OF

Master of Applied Science

Master of Applied Science (2022) McMaster University

(Mechanical Engineering) Hamilton, Ontario, Canada

TITLE:	Design of Liquid Cold Plates for Thermal Management of DC-DC Converters in Aerospace Applications
AUTHOR:	Robert Vangoolen B.Tech, McMaster University, Hamilton, ON, Canada
SUPERVISOR:	Dr. Ali Emadi
NUMBER OF PAGES:	xv, 173

Abstract

Due to increasing power demands and decreasing component size, thermal management has become the bottleneck for many power electronic applications. The aerospace industry has focused on reducing weight, operating temperature, and pumping power of power converters since these will limit an aircrafts' range and load-carrying capacity. This paper outlines a tool created in MATLAB to automate the cold plate design process for DC-DC converters (or similar applications). The tool incorporates a genetic algorithm to find the optimal aligned or staggered pin fin configuration that maintains the devices below their critical junction temperature while reducing the system's overall weight and pressure drop.

Utilizing this MATLAB design tool, a cold plate was designed, manufactured, and tested. The convection coefficient calculated within MATLAB (via empirical correlations) was verified using simplified CFD simulations within 5% of each other. The same CFD setup, boundary condition types, and methodology are then applied for the full-sized prototype cold plate simulations. These simulations were then validated using the experimental results. For all cases, the percentage error between the simulated convection coefficient values (CFD) and the experimental results was less than 12%. The experiments' measured surface temperature and pressure drop errors were less than 8% off the predicted CFD results.

Therefore, the MATLAB tool and its correlations/calculations could be verified (via CFD) and validated (experimentally) based on good agreement between the CFD and the experimental results. This three-pronged approach (analytical calculations, CFD simulations, and experimental validation) is an effective and robust method to solve heat transfer problems.

Overall, with the framework outlined in this thesis, a complete cold plate design can now be completed in weeks instead of months. This streamlined approach will save companies significant time and money in the design and simulation phases, making this tool a valuable addition to the current literature available.

Acknowledgments

I want to thank my supervisor Dr. Ali Emadi for his guidance and support throughout the Master's program. I also want to thank Dr. Romina Rodriquez for her help and support throughout my project with the day-to-day activities. She was instrumental in keeping me motivated and on track to finish my thesis in a timely manner.

I also want to thank my friends and colleagues at McMaster Automotive Resource Center (MARC), who were a constant encouragement throughout the project. I want to especially thank the thermal team at MARC, who were constantly willing to answer my questions and guide me through the design process.

Next, I want to thank Mario Cruz from Eaton Aerospace and his team for their collaboration and helpfulness. They provided essential support and guidance throughout this project and helped me stay accountable. This research was undertaken, in part, thanks to funding from Eaton Aerospace and Mitacs Accelerate Program.

Lastly, I want to thank my family and friends for their constant support throughout my years of undergrad and graduate studies. Without their love, support, and encouragement, none of this would have been possible.

Contents

List of Figures

List of Tables

Chapter 1

Introduction

1.1 Background and Motivation

As power density requirements for DC-DC converters increase, there is a constant push to minimize the power losses, volume, weight, and costs as much as possible [1]. To accomplish this, the aerospace and automotive industries continue to implement high-powered electronic devices in a wide variety of electronics packages. Some typical examples include Metal-Oxide-Semiconductor Field-Effect Transistors (MOSFET), Insulated Gate Bipolar Transistors (IGBT), Gate Turn-Off Transistors (GTO), and Silicon Controlled Rectifiers (SCR). As power density demands for these devices continue to increase rapidly, so do the thermal management requirements. Companies are implementing devices with increasing power dissipation and reduced device size, increasing demand for the cooling system's capabilities [2]. For this reason, thermal management is often the bottleneck that prevents an increase in power output for electronics packages.

To solve this thermal management issue, advanced designs and technologies should

be implemented to remove high component heat fluxes. This higher heat removal improves the electronics' longevity and minimizes the risk of failure since the number one failure of electronics is overheating. Foreign object debris (FOD), humidity, and vibrations make up most other electronic component premature failures [2].

The thermal management system employed will depend primarily on power dissipation and the packaging constraints. If natural convection can provide sufficient cooling, this would be ideal since it will have the fewest mechanical components, and leakage and other issues related to fluid flow cannot occur. If, however, natural convection cannot keep the device junction temperature below a specific pre-determined limit, forced air convection is the second-best option (with respect to ease of implementation and overall simplicity). The added cooling ability is due to the induced air velocity across the device surfaces. If forced air convection is insufficient, it is necessary to explore liquid-cooled solutions. Since water is a significantly better heat transporter than air, more heat gets removed from a liquid-cooled system. However, this does have drawbacks as liquid-cooled solutions typically require a cooling loop with a pump and heat removal devices such as a cold plate, heat sink, or heat exchanger. When implementing liquid cooling, issues can also arise involving corrosion, leakage, and flow maldistribution.

The cold plate is a well-researched and effective means of heat removal for an electronics system. There are a wide variety of different types of cold plates, each one unique for specific applications. However, all cold plates follow basic design principles. These principles involve creating a confined flow space between bounding metallic walls [3]. This fluid flow will be the primary mechanism through which the heat removal will occur.

1.2 Publications

"Cold Plate Tool Development for Power Electronics in Aerospace Applications." Presented at IEEE Transportation Electrification Conference (ITEC) in 2021.

1.3 Research Objectives

This thesis's main objective is to create a baseline design tool in MATLAB, through which a cold plate may be created from scratch. The aim is to reduce the initial amount of design, computational, and simulation work required to complete this objective. This thesis walks through this entire design process from conception to completion and provides a valuable framework for anyone implementing a cold plate design in the future. Instead of just creating a theoretical design tool, the tool was implemented to design a prototype cold plate, including manufacturing and testing. This implementation ensures that the MATLAB tool created is functional, applicable, and valuable for cold plate design. The tool gives basic and preliminary performance metrics such as junction temperature, convection coefficient, pressure drop, pumping power, and more to assist a thermal engineer with design.

This thesis illustrates and compares the differences between staggered and aligned fin configuration for analysis. Each configuration includes step-by-step equations, giving future designers an easy-to-follow methodology. Once the configuration is selected, all corresponding simulation work is shown. These simulations can provide valuable insight for future designers on what to look for within simulations, typical boundary conditions, and how to ensure accuracy. Minimal information was available in this respect regarding cold plate design specifically. If this information had been

available in one concise location at the start of this thesis, the lead time could have been drastically reduced. Therefore this thesis hopes to provide this framework to assist designers in the future.

Lastly, the thesis investigates several different manufacturing methods and when one might opt to use a specific type. Manufacturing is critical to keep in mind because the best thermal design in the world is useless if it is not manufacturable. During design, complexity and performance must be balanced carefully to propose a manufacturable, cost-effective design with good performance characteristics.

1.4 Thesis Outline

Chapter 2 starts by exploring why the cold plate was chosen. This reasoning goes back to the basics of conventional cooling techniques. Natural convection and forced convection (air) should be explored first since they are the easiest and cheapest to implement when creating any cooling system. However, if higher heat flux removal is required, liquid cooling is often the way to go. Liquid cooling was broken down into indirect and direct cooling, which are explored in this chapter. After this, some state-of-the-art cooling options are explored, including directly integrated cooling, double-sided cooling, and additional heat enhancement techniques. Some weight reduction methods are then explored, including some optimization techniques to improve the performance of cooling systems.

Chapter 3 looks at the design and manufacturing of cold plates specifically since a cold plate design was implemented. This chapter includes selecting the materials that make up a thermal package and their importance. Then this chapter discusses some typical manufacturing methods and their applicability for cold plates. Some

concerns and considerations which the designer should be aware of are also outlined in this chapter. Next, inlet and outlet geometry and the effect these locations play on the design are explored. Lastly, this chapter also considers flow maldistribution, and some mitigation techniques are outlined.

Chapter 4 explores the MATLAB tool created for cold plate design. It starts by going through all relevant equations and correlations. Next, the specifics of the tool are discussed in terms of the thermal model and optimization algorithm used. Then the specific design requirements for the cold plate design are outlined. These requirements include device layouts, power dissipation, inlet/outlet locations, weight requirements, and more. Lastly, the MATLAB tool was run, a prototype was created, and all design aspects and 3D geometry are shown in this section.

Chapter 5 goes into detail about the simulations that were conducted. These include two sets of simulations; 1) to verify the convection coefficient between MATLAB and CFD for a simplified model and 2) to calculate the convection coefficient, pressure drop, and surface temperature of the prototype cold plate. All meshing, boundary conditions, solution monitors, and relevant parameters are considered in these sections.

Chapter 6 discusses the prototype cold plate manufacturing, assembly process, and experimental test setup. This chapter includes all components in the experimental setup and a complete description of the tests to be conducted. Lastly, the experimental results are recorded and compared to the CFD results obtained in chapter 5.

Chapter 2

Cooling of Power Electronic Devices

2.1 Conventional Cooling Technologies

2.1.1 Air Cooling

Cooling all electronics is a critical step in any electro-mechanical design. The simplest way to cool electronic devices uses air as the convective heat transfer medium. First, it is essential to assess whether air cooling will suffice when beginning any thermal design. Air-cooled systems are cheap to manufacture, do not require complex designs, have few (if any) moving parts, and do not have liquid cooling loops (which often creates additional problems) [4]. The obvious downside to this cooling method is that the amount of heat dissipated is much lower than more advanced liquid cooling options. However, enhancements can still be made with fins of varying shapes and sizes to improve the heat transfer capabilities drastically. Two types of air cooling

methods exist, namely 1) natural convection and 2) forced convection. These will be discussed in detail in section 2.1.1.1 and section 2.1.1.2, respectively.

2.1.1.1 Natural Convection

Within air cooling, the first approach to explore is natural convection. Natural convection has many advantages, including low-cost, noise-free, and energy-free operation [5]. This type of convection is based on the fundamental thermal principles of heating and cooling air. When air is heated, it becomes less dense and rises. As the warm air rises, cool air replaces it, which creates something known as the 'natural convection current.' Since this is a naturally occurring process, the velocity associated with natural convection is low, which results in poor heat transfer. A way to capitalize on this natural convection current is to utilize a vertical heatsink. A vertical heatsink can better capture the airs' natural upward flow as it is heated. When designing such a heatsink, optimizing the fin spacing or pitch(S) is imperative, as shown in Fig. 2.1.

While adding fins increases the surface area, too many fins may result in worse thermal performance. A densely packed fin array will trap the heated air between the fins. This will have the opposite effect as desired and may cause the electronics to heat up. Therefore, the fins must be sparsely populated enough to allow the heated air to rise easily out the heatsink, thus extracting the heat from the system. Contrarily, having fins spaced too far apart will reduce the available heat transfer area and limit the cooling capabilities. Therefore, optimizing the spacing between fins for each particular application is critical. This spacing will vary depending on heatsink size, device power dissipation, and junction temperature constraints. In a study by

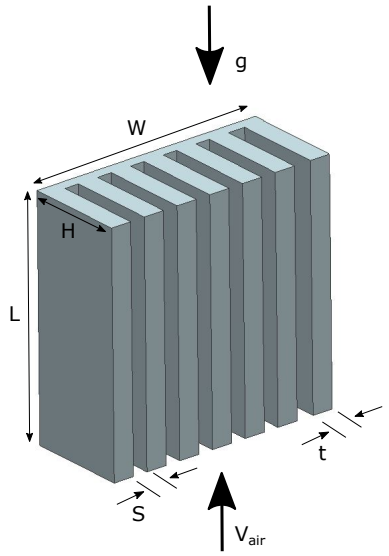

Figure 2.1: Vertical Heatsink

Ahmadi et al., a novel heatsink was tested, incorporating rectangular, interrupted fins instead of conventional straight, continuous fins. This design made it possible to postpone the thermal boundary layer formation, increasing the total heat transfer rate while simultaneously reducing the weight. Results showed that the new design could dissipate 5x more heat, with a 30% weight savings [6].

When using natural convection, treating the surface is often necessary. Surface treatments such as paints or anodizing increase the surface emissivity, allowing more heat transfer from the heat sink into the ambient air. This small radiation effect becomes negligible for heat sinks or cold plates using forced convection or liquid cooling.

2.1.1.2 Forced Convection

When natural convection cannot supply sufficient cooling, forced convection is the next viable option to explore. This method adds an external source such as a fan, pump, or jet of air to provide better cooling for the electronics. This induced

fluid velocity increases the heat transfer coefficient but is limited by the air's heat removal properties. Another way to increase the heat transfer coefficient is to increase/optimize the heat transfer area. When optimizing, there must be a balance between the thermal design, minimum material consumption, and minimum pumping power. A study by Bar-Cohen and Iyengar uses the least-energy and least-material optimization to categorize natural convection and forced convection heat sink designs [7]. Micro-channels are a promising study area since they can effectively increase the heat transfer surface area. Hilbert et al. investigated using laminar flow through micro-channels and achieved good heat transfer performance, and low thermal resistivity levels with a small internal pressure drop [8].

2.1.2 Indirect Liquid Cooling

2.1.2.1 Cold Plates

Since liquids have much higher heat transfer coefficients than gases (air), liquid cooling is more effective than either natural or forced convection. Liquid cooling is suitable for applications where the goal is to remove high heat fluxes from an electronics package. However, adding a liquid loop introduces risks such as leakage, corrosion, and additional weight.

Cold plates use various liquids with varying heat transfer capabilities. Common cooling mediums include water, ethylene glycol, gasoline, oils, propylene glycol, and distilled water; these liquids have unique viscosity, specific heat, and heat transfer characteristics. More information on some of these coolants can be found in section 3.1.3.2.

Cold plates directly couple the heat dissipating devices (power sources) with the

cold plate, which will pull the heat out of the system. Cold plate bodies are typically manufactured out of a highly conductive metal to transfer the heat from the device into the cooling channels. Many manufacturing methods exist when manufacturing these cooling channels; each will depend on the project design and constraints. Standard cold plate designs include formed tube, deep drilled, mini-channel, micro-channel, pocketed folded-fin, and pin fin. Each cold plate has various advantages and disadvantages and must be selected carefully based on the application.

A significant issue for all types of cold plates is a phenomenon referred to as 'thermal runaway.' Thermal runaway is a detrimental effect where further downstream devices experience higher temperatures because of heat picked up upstream. Since downstream devices usually have higher temperatures, they also have a much higher chance of failure, and a reduced operating efficiency [9]. This phenomenon is a critical issue to consider when designing any cold plate. The following sections discuss each type of cold plate and when to implement each.

2.1.2.2 Formed Tube Cold Plate

A formed tube cold plate (FTCP) is one of the most straightforward cold plate designs. It consists of a coolant tube attached to a machined base (Fig. 2.2). Copper tubing is often used because of its high thermal conductivity. This tubing can be bent to the appropriate shape to maximize the cooling and direct the flow under any hotspots/devices. Constructing the machined base(base plate) out of aluminum is recommended due to its light weight, cost-effectiveness, availability, and good thermal performance. However, copper can be implemented when a higher heat flux removal is needed. The copper tubing is often soldered, adhered to, or brazed onto the base

plate. The base plate, tubing, adhesive material, and solder material all have thermal resistance, increasing the system's total thermal resistance.

Since the FTCP design is straightforward, it is a very affordable option making it suitable for low-cost, low-power applications. However, with this simplicity comes relatively poor thermal performance. Compared to deep drilled cold plates, the FTCP had a significantly lower heat transfer coefficient, as shown in Song et al. [10].

If choosing an FTCP, the flow path is a critical consideration that will affect the cold plate's thermal performance. The copper tubing (flow path) must run directly below any heat source to maximize cooling. However, the pressure drop will be negatively affected for every added loop or turn.

Additionally, the total length of the coolant channel will determine the overall system pressure drop; therefore, it is critical to have a direct flow path without unnecessary looping. Rayt et al. investigated this flow path variability using CAD modeling to compare four various flow channel routes. The maximum temperature values for each design are used as the performance criteria within their work. Results show that flow routing has a significant effect on the device temperatures [11].

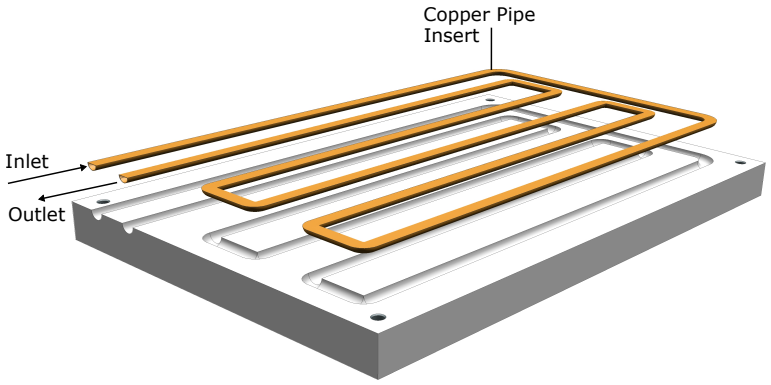

Figure 2.2: Formed Tube Cold Plate

2.1.2.3 Deep Drilled Cold Plates

A deep drilled cold plate (DDCP) is often superior if designed correctly when using higher power dissipating electronics. As previously mentioned, when comparing the FTCP to the DDCP design, DDCP had a significantly higher heat transfer coefficient [10]. Like the FTCP design, the baseplate is also generally aluminum or copper. However, instead of soldering a copper tube through which the coolant flows, coolant passages are drilled directly into the cold plate (Fig.2.3). The heat-dissipating locations/ hot spots determine where the passageways are drilled in the base plate. Often multiple parallel coolant passages are implemented to effectively remove the heat from the system while still maintaining acceptable pressure drop and device temperatures [12].

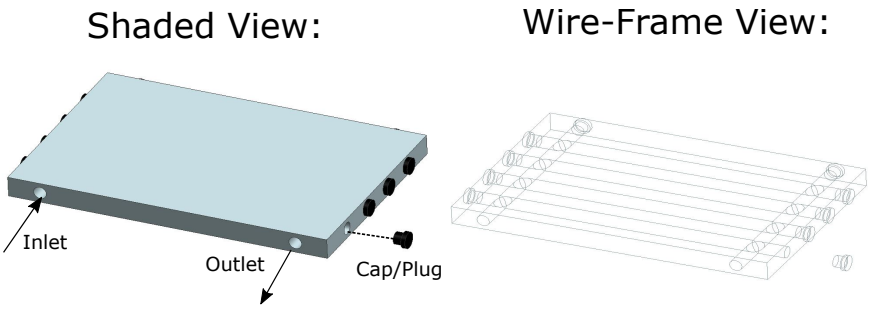

Figure 2.3: Deep Drilled Cold Plate

Like the FTCP, this cold plate design is relatively cheap and easy to manufcomplete,acture. It utilizes a process known as gun drilling to obtain long, straight holes. No internal burrs or defects can be left; otherwise, this can restrict the flow path and cause maldistribution or clogging. Careful planning goes into drilling the passages and how they overlap to form a coolant loop. Once the drilling is installing end caps

(or plugs) is done to direct the flow as desired. Finally, a brazing or electron beam welding process is used to install these caps securely, eliminating leakage.

2.1.2.4 Mini Channel Cold Plate

This type of cold plate uses small channels to achieve high cooling levels. It is essential to differentiate between rectangular fins (straight fins) and mini channel designs. The typical naming convention calls them fins when they consist of material extruded from a single surface (Fig. 2.4). However, these are typically classified as channels when the extruded material spans the gap between two fixed parallel plates. As heat flux removal requirements increase, optimizing the internal channel geometries for such designs is imperative. Channel geometry refers specifically to the channel width, height, length, thickness, spacing, and the number of channels. Depending on the thermal performance required, the channels can be anywhere from several millimeters to several micrometers (i.e., micro-channel cold plates). As the channel size decreases, the associated heat transfer coefficient increases. However, so do the manufacturing costs and design complexity; therefore, a design that maximizes heat transfer while minimizing costs is optimal. Fig. 2.4 shows an example of a mini channel cold plate.

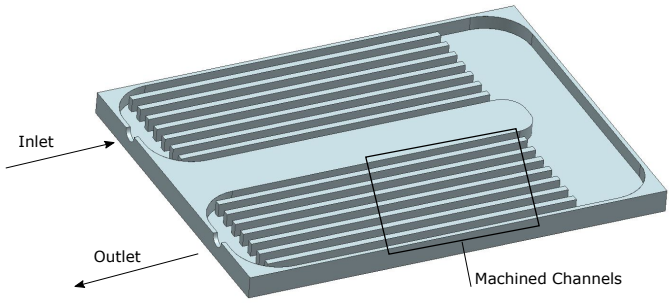

Figure 2.4: Mini Channel Cold Plate

In work by Nabeel et al., the performance of a mini channel heat sink(MCHS) was compared to a serpentine mini channel heat sink (SMCHS) design, using water as the coolant. They also added both ribs and grooves into the channel to investigate the effects of these enhancements. The study showed that adding ribs and grooves increased energy efficiency by 24% and 37% for the SMCHS and MCHS cases. However, the pressure drop of the SMCHS was approximately 39 times worse than the MCHS design [13]. Similar results are obtained by Zhu et al., who also looked at adding groove/ rib enhancements of various shapes and sizes to improve heat transfer [14].

Other design improvements for mini channel or straight fin designs can decrease overall weight and improve heat transfer. One such modification is introducing oblique slots into a traditional straight channel/fin. These oblique slots will have two benefits: 1) the total weight of the cold plate will be reduced due to less material being present, and 2) the heat transfer of the plate will be improved. This improvement in heat transfer results because of the unique oblique fin shape, which interrupts the flow path causing the re-initialization of the thermal boundary layer at the leading edge of each fin. This re-initialization will reduce the boundary layer thickness and cause the

flow to continually re-develop. Having the flow in an undeveloped state will induce higher turbulence resulting in better heat transfer performance [15]. Additionally, the secondary flow between channels can be beneficial for flow mixing, which will also help to improve heat transfer [16].

Besides adding oblique slots, additional work is underway studying inline oblique fin, incline fin, and louvered fin arrangements. After conducting testing, the louvered fin arrangement obtained the lowest surface temperature, followed by inline and incline [17]. Further enhancements are taking place in this field, but initial work shows promising potential for mini channel designs.

2.1.2.5 Microchannel Cold Plate

The sole difference between mini and microchannel cold plates is simply the size of the channels. Microchannels are defined as any channel with a hydraulic diameter of less than 1 mm; therefore, the geometry will fall on the micro-scale. While mini and microchannel designs share many similarities, the main advantage to using microchannel cold plates is higher heat flux removal ($> 100\ \frac{W}{cm^2}$).

To investigate differences between liquid cold plate designs, Lee and Vafai compared two common approaches to cold plate cooling; microchannel and jet impingement cooling. They found that microchannel cooling was preferable for small target dimensions of less than 0.07 by 0.07m, while jet impingement is comparable or optimal for a larger target cold plate [18]. Harris et al. took a different approach to conventional methods by combining micro-channel liquid cooling with crossflow via air within the same design [19]. They discovered that the cross-flow micro heat exchanger could improve heat transfer compared to conventional heat exchangers.

Combining liquid cooling with air cooling is practically implemented in the automotive industry with technologies such as the commonly used radiator.

Using customizable inserts instead of machining the tiny channels is also an option when incorporating micro-scale geometry. This design includes a higher complexity design for the inserts, while the baseplate remains relatively simple. Examples of these inserts are micro straight fin or micro pin fin designs created using micro deformation technology (MDT). MDT is a process that uses a fixed tool to mechanically and plastically deform a workpiece. This patented MDT process is unlike typical manufacturing since it does not use a subtractive process, reducing material waste [20]. The result is a consistent, repeatable fin pattern suitable for mass production. This process is becoming more mainstream since it can create optimal fin and pin geometries with limited waste.

In another study by Reeves et al., a test is conducted to investigate the effect of fin geometry on heat transfer. Testing includes three fin geometries: straight fin, round staggered pin fin, and MDT in-line pin fin design. When compared, the MDT pin fins performed the best, followed by round fins and then straight fins, given a 1mm flow gap constraint [21].

There are still several roadblocks in implementing microchannel cold plates on a commercial scale. The most significant roadblock is the high manufacturing cost because of the specialized equipment needed to manufacture these plates on such a micro-scale. Another major issue is the increased risk of internal fouling and clogging of the system due to the tiny cross-section of the channels.

2.1.2.6 Pocketed Folded-Fin Cold Plate

Pocketed folded-fin cold plates (PFCP) use a fin array insert within the cooling channel to enhance the heat transfer capabilities. These fin arrays come as pre-made inserts and install into a recessed pocket within the cold plate. These fin arrays are then typically soldered or brazed to the cold plate. Many insert types are available, including straight fins (square edges), straight fins (round edges), ruffled, herringbone, lazy ruffled, lanced, offset, perforated, and triangular [12]. These have different thermal resistance and surface area specs making them suitable for various applications depending on the project constraints. Fig. 2.5 shows an example of a square edge straight fin PFCP design. Many vendors across the country offer either pre-made or custom options for relatively low prices, making this type of cold plate a viable option in many situations.

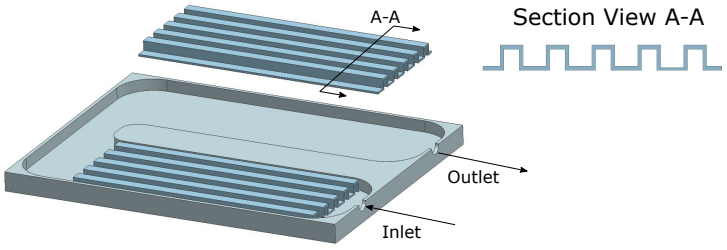

Figure 2.5: Pocketed Folded-Fin Cold Plate

This type of cold plate experiences issues when securing the fin array to the base plate. This solder or brazing material has a thermal resistance that will reduce overall thermal performance. Additionally, the solder or brazing process can be complicated,

time-consuming, and require special tooling (oven). Careful planning and design are needed to direct the brazing material into the required areas. Improper material flow will result in a weak bond or lessoned thermal performance (due to air gaps).

2.1.2.7 Pin Fin Cold Plate

Pin fin cold plates are a commonly implemented cooling solution due to their simplicity and relatively good thermal performance. These cold plates can come in various shapes and sizes, each with unique benefits and drawbacks. Some of the most common pin fin shapes include circular, square, or rectangular fins. It is essential to understand how pin fins designs compare in terms of performance. One paper by Kim et al. compares straight plate-fins and pin-fins. In the paper, they compare the performance of these two configurations under a fixed pumping power constraint. They developed a contour map demonstrating that the straight plate-fin design has a lower thermal resistance at low pumping power and large heat sink length. Contrarily, when the pumping power is significant and the length of the heat sink is small, the pin-fin design results in a smaller thermal resistance [22]. This work coincides with Chapman et al., who compared rectangular cross-cut pin fins, straight fins, and elliptical pin fins (Fig. 2.6). After comparing the rectangular cross-cut pin fins and elliptical pin fins, the elliptical pins had improved heat transfer. This increase is because the elliptical geometry reduces vortex flow and eliminates boundary layer effects, resulting in better heat transfer. The paper shows that even though roughly 40% more air was flowing through the rectangular cross-cut pin fins, it had virtually the same thermal resistance as the elliptical design [23]. Therefore the rectangular

cross-cut pin fin design requires more pumping power without significant thermal resistance reduction. Additionally, they found that the straight fin design performed significantly better than the other two configurations over the flow range tested.

In a further extension by Jihed Boulares, he looked at the comparison between circular pin fins and "tear" drop-shaped pin fins. His results conclude that the drop-shaped pin fin significantly improved heat transfer over the same pressure drop characteristics. This improvement is due primarily to the delay in flow separation of the drop-shaped design and the increased surface area for heat transfer [24].

Besides adjusting the geometry of these pin fin designs, it is also essential to optimize their orientations'. Two main configurations/orientations exist; 1) aligned configuration and 2) staggered configuration. It is crucial to realize the differences between the two. The staggered orientation will typically have a higher heat transfer because the flow path will be interrupted at each subsequent row, inducing turbulence and reducing channel clogging. However, with this increase in turbulence comes an increase in pressure drop, negatively impacting the design.

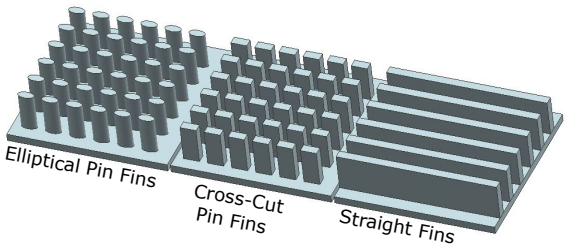

Figure 2.6: Pin Fin Configurations (Adapted From [23])

The pin fin locations and the configuration are two things that must be optimized

when designing a pin fin cold plate. This optimization concept is what Tien-Yu Lee uses to create a liquid-cooled cold plate for an IGBT power module. This paper goes through the complete design process, beginning with a single flow channel with no pin fins. Using CFD to analyze different configurations, he tests a variety of designs. After several iterations, a 3-2-3 pin array upstream and a 4-3-4 pin array in the downstream locations are chosen. This fin configuration keeps the IGBT module peak junction temperature of 100.1°C, with a difference of only 1°C between the upstream and downstream dies [25]. These results significantly improved the initial design, with a maximum (peak) junction temperature of 109°C, with 11°C variations between the upstream and downstream dies. This non-uniform temperature is disastrous from an electrical standpoint since this would result in unequal current sharing for the DC-DC converter.

Additional heat transfer benefits are possible by introducing advanced features such as perforated fins. A study by Amer et al. investigated using perforations within the pin fin to enhance heat transfer. They concluded that a pin with five perforations had an 11% higher Nusselt number than its solid counterpart. They noted that pressure drop is also significantly reduced. However, this exact pressure drop improvement was hard to pinpoint accurately. This difficulty is because pressure drop is highly dependent on having the perforations line up perfectly with the flow. However, the author still reduced the pressure drop by 7% for the fin with three perforations, slightly less than the predicted 9% reduction [26].

2.1.3 Direct Liquid Cooling

A conventional power electronic package consists of several interface layers. The electronic device(s) (e.g., MOSFET, IGBT, and Diode) is soldered onto a ceramic-based substrate, conventionally a direct bond copper (DBC) substrate. This substrate is then typically soldered onto a copper or aluminum base plate. Lastly, this base plate is attached to an extruded heatsink or cold plate, usually manufactured out of aluminum or copper. This heatsink or cold plate is usually air-cooled or liquid-cooled, depending on the cooling requirements. A thermal pad or grease is required between the baseplate and the heat sink. This layer assists in transporting the heat from the base plate into the cold plate while maintaining electrical insulation. Fig. 2.7 shows a standard power module package commonly found in the aerospace industry.

The majority of the system thermal resistance comes from the heatsink and

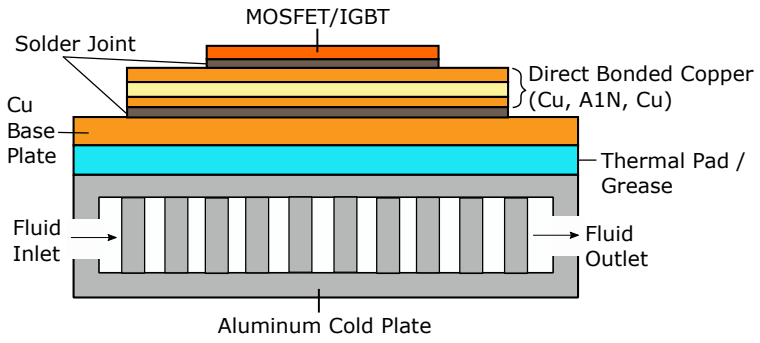

Figure 2.7: Standard Power Module (Adapted From [27])

the thermal interface material (TIM). To decrease overall thermal resistance, reduce either the thermal resistance of the heatsink or the pad/grease. One method is to optimize the heatsink or cold plate design to create less resistance to heat flow. Integration of the baseplate and heatsink into a single part can also help to eliminate

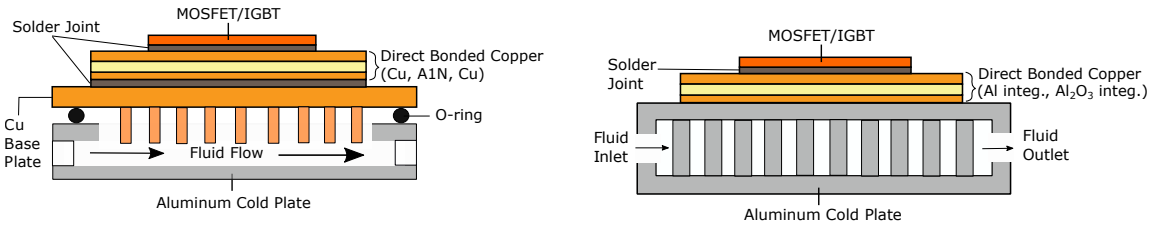

(a) Direct Base Plate Cooling (b) Directly Integrated Substrate Cooling

Figure 2.8: Comparison of Direct Cooling Methods (a) With Direct Substrate Cooling (b) With Directly Integrated Substrate Cooling (Adapted From [27])

system thermal resistance. Then coolant can be applied directly to the baseplate to provide direct cooling and remove an interface layer (Fig. 2.8a).

Further enhancements can be made by directly integrating the substrate and the cold plate. This integration removes an additional solder joint, decreasing the packages' overall thermal resistance (Fig. 2.8b). Schulz-Harder et al. studied the feasibility of this integration, concluding that the integrated solution reduced the thermal resistance for all observed flow rates. However, they noted that integrated solutions are much more costly to manufacture, while the reduction in thermal resistance is relatively insignificant [27].

2.1.3.1 Direct Liquid Immersion

Direct liquid immersion is another type of electronics cooling. Cooling occurs by submerging components directly into a dielectric liquid. A dielectric liquid does not conduct electricity; in other words, it is a good insulator. This property gives these liquids the ability to quench electric discharges rapidly; an excellent example of this is distilled water. An ideal dielectric liquid must have high dielectric strength,

high thermal stability, be non-flammable, have good heat transfer, and be reasonably priced. There are two basic categories of immersion cooling; single-phase and two-phase cooling. In single-phase cooling, the dielectric fluid travels over the hot electronics, pulling the heat out. The system transports the heat to a heat exchange device where the fluid is cooled and then re-inputted into the system. At no point in this cooling process does the coolant change phase (i.e., from liquid to gas); for this reason, it is referred to as single-phase cooling.

The main difference in two-phase cooling is the change of phases from liquid to gas. In two-phase immersion cooling, a low-temperature evaporation process removes heat from the electronics. This process is only possible when using an engineered fluorocarbon-based liquid with a low boiling point (often below 50°C). This low boiling point causes the liquid to evaporate with less heat added to the system. This vapor gets condensed back into liquid form through a condenser. Lastly, this liquid goes back into the system to be used again for cooling.

As might be expected, two-phase cooling can be much more effective at removing high heat fluxes from electronics due to the changing states of the coolant. However, both single-phase and two-phase cooling can be highly effective heat dissipation methods. One significant downside of this type of cooling is the high cost and complexity of the design. The two-phase coolant is very expensive since it utilizes a fluorocarbon-based fluid, whereas the single-phase system uses a much cheaper hydrocarbon-based fluid. In addition, the added water boiling may introduce mechanical stresses, contamination, and mechanical design issues [28]. Therefore, all these considerations must be considered if the engineer decides to incorporate either a single-phase or two-phase cooling design.

2.1.3.2 Jet Impingement

Jet impingement allows the designer to direct the fluid precisely onto the surface to be cooled. The coolant is highly turbulent upon impact by utilizing jets, thus increasing the heat transfer coefficient. Many studies look at the heat transfer and fluid flow characteristics over several different heat sink geometries. These studies have focused on the heat spreading and thermal resistance of the heat sink. Wiriyasart and Naphon test three design geometries in this paper: conical, rectangular, and circular fins where the jet impinges on the heated surface to cool it. Experimental results show that the circular fin resulted in a thermal resistance reduction of 12% and 25%, compared to the conical fin and rectangular fin designs, respectively [29]. In a further extension by Wiriyasart and Naphon, they conclude that power input, coolant mass flow rate, heat source area, pin fin geometries, and coolant types all play a significant role in the heat sink performance [30].

There are many configurations to investigate for impingement jets, including free, plunging, submerged, confined, and wall-type jet configurations. The three most commonly used are free, submerged, and confined-type jets [31]. The free surface jets are standard in industry; these shoot a pressurized gas or liquid at a hot surface to be cooled. A submerged type of jet has a nozzle wholly submerged within a liquid. Again pressurized air or liquid is expelled from the nozzle directed at the surface to be cooled. Lastly, the confined jet configuration is similar to the free surface jet, except the liquid gets entrapped within the nozzle. Before finalizing any design, it is crucial to look at all configurations and the benefits and drawbacks of each. The study by Gould et al. investigates how the number of jets, jet pattern, and impingement distance factor into the amount of cooling achieved. The results from the study show

that by switching to the proposed jet impingement design, the junction-to-coolant thermal resistance reduces from $1.25\frac{^\circ C}{W}$ and $0.76\frac{^\circ C}{W}$ for the cold plate and micro-channel cooler, respectively, to $0.45\frac{^\circ C}{W}$ [32]. This resistance reduction significantly decreases junction temperature, which is critical to ensure component longevity.

Overall, jet impingement can be a good option when high heat flux removal is required. However, jet impingement designs are often complex, and manufacturing multiple small jets can significantly drive production costs.

2.2 State-of-the-Art Cold Plate Cooling Technologies for Aerospace Applications

2.2.1 Direct Integrated Cooling

This concept of directly integrated cooling has already been touched on briefly in section 2.1.3; however, it would be beneficial to dive into it a little deeper here. The main goal is to directly integrate the heat sink and the DBC structure within a power module. This integration can effectively eliminate the need for solder, TIMs, or heat sink layers, reducing the overall thermal resistance.

In theory, this concept is obvious, but it can be quite complex to implement.Careful material selection and a calculated assembly process are critical to implementing this concept successfully. A microchannel design formed by integrated silicon fins was created and tested by Colgan et al. This paper achieves cooling levels of $300\frac{W}{cm^2}$ and higher, with a final thermal resistance of $10.5\frac{^\circ C-mm^2}{W}$ [33]. These results were obtained using a flow rate of 1.25 liters/minute with a pressure drop of <35kPa.

Part of the work in this field has been looking at different hybrid materials. The

paper by Tang et al. introduces a hybrid material, which combines the copper and ceramic of the substrate to the aluminum of the heat sink. This bonding process uses a carbon nanofibre adhesive, a novel concept in the power electronics field [34]. The motivation of this hybrid material was to have the aluminum heat sink be in direct contact with the liquid because of its corrosion resistance while utilizing the copper side for superior electrical and thermal capabilities. The manufacturing and assembly of this hybrid material were successful; however, performance and reliability tests still need to be conducted.

In 2019, Jung et al. investigated the performance of an embedded silicon microchannel cold-plate with 3-D liquid distribution manifolds. This cold plate can remove $250\frac{W}{cm^2}$ at a max temperature of $90°C$ with a pressure drop of less than 3kPa and a flow rate of 0.1 liters/minute [35]. It is important to note that this test experienced micro-fabrication defects, which can be common when dealing with such intricate manufacturing. These defects made it hard to predict the pressure drop accurately, thus increasing the uncertainty of the surface temperature calculations.

Chen et al. applied this integration technique to the thermal management of lithium-ion batteries. They hoped to avoid critical issues such as overheating and thermal runaway of the batteries. A design was optimized and verified by Chen et al., and results showed that temperature reductions of 1.87°C and temperature deviations of 0.35°C were recorded [36].

More recently, Erp et al. developed a new multi-layer manifold micro-channel (MMC) heatsink capable of cooling 20 devices simultaneously. The design consists of three layers of Polymethyl methacrylate (PMMA): a transparent, rigid thermoplastic,

and a single silicone layer. The bottom-most silicone layer utilizes deep-reactive-ion-etched (DRIE) microchannels, which helps increase the cooling surface area. During testing at 1kW of output power, the average temperature rise was $10.37°C$, a 76% and 60% reduction compared to a conventional heat sink with natural convection and forced air cooling, respectively [37]. Although this design is relatively complex, it is suitable for applications that require very high heat flux dissipation.

2.2.2 Double Sided MOSFET Cooling

Another intuitive way to enhance cooling ability would be to implement double-sided cooling. If cooling occurs on both sides of a device, it stands to reason that the cooling effect could be up to twice as effective. Another area of research for state-of-the-art converters is modularizing the cooling systems (i.e., making them as compact as possible). These two focus areas are not mutually exclusive, and both should be considered simultaneously during the design process. In the paper by Marz et al., they outline an overview of power electronics integration within the automotive industry. This paper focuses on system-level and component-level integration, which makes designs more modular, saving considerable space. However, many challenges arise when integrating, including limited space, complex structures, contaminants, thermal and mechanical stresses [38].

Since the extra surface area for double-sided cooling is much larger, the double-sided cooling method will have superior thermal performance. This performance improvement is illustrated by Schneider-Ramelow et al. after their experimental results show a 40% improvement between single and double-sided cooling [39]. A similar

study by Wang et al. verifies this concept, with a 47.5% improvement when comparing single and double-sided packages [40]. Double-sided cooling is being researched heavily in the automotive industry since cooling is often the limiting factor for power electronics packages [41].

Toyota has implemented this concept into a double-sided power module assembly design. This design connects the silicone chip via solder to copper heat spreaders on both sides. Next, each heat spreader connects to a ceramic insulating layer. This ceramic is the final layer before reaching the aluminum liquid cold plates, which are directly cooled [42]. The design incorporates the entire power stack with all individual modules stacked together, thus reducing space requirements. This design uses a compression force to keep the modules together, eliminating the risk of leakage [43]. Consistent with other results in this field, the double-sided cooling had almost half the resistance as a conventional single-sided system.

2.2.3 Heat Transfer Enhancement Techniques

A wide range of enhancement techniques can drastically improve cold plate performance. Using these techniques only occurs after an initial analysis and design phase. Two main categories of enhancements exist; passive and active enhancements. Passive methods require no external power. Examples include treated surfaces, roughened surfaces, and extended surfaces [44]. These methods involve modifying the shape, surface area, or roughness of the heat transfer surface area. The rougher the surface is, the more turbulence is induced in the flow, increasing the heat transfer. However, increased turbulence and roughness will inevitably cause higher pressure drop, so an acceptable trade-off is required.

Other passive enhancements include displaced enhancement devices, swirl-flow devices, coiled tubes, and surface tension devices. Typically, these devices are inserted into the flow channel to indirectly improve energy transport at the heated surface.

Additionally, active techniques are often used to increase heat transfer. Some examples of such enhancements include mechanical aids or surface/fluid vibrations. Mechanical aids assist in stirring or mixing the fluid using a rotational force. Next, electrostatic fields may increase the fluids' bulk mixing in dielectric fluids. Lastly, injection and suction are the last two active heat transfer enhancement techniques. Injection involves adding gas to the liquid, whereas suction consists of the vapor removal from the fluid [44].

2.3 Weight Reduction Methods

Weight reduction is a vital aspect of cold plate design, especially when using these plates in the automotive or aerospace industries. In either of these industries, extra weight means less range for the vehicle and reduced payload. These reductions will limit the implementation of these vehicles since range anxiety is a significant problem for electric vehicle adoption. The paper by Noel et al. identifies "range anxiety" as one of the most significant barriers to the mainstream adoption of electric vehicles. In this paper, they define range anxiety as the psychological anxiety of the consumer concerning the limited range of electric vehicles [45]. This fear is not grounded in reality since this technology has been drastically improved over the last several years to improve performance and range. Additionally, the infrastructure to support electric vehicles has been steadily increasing to meet the growing number of electric vehicles in circulation.

When it comes to a cooling system, this weight reduction concept must be applied to maximize the power density. Using traditional mechanical systems to solve design problems that engineers faced was very common in the past. Today, electrical systems replace many of these mechanical systems to reduce weight, decrease fuel consumption, and improve the overall design. This switch to electrical systems requires better thermal cooling systems to remove higher heat fluxes from these electronics. The paper by Sharar et al. investigates moving from a single-phase cooling system to a two-phase cooling system to reduce the overall flow rate required. This reduced flow rate will require smaller fluid reservoirs, less onboard fluid volume, reduced pumping power, and smaller pumps [46]. These all will help reduce the system weight and volume, which will increase the overall power density.

A paper by Uhlemann et al. studied the effects of joining aluminum and copper together. The copper would be situated on the top mainly for soldering and electrical capabilities. Meanwhile, the bottom would be constructed from aluminum for weight reduction and would be responsible for most of the cooling. This connection underwent rigorous thermal cycling tests, resulting in an excellent, durable bond. Results from testing show that the new design by Uhlemann et al. improves the thermal resistance by 10%, with a weight reduction of about 30%.

2.3.1 Design Optimization

Design optimization is a critical concept to incorporate into any cold plate design. There is a wide range of techniques for optimization, each with its own unique optimization goal. These goals can include variables such as channel geometry optimization, pumping power reduction, cold plate weight reduction, junction temperature reduction, and thermal resistance reduction, to name just a few [47].

When it first came out, optimization relied heavily on the governing equations of fluid dynamics. These equations combined with conductive and convective heat flow were the basis for all early optimization techniques. Knight et al.'s work combines these dimensionless equations for both turbulent and laminar flow. The paper then outlines a method to solve the equations that determine the optimized heat sink dimensions, which result in the lowest thermal resistance between the heatsink and coolant [48]. While this paper focuses on heatsinks, the same principles can also be applied to cold plates. Ritzer and Lau use a completely different form of optimization by analyzing a series of heat sinks with price as the optimization variable. Their analysis included the price of the original part (machining plus fan mounting), plus all other associated costs such as packaging and shipping. This analysis led them to conclude that passive air-cooled systems were unsuitable for their large, bulky design. Additionally, they discovered that high-density heat sinks were comparable in price to low-density models, even though they had superior thermal performance [49].

The introduction of computational fluid dynamics (CFD) opened many new optimization possibilities. CFD uses numerical structures coupled with numerical analysis to analyze fluid flow problems. Li and Peterson used this concept to create a three-dimensional (3-D) conjugate heat transfer model consisting of a 2D fluid flow and a

3D heat transfer model. Using this model, they optimized the geometric structure of a heat sink [50]. Additional heat transfer analysis by Husain and Kim uses 3-D Navier-Stokes and conduction equations to optimize for minimal thermal resistance geometrically [51].

2.3.2 Topology Optimization

Topology optimization (TO) is an integral part of cold plate design which uses a mathematical approach to optimize material layout within a given design area for a specific set of constraints. Complex designs that were not possible several years ago are now becoming commonplace due to increases in manufacturability due to 3D printing and precision machining technologies.

Generally speaking, topology optimization is required to achieve a design with optimal parameter reduction. By optimizing the geometric parameters of the cold plate, weight and volume improvements can often result. This optimization usually entails modifying the internal fin structures of the cold plate. The paper by Qian et al. uses topology optimization to create a three-dimensional flow channel for an active phased array antenna. After comparing results to a traditional S-type flow channel, they found that the optimized design performed better in most characteristics except the RMS_{delta}, with reasons explained in the paper [52].

Another similar paper by Yu et al. used moving morphable components (MMC)-based approach to optimize a design topology. The paper details the design progression at each iteration and how it changes over time. The optimized design is verified using a density-based approach, with similar (but slightly worse) results. Overall, the MMC approach can achieve the lowest value of the objective function, meaning that

it has reached the optimal solution [53].

One common application of topology optimization is volume or mass minimization for cold plates or heat sinks. This minimization is essential for aerospace applications since weight and volume are often the two most critical parameters. The paper by Dede et al. uses topology optimization to create a unique heat sink design using additive layer manufacturing (ALM) techniques. When comparing this heat sink to traditional designs using conventional manufacturing processes, it outperforms the competition [54].

Further advancements by Alexandersen et al. used topology optimation of three-dimensional heat sinks cooled by natural convection. Results show the creation of complex geometrical designs capable of excellent heat transfer. The optimized results are verified using COMSOL and agree with the literature [55].

Overall, a considerable variety of optimization algorithms can be employed to optimize the cold plate's geometric parameters to minimize weight, pressure drop, and temperature simultaneously. The focus will be on the genetic algorithm's potential in the cold plate design process.

2.3.3 Genetic Algorithm Optimization

A genetic algorithm (GA) works on the "survival of the fittest" premise. This concept is taken directly from nature and mimics the natural evolution of species. Each potential solution vector is an 'individual' or 'chromosome' and has a unique set of genes. The GA algorithm starts by initializing a set of population points or chromosomes by random generation. Each chromosome gets ranked on its respective fitness or how well it minimizes the objective function. For the GA algorithm, fitness

is defined as the negative of the objective function. Chromosomes with higher fitness values are better able to minimize the objective function. There are two main methods to achieve better (higher) fitness values in successive generations: crossover and mutation.

Firstly, crossover is employed, which takes two "parents" from the initial population and combines them to form an "offspring." Mating priority gets given to parents with higher fitness, and they will have a higher likelihood of reproducing. Hopefully, the offspring inherits the good genes of its parents and will have a higher fitness value as a result. As generations pass, the fitness of the chromosomes should increase until they eventually converge to an optimal solution.

The second method to improve the fitness of the chromosomes is through mutation. Mutation helps with exploring new points and areas in the parameter space. While crossover leads to convergence, mutation will cause genetic diversity within the population, hopefully avoiding local minima. This mutation will occur at a set probability dictated by the user. Usually, the likelihood of such an occurrence is relatively low.

Cold plate design optimization often uses a multi-objective genetic algorithm (MOGA). This MOGA is required since there are typically several conflicting objective functions which must be optimized simultaneously. Since weight is a critical design parameter for aerospace applications, this is a crucial parameter within most algorithms. Other objective functions to minimize include device junction temperature, pumping power, pressure drop, operating costs, and thermal resistance. Certain objective functions can be maximized instead, including heat transfer coefficient, heat transfer surface area, reliability, and entropy generation. A combination of these

aforementioned objective functions is often used in a single optimization algorithm. Lv et al. use multi-objective optimization (MOO) to solve for optimum system reliability while minimizing the annual cost of a heat exchanger [56].

In work by Khan et al., they implement a GA to minimize investment, operating, and total annual costs while simultaneously maximizing the heat transfer rate. They used three different algorithms, Genetic Algorithms, Differential Evolution, and Adaptive Simulated Annealing, to help generalize and improve the robustness of these algorithms [57]. Wu et al. uses a GA to create a complex heat sink design. This work relies on the fact that 3D printers can print complex shapes, which opens many possibilities for different heat sink/cold plate designs. The paper showed a 15% improvement in thermal performance using a GA optimization technique [58].

In the thesis by Andrew Michalak, he goes through an extensive explanation of the methodology and construction of the GA optimization, which he utilizes in his work. He creates a unique 3D structure with superior cooling capabilities than the conventional or "off the shelf" heat sinks [59].

Chapter 3

Cold Plate Design and Manufacturing

3.1 Design Considerations for Cold Plate Design

3.1.1 Material Selection

3.1.1.1 Power Electronic Devices

Most cooling systems have a series of power electronic devices which need to be cooled. These devices are fabricated from silicon (Si) or a wide band gap (WBG) material such as silicon carbide (SiC), gallium nitride (GaN), or diamond. Research over the last several years has shown that silicon semiconductors have reached (or are very close to) their theoretical limits; therefore, other alternatives are necessary. Research is going into wide band gap semiconductors such as SiC and GaN to replace silicon. These devices can obtain higher blocking voltages, switching frequencies, efficiency, and reliability, all of which are critical for increasing the power density of a DC-DC

converter package [60]. WBGs have a much higher thermal conductivity (except for GaN) and, therefore, smaller junction-to-case thermal resistance [61]. This reduced resistance implies that heat can easily be extracted from the device and dissipated by the cooling system. Of these devices, diamond has the best electrical and thermal properties. However, its hard material properties, combined with difficulty processing and manufacturing, limit this material's implementation [62].

The use of WBGs in aerospace applications is critical since they can operate efficiently at higher temperatures and produce lower losses when compared with conventional silicon devices. When implemented within the DC-DC converter, these devices will create mass and volume improvements since fewer devices would achieve similar or better performance.

3.1.1.2 Substrate Material

The power dissipating devices are then typically soldered onto a dielectric substrate with several unique functions. The substrate provides interconnections between the various electrical devices similar to a PCB. Secondly, these substrates are instrumental in the heat spreading and, therefore, thermal performance of the system. Lastly, the substrate assists in electrical insulation between devices. Ceramic and direct bonded copper (DBC) are two commonly used substrates found within most power modules. Typical DBC substrates include two layers of copper bonded onto either side of an aluminum-oxide (Al_2O_3) or aluminum-nitride (AlN) ceramic base using a high-temperature oxidation process. Other potential ceramic material candidates include boron nitride and silicon nitride (SN_3N_4). In a paper by Chasserio and al., the authors investigate the electrical, mechanical, and structural properties of four

common materials; alumina, aluminum-nitride, boron-nitride, and silicon-nitride.

One thing the literature is consistent on is that DBC substrates exhibit good mechanical strength and corrosion resistance, excellent thermal insulation, thermal conductivity, and thermal cycling stability [63] [64]. One of the essential DBC substrate advantages is its low coefficient of thermal expansion (CTE). Fig. 3.1 shows the thermal expansion rates of some materials commonly used in power modules.

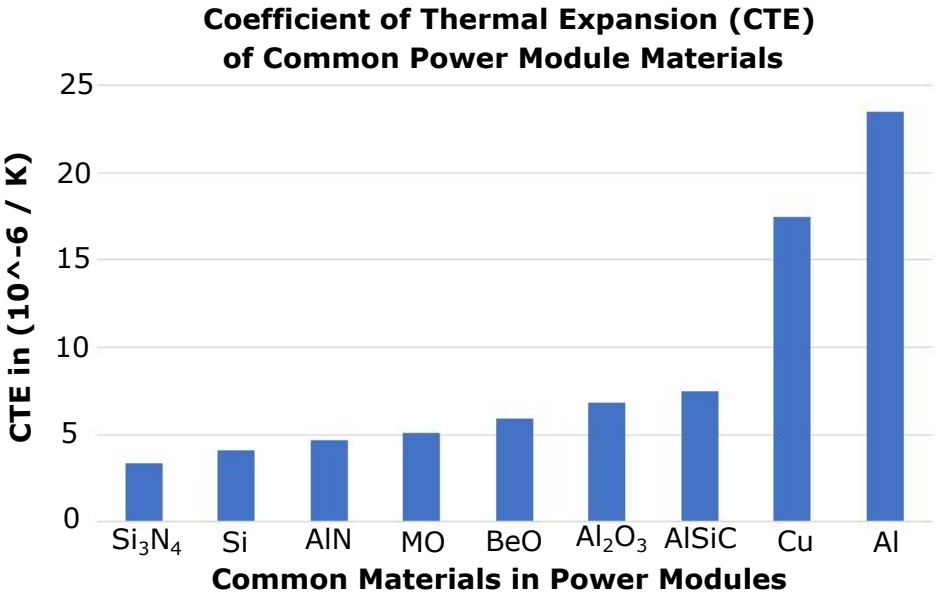

Figure 3.1: Coefficient of Thermal Expansion for Common Material Found in Power Modules (Adapted From [39])

As its name suggests, this coefficient of thermal expansion (CTE) characterizes how a material will expand and contract under thermal cycling (i.e., heating and cooling). Materials with similar CTE values should be placed next to each other. Failure to do so may result in fatigue, internal cracking, and overall system degradation since these materials will expand at different rates during thermal cycling. Fig. 3.2 depicts this thermal expansion process, which shows a power electronics package

experiencing cooling and heating scenarios. For this reason, Schneider-Ramelow et al. proposed a new package design that bonded the top side contacts to a DCB with matching CTE, thus increasing the lifetime reliability [65].

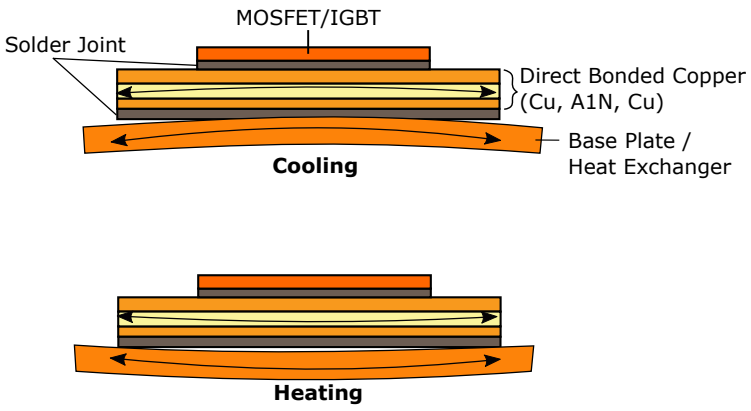

Figure 3.2: Power Electronics Package Deformation Due to CTE Mismatch Under Cooling and Heating Conditions (Adapted From [66])

The paper by Devoto et al. outlines just how common issues with CTE mismatches are and some of the associated reliability concerns [66]. Mitic et al. conducted a similar study examining AlN substrates' delamination and crack propagation under thermal cycling. To mitigate these issues, Pahinkar et al. propose a new packaging design that uses an AlN dielectric substrate directly bonded to the AlSiC baseplate/heat sink using a transient liquid phase (TLP) bonding approach [67]. As shown in Fig. 3.1, these two materials have very similar CTE values, thus minimizing the CTE mismatch and hopefully avoiding all the potential issues mentioned previously. The design and test of this proposed power electronics package reduced the CTE mismatch by 84%, improved the theoretical lifetime by 18 times under test conditions,

and made the package lighter and more compact. However, the heat spreading of this design would not be as efficient because it does not have the copper found in typical DBC substrates.

3.1.1.3 Cold Plate Material

When choosing a cold plate material, there are two critical deciding factors; thermal conductivity and weight. The higher the thermal conductivity, the more heat it will pull from the electronic components and dissipate into the coolant. Aluminum is one of the most commonly used cold plate materials, even though its thermal conductivity is relatively low (in the range of 167-247$\frac{W}{mk}$). Aluminums' wide availability, low cost, and ease of fabrication make it a great alternative to better heat-conducting materials. One such alternative to aluminum is copper, which has a much higher thermal conductivity (in the range of 371-398$\frac{W}{mk}$). However, since copper is much more expensive to purchase, it is usually reserved for high heat flux removal applications. Silver and diamond alternatives can be used for high heat flux removals since they exhibit very high thermal conductivity values of 406-429$\frac{W}{mk}$ and 2000-2200$\frac{W}{mk}$, respectively. However, since these materials are expensive to purchase and challenging to manufacture, this section will deal primarily with aluminum and copper cold plates since they are most commonly used in aerospace.

The second critical aspect of cold plate material selection is weight. The density of the material used dictates the resultant weight of the cold plate. Standard material densities are 2640-2810$\frac{kg}{m^3}$, and ≈8940$\frac{kg}{m^3}$ for aluminum and copper. Clearly, aluminum will be lighter since its density is less than $\frac{1}{3}$ the density of copper, making it a desirable candidate for aerospace applications. Often metals and plastics are

combined to make a single, lightweight cold plate design. The body of the cold plate is made from plastic to reduce weight. Then parts in direct contact with the fluid are made out of copper or aluminum due to the more favorable thermal characteristics.

In the paper by Wang et al., carbonaceous materials and carbon matrix composites (CAMCs) are explored as possible alternatives when designing heat exchangers and heat sinks. These materials can create advanced thermal management alternatives due to their exceptional thermal conductivities, low density, low coefficient of thermal expansion, and chemical stability. In the same paper, both carbonaceous materials (including carbon, graphite, diamond, HOPG, ThermalGraph, carbon foam, and CNTs) and CAMCs are reviewed in detail. This study outlines the potential of these advanced materials as replacements for standard materials such as copper or aluminum. However, there are still low compressive strength and friability issues, making processing and shaping these materials difficult [68].

In another paper by Smalc et al., a natural graphite spreader was designed for a laptop to reduce the amount of temperature experienced by the user. Test results achieved a thermal conductivity of $369\frac{W}{mk}$, comparable to copper, but at a heavily reduced weight [69].

3.1.1.4 Joining Material

Several methods exist to join the semiconductor die-substrate and substrate-heatsink interfaces. Soldering, brazing, or low-temperature sintering are most commonly used [70]. Low-temperature sinter technology is an exciting new technology, with results from Gobl and Faltenbacher showing that the reliability of a module could be increased by a factor of three compared to a standard soldered module [71].

This study looked at silver as a soldering alternative due to its impressive electrical and thermal conductivity. Additionally, silver is not susceptible to oxidation and performs well under thermal fluctuations. The only downside to this material is the high temperature with which it must be processed, but it still can be an attractive alternative.

3.1.1.5 Thermal Interface Material

Thermal interface materials (TIM) are critical within electronics packages since they improve the contact resistance between mating surfaces. This TIM usually consists of thermally conductive gels, thermal pads, greases, or phase change materials (PCMs), which assist in filling surface irregularities (or voids) at a micro-level between mating materials [72]. This improved contact results in better heat transfer from the heat source to the heat sink. Unfortunately, this TIM layer can account for approximately 40-50% of the total thermal resistance of the package, so this can significantly reduce the effectiveness of the cooling system. Other possible TIMs are solder and carbon nanotubes (CNTs), but these are less common and more expensive solutions. Choosing a thermal interface material is critical since it can minimize thermal resistance and improve system reliability. Some TIMs (gels, greases) may experience pump-out after repeated thermal cycling and dry-out over a product's life cycle. Either pump-out or dry-out may eventually lead to voids in the interface material, which will increase resistance and, therefore, decrease the material's thermal conductivity. Therefore, choosing the correct TIM is critical to any thermal design of an electronics package.

3.1.2 Manufacturing Methods

Plenty of manufacturing methods exist, each with its unique benefits and challenges. Some common types of manufacturing are outlined in this section so that the designer can choose one which meets their specific project constraints. Typical manufacturing constraints include surface finish requirements, tolerances, lead time, and mass production suitability. Often a combination of several manufacturing methods may be used simultaneously to create a complete cold plate, but this varies based on complexity. It is critical to understand and consider the production rate and capacity when choosing a manufacturing technique. Fig 3.3 gives a general outline of some standard methods and when a designer might opt to use a particular method of manufacturing. This figure includes electrical discharge machining (EDM), powder injection molding (PIM), 3D printing, machining, and casting. Fig. 3.3 is not an exhaustive list, and other alternatives are possible, including stamping, forging, extrusion, and more. For more information on any of these manufacturing methods, see the papers by Seyed [73] or Jasperson et al. [74].

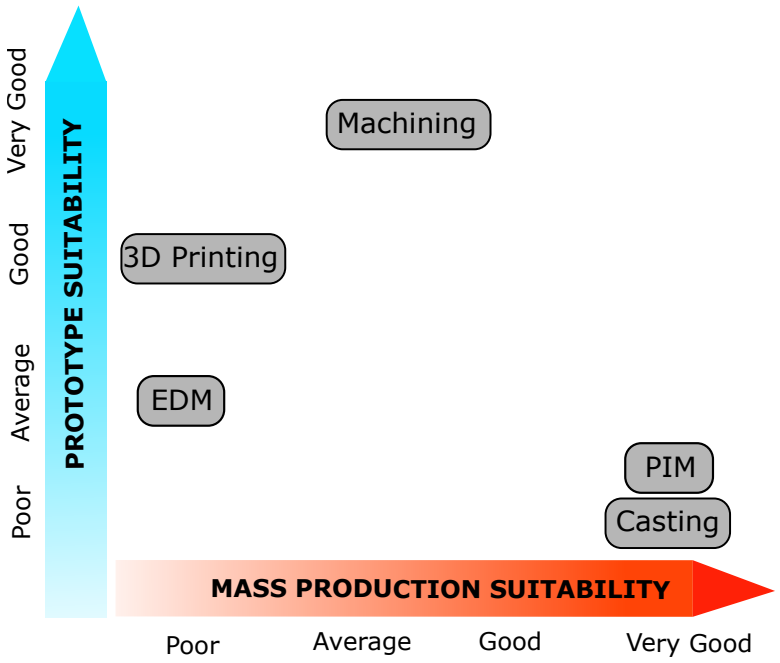

Figure 3.3: Production Suitability for Cold Plate Manufacturing (Adapted From [74])

Due to this project being in the prototyping stage, only machining and 3D printing were covered in detail within this thesis. These options are the most straightforward, cost-effective solutions. Additionally, the full-sized converter cold plate (version 2.0) would be a relatively low production item. If ever higher production was required, the design should require very few (if any) changes to make this possible. Further extensions to this paper could explore state-of-the-art manufacturing techniques to improve the cold plate performance.

3.1.2.1 Machining

Machining is a term that broadly refers to many different material removal processes. Milling, drilling, turning, boring, grinding, and cutting are typical machining processes. Creating a single cold plate design often requires a combination of these

processes. Each new machining project begins with a block of material commonly referred to as a blank. This raw material will undergo various material removal processes to obtain the final product. A computer numerically controlled (CNC) milling machine is one standard tool typically used in industry. This machine is versatile and can be pre-programmed to complete all steps without user intervention. This machine can automatically switch between cutting bits, grinding bits, and drilling bits, all without pausing the build. This autonomy saves a considerable amount of time since it prevents the engineer or machinist from stopping the machine and changing bits. CNC machines can also directly connect to computer-aided design/computer-aided manufacturing (CAD/CAM) systems [75]. CNC machines' tolerance is also very tight, making this a desirable manufacturing method. CNC machine operators/ shops usually charge an hourly rate, so designing the part smartly and efficiently is essential. Doing this can reduce overall machine run time as well as setup times. Additionally, the more machining operations the workpiece undergoes directly correlate to the product's final cost.

3.1.2.2 Additive Manufacturing

Additive manufacturing (AM) is a growing research area for cold plate design and manufacturing. Also called 3D printing, this process involves fabricating cold plates in a layer-by-layer approach based on a 3D CAD model. One massive advantage to AM is that the inner channel dimensions and geometries can be optimized to produce the best heat transfer possible. This optimization can produce highly complex geometries, which are not feasible with conventional manufacturing. Additionally, AM can create a single-piece cold plate, improving reliability by eliminating the need for

welding or joining interfaces, which increases the risk of leakage.

Unfortunately, there are also some drawbacks to AM, which slows the adoption of this technology. These drawbacks include porosity and cracks, mechanical stresses, and grain boundaries. It is essential to carefully choose the laser parameters and suitable materials to minimize cracks and grain boundaries [76]. Additionally, heat treatment combined with high pressure can limit defects and potential leak paths in the plate introduced by porosity [77]. In the paper by Cove et al., selective laser melting (SLM) was used to create the prototype parts. They used different internal geometries to investigate various 3D printed designs regarding temperature distribution and pressure drop. This study concluded that using SLM to create cold plate geometries was viable and effective and withstand mechanical clamping pressures found in press-pack assemblies [78].

In another study by Wong et al., SLM was used to manufacture three unique heat sink configurations: circular, rectangular-rounded, and aerofoil style fins. The manufactured heat sinks exhibited a high relative density of 99.1% and good dimensional accuracy. After conducting the tests, Wong et al. found that the cylindrical heat sink performed the worst of the three designs. They found a 15% and 21.4% improvement in average Nu_t for the rectangular-rounded and aerofoil heat sink geometries, respectively [79].

One crucial consideration when 3D printing is finding a way to expel the residue powder. This powder is a by-product of the print and must be flushed out with compressed air to avoid channel clogging and fouling. Therefore, additional holes may need to be created to expel this powder. These exit holes become especially critical when printing a single-piece design since the designer does not have access to the

internal channels. An x-ray may be used for more complex designs to verify that all powder has been removed before introducing coolant into the system.

3.1.3 Manufacturability Concerns/Considerations

3.1.3.1 Corrosion Prevention

One of the most critical factors to consider during cold plate design and manufacturing is leakage prevention. The most significant cause of leakage is galvanic corrosion which occurs when dissimilar metals are in direct contact. When this situation occurs, the passive metal (cathode) drives the corrosion of the active metal (anode) while remaining intact. The amount and speed at which corrosion occurs depend on the nobility of each material in contact. Many online references exist which show common materials and their respective nobility values. The more significant the difference of nobility between the two materials, the faster galvanic corrosion will occur. Whichever of the two materials is the least noble; this material will act as the anode and experience galvanic corrosion [80]. Another consideration to keep in mind is that the larger the cathode relative to the anode, the faster the anode will corrode.

To minimize corrosion, it is critical to choose materials that are as close together as possible on the galvanic series. If this is impossible, adding an isolating washer can be a viable alternative to separate two dissimilar metals. Using paint as a method of isolation is also viable; however, any crack or imperfections in the paint may become a point of significant corrosion.

Alternatively, a 'sacrificial anode' can be utilized to limit the amount of corrosion. This anode is composed of a material with a much lower nobility than the part which needs to be protected against corrosion. Thus, this material will become the anode

in the system, making the part to be protected a cathode. This switch-up will cause corrosion to occur on the sacrificial anode and not on a vital part of the assembly. These sacrificial anodes must be replaced periodically to prevent corrosion buildup.

3.1.3.2 Coolant Selection

Lastly, corrosion inhibitors are an effective tool to limit the effects of corrosion. These inhibitors usually include chemical additives, which are added to the coolant to reduce the corrosion rate. A combination of glycol and water solutions are standard coolants found within cold plates. The two most common types of these found in the industry are water-ethylene glycol (WEG) and propylene glycol-water (PGW) solutions. Water-ethylene glycol exhibits desirable thermal properties such as high boiling and freezing points, good thermal stability, high specific heat, and decent thermal conductivity. However, these benefits come at the cost of reduced thermal performance compared to water. The alternative, PGW, has less desirable physical properties than EGW. However, it is not a toxic substance, suitable for food processing and working in enclosed spaces.

De-ionized (DI) fluid is another promising cooling medium due to its improved heat transfer relative to water. De-ionized water is simply water that has had its ions removed: these ions usually come in the form of minerals, salts, or other impurities. This material has good electrical isolation properties since the ions that transfer electrons get removed in the de-ionization process. However, DI fluid has a very high resistivity resulting in a high corrosiveness. This corrosiveness makes it unsuitable for most copper/aluminum applications since corrosion would be a significant failure mechanism. Stainless steel tubing is required to implement a DI fluid in a cold plate

since this has better corrosion resistance properties.

On the other hand, a power electronics engineer might opt for a dielectric fluid. This fluid is non-conductive, making it an attractive alternative to water. A dielectric fluid's primary goal is to prevent or rapidly quench any electrical discharges which occur. One standard class of dielectric fluids is fluorocarbons. Fluorocarbons are typically non-flammable, thermally stable, and non-explosive. However, these coolants have significantly reduced thermal conductivity and high costs [81].

Before installing a cold plate next to sensitive electronics, it must undergo a leak test. The most common leakage locations are drilled holes or areas with thin material cross-sections. Another common leakage location is the brazing, joining, or welding location. Visual confirmation is usually adequate to confirm a watertight seal with no leakage. For more accuracy, Gary Stefani used two flow meters in his setup, each producing an electrical output signal proportional to the flow rate. He compared these two flow rates, and if they vary at any point in time, this will signal a system leak. The system he produced could respond in approximately two seconds and sense leaks of as little as $4\frac{mL}{minute}$ [82].

3.1.3.3 Tolerances

Many tools used in the manufacturing process have very tight tolerances. The commonly used CNC machine has a +/- 0.125mm tolerance, suitable for most applications. Precision tooling can achieve even tighter tolerances of +- 0.050mm, all the way to +/- 0.025mm, but the associated costs will increase dramatically at each level of decreasing tolerance. Tight tolerances dictate why micro-channel designs are more expensive than larger channels since specialized tooling is required to achieve such

tight tolerances. Simultaneously, machine run times will inevitably increase since less material gets removed with each pass. It is essential to factor machine tolerances into designs and specify tight tolerances only for critical locations such as holes and mating faces.

Often, an engineer will designate specific hole locations, depths, dimensions, milled paths, bosses, edge features critical to the operation or function of the part. These are often given the 'Critical to Function' or 'Critical for Design' labels, implying that a machine shop pays special attention to these callouts. Each callout comes at an additional cost since hitting these specific targets requires more setup time or additional tooling/fixtures. A fixture refers to any tooling in the manufacturing process to secure the workpiece during processing. Fixtures can include locating pins, clamps, supports, or braces to securely clamp the part in place and ensure the manufactured part's accuracy.

3.1.3.4 Fasteners

Using fasteners is common in cold plate designs, often connecting the base plate and the top cover. Most cold plates are at least two pieces because of ease of manufacturing. Having it in two pieces allows interior fins/pins or additional heat transfer enhancement geometry to get machined quickly and efficiently.

It is crucial to choose fastener material wisely to avoid galvanic corrosion. As mentioned in previous sections, galvanic corrosion occurs because of mismatched materials on the galvanic series. Therefore choose fasteners with material properties close to the cold plate material on the galvanic series. If not possible, look into fasteners

that include extra protective coatings. Coating these fasteners provides extra chemical stability and corrosion resistance, which are beneficial to the system's longevity. Isolating standoffs or washers can be a viable alternative if neither option is possible.

3.1.4 Joining Techniques

3.1.4.1 Gasket or O-ring

Besides permanent joining methods, o-rings and gaskets are the cheapest and easiest ways to join a cold plate. Using fasteners to secure the two pieces together with the gasket or o-ring sandwiched in between provides sufficient sealing. This simple setup is beneficial for prototyping since the parts can be taken apart and modified as the design process continues. When using fasteners, it is vital to have them outside of the liquid loop whenever possible to minimize the chance of leakage. A simple example of such a design can be found in the work by Charboneau [83].

In a situation where fasteners (or fittings) must get installed within the cooling loop, it is essential to take the proper precautions to avoid leaks. A standard method is Teflon tape (or equivalent) to seal any threads. When using Teflon tape, it should be applied to the male end of the fitting or fastener and wrapped counterclockwise so that it will not unravel when the fastener is tightened. Typically this tape is wrapped up to three times around the thread to make sure it will seal properly. This tape works as a deformable filler and thread lubricant to fill any gaps in the thread, preventing leaks.

3.1.4.2 Vacuum Brazing

Brazing is a material joining process in which molten filler metal (the braze alloy) gets heated above its melting point. Once melted, the filler/braze material is either drawn or distributed by capillary action into the desired areas. Next, the part is brought back down to room temperature, where the braze material will harden, forming a secure bond with the part. There are a wide variety of different brazing techniques, including torch brazing, furnace brazing, silver brazing, braze welding, vacuum brazing, and dip brazing, to name a few.

Vacuum brazing is becoming more popular for cold plates, so it will be explored further in this section. This technique uses a vacuum furnace to achieve precise temperatures without overshooting. This precise temperature control allows the alloy to melt in a controlled manner and avoids oxidation and corrosion. If this material does not flow properly, this will cause gaps to be inadequately filled, leading to potential leakage issues.

Using vacuum brazing to join pre-made fin stock to a cavity in the cold plate base is very common. The brazing gets applied to the fin stock's sidewalls and the recessed cavity's sidewalls manufactured in the cold plate base plate. When heated, the brazing alloy flows downwards, successfully joining the parts. However, sometimes the brazing material can overshoot, and some brazing material overflows into the flow passages [3]. This overflow can be detrimental to the system's heat transfer and pressure drop performance because of partial channel blockage. However, using a brazing operation to secure the cover plate onto the base plate is common since it eliminates fasteners, thus decreasing the risk of leakage. Akselband et al. used this technique to create two copper vacuum brazed cold plate designs; dual-sided copper

etch, and single-sided copper etch [84].

3.1.4.3 Friction-Stir Welding Technique

Traditional welding joins two parts via the fusion of a filler material between the two parts. Contrarily, friction stir welding (FSW) is a solid-state joining process. In this process, a rotating tool applies a downward force to the workpiece along the intersecting line of the two pieces (Fig. 3.4). The tool uses frictional heat generated by the rotating tool shoulder to soften the material near the joint. Then the probe or pin mechanically stirs the material at the joint, causing an intermixing between these materials, forming a solid bond. The resulting mechanical properties of an FSW joint are preferential to typical fusion-type welding. A study by Mistikoglu et al. observes superior weld profile and surface quality using friction stir welding [85]. Some other advantages of FSW include [86]:

- Fewer defects due to hot cracking, solidification cracks, and porosity
- Reduced shrinkage and distortion due to low temperature joining
- No filler material or shielding gas required
- Environmentally friendly, energy-efficient, repeatable process, with low operation costs

However, there are some downsides to using FSW. For example, FSW requires a minimum material thickness; therefore, fin stock or other small cross-sectional inserts are no longer viable. The paper by Thomas et al. outlines several more flaws of using FSW as a joining technique which includes:

- Exit hole is left where the tooltip gets withdrawn
- Significant clamping force and fixtures are required to secure the workpiece
- Slower welding speeds compared to conventional welding methods
- Tool wear

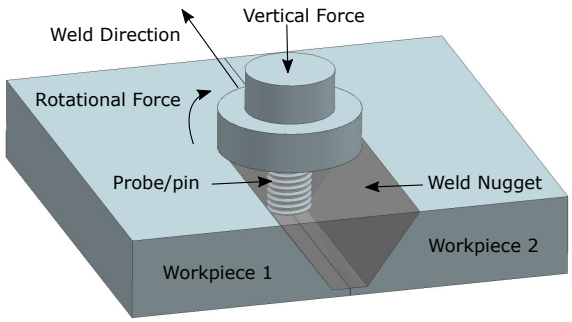

Figure 3.4: Friction Stir Welding Process

As this paper by Thomas et al. shows, while FSW has promising results, more work and study needs to be done in this field. This work includes applying this joining technique to dissimilar materials. For example, a study by Lakshminarayanan et al. investigates joining an aluminum-copper interface using friction stir welding. After successful manufacturing, CFD is used to validate the cold plate thermal performance [87]. Another paper by Hori et al. compares two cold plate designs: 1) a cold plate joined using traditional fasteners, 2) a cold plate joined using FSW. Results show that the FSW cold plate had a 30% increase in thermal performance compared to its bolted cold plate counterpart [88]. FSW is a viable joining technique often used in aerospace, automotive, and shipbuilding industries since it creates strong, permanent bonds without utilizing fasteners.

3.2 Inlet and Outlet Location/Configuration

Inlet and outlet location/configuration has a critical impact on the fluid flow, significantly affecting the cold plate performance. The inlet/ outlet geometry can also significantly affect the flow distribution of the cold plate. The paper by Kumaran et al. conducts multiple simulations with varying header shapes (rectangular, trapezoidal, and triangular) and header sizes. Additionally, the inlet and outlet locations were varied to study various cold plate configurations. This paper explores I, C, V, Z, and U inlet/outlet flow configurations to study the effect on the flow. There were several outcomes to this study.

First, the triangular inlet header provided the best flow distribution of the three geometries, while the optimal outlet geometry was the trapezoidal shape. They observed that the maldistribution decreases as the header increases in width. When it comes to the different inlet/outlet configurations, the flow distribution is better for the C-type and inadequate for the V-type arrangements. Because of its symmetrical design, the I-type arrangement has a symmetrical flow distribution; however, it also experiences a very high pressure drop. On the other hand, the U-type configuration has a relatively low pressure drop [89]. As these results show there is not a 'one size fits all' solution when it comes to cold plate designs.

A similar study by Chein and Chen looked at different inlet/outlet arrangements and the effect on the heat sink's fluid flow and heat transfer performance. They looked at six different arrangements: I, N, D, S, U, and V-type configurations. The paper concluded by suggesting that the V-type design performed the best when using thermal resistance, overall heat transfer coefficient, and pressure drop as performance criteria [90]. Several other papers have obtained comparable results [91] [92].

3.3 Channel and Header Geometry

In a study by Gunnasegaran et al., they investigated the effect of the channel geometry on the fluid flow and thermal performance using a micro-channel cold plate. The study covered three different channel geometries: rectangular, trapezoidal, and triangular, to see which would perform best. They concluded that the rectangular-shaped micro-channel design performed best for this specific application, followed by trapezoidal and triangular-shaped micro-channels with respect to overall heat transfer [93].

Another paper by Cho et al. studied the differences between micro-channel heat sinks with rectangular and trapezoidal headers with either straight or diverging channels. Additionally, they tested each micro-channel design under both uniform and non-uniform heat fluxes to see its effect on the system. Results show that when comparing straight vs. diverging microchannels, the straight channels show less temperature sensitivity to varying header shapes. However, the straight channels also experienced a higher pressure drop. Contrarily, the trapezoidal header design with diverging microchannels resulted in the lowest pressure drop. However, this design resulted in poor temperature distribution. This study concluded that the trapezoidal header with diverging channels was the best choice for this application, given its acceptable pressure drop and favorable temperature distribution [94]. While it did not record the most uniform temperature distribution, it is a good trade-off between the two variables; a concept that is critical when designing a cooling solution.

3.4 Flow Maldistribution

A common misconception when designing cold plates is assuming uniform fluid distribution throughout the interior channels. In actuality, flow maldistribution is very common within the flow channels of the cold plate. Flow maldistribution is a phenomenon defined as the non-uniform distribution of the mass flow rate within the liquid cooling loop. This maldistribution is an issue since it alters the cold plate's performance and significantly reduces heat transfer capabilities. Maldistribution often occurs within the channels because of varying channel dimensions. Some causes of this are manufacturing imperfections or tolerance stack-ups within machining. Alternately, brazing or soldering material may flow into the channels causing partial blockages for some cold plate designs. Maldistribution may also be induced by poor header or manifold design, causing unequal coolant flow into the various channels [95]. Complications from these issues may cause an increase in pressure drop and a reduction in the heat transfer rate of the cold plate.

3.4.1 Mitigation of Flow Maldistribution

In two papers by Liu et al. [63] and Lu et al. [91], they study the effect of various inlet and outlet locations on the cold plate performance. Both papers look at five different inlet/outlet configurations, and results show the velocity maldistribution, pressure drops, and temperature fields caused by each respective inlet/outlet combination. An interesting study by Liu and Yu investigated nonuniform mini baffles within the heat sink to aid flow distribution between the various channels. Simulation results show that these baffles can reduce the total thermal resistance of the heat sink by 9.9 - 13.1% [96].

Lastly, a study by Peng et al. worked to improve flow distribution by implementing a novel header design. This design incorporated a triangular transition duct with splitter plates to direct the flow as desired. The optimal number of splitter plates for the application was nine when using flow maldistribution, pressure drop, and structural constraints as the decision criteria. Their results show significant decreases in flow maldistribution and pressure drop by 91.5% and 40.9%, respectively [97].

Chapter 4

Cold Plate Design Tool

4.1 Pin Fin Cold Plate Equations

4.1.1 Staggered Configuration

Fluid Velocity: The first critical parameter to be calculated is the fluid velocity. This velocity will determine whether the fluid flowing through the cold plate falls within the laminar, transitional, or turbulent range. This velocity calculation is based mainly on the fin arrangement being used. The general workflow of staggered and aligned pin fin configurations are the same; however, there are some minor differences. The velocity is directly correlated to the pitch between fins and the fin diameter for pin-fin arrangements. The maximum fluid velocity (V_{max}) gets calculated based on the entire bank of pin fins.

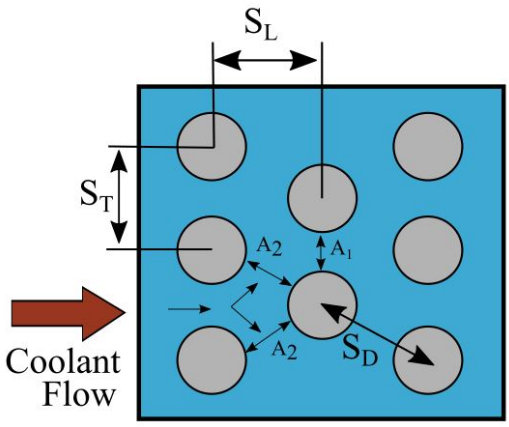

Figure 4.1: Top View - Staggered Configuration

The location of this V_{max} differs based on configuration (aligned vs. staggered). The V_{max} can be at two different locations for the staggered configuration: 1) plane A_1 or 2) the diagonal plane A_2 (Fig. 4.1). To determine on which plane V_{max} will occur, the following condition gets tested:

$$S_D = \left[(S_L)^2 + (\frac{S_T}{2})^2\right]^{1/2} < \frac{S_T + D}{2}, \tag{4.1}$$

where S_D, S_L, and D are the diagonal pitch, longitudinal (downstream) pitch, and transverse (cross-stream) pitch, respectively. If condition 4.1 is not satisfied, V_{max} is calculated at the transverse plane A_1. Due to conservation of mass for an incompressible fluid this gets calculated using:

$$V_{max} = \frac{S_T}{S_T - D} V, \tag{4.2}$$

where S_T, D, and V are the transverse pitch, fin diameter and fluid approach velocity, respectively. However, if condition 4.1 is satisfied, V_{max} is calculated at the diagonal

plane A_2 using:

$$V_{max} = \frac{S_T}{2(S_D - D)} V \tag{4.3}$$

Reynolds Number: Next, this V_{max} gets used to calculate the Reynolds number. The equation to calculate the Reynolds number is:

$$Re = \frac{\rho V_{max} D}{\mu}, \tag{4.4}$$

where ρ and μ are the density and dynamic viscosity of the coolant. D in this equation is the fin diameter. The calculated Reynolds number is essentially a ratio of the inertial forces to viscous forces. This ratio implies that the lower the Re ratio, the higher the viscous forces acting within the fluid; thus, velocity decreases. The opposite is true that when the ratio is high, the flow tends to have a higher ratio of inertial forces, causing the velocity to increase. The lower the fluid velocity, the more likely the flow will be in the laminar region, whereas fluid with a high velocity will most likely be turbulent in nature. This Reynolds number is critical since certain correlations are valid only over specific Reynolds ranges. There is some literature debate about where the fully turbulent region begins. This thesis assumes that the onset of turbulence will occur at Reynolds values of 2300 and higher.

Nusselt Number: After calculating the Reynolds number, if the value falls between these bounds: [1000 <= Re <= $2e^6$], the Zukauskas correlation can be used. The Prandtl number also must fall within [0.7 <= Pr <= 500] for the correlation

to be valid. This correlation is of the form:

$$\overline{Nu_D} = CC_2 Re_{D,max} Pr^{0.36} (\frac{Pr}{Pr_s})^{1/4}, \tag{4.5}$$

where C and C_2 are constants determined based on the spacing, diameter, and number of fins in the longitudinal direction. Both coefficients are [$0 <= C_1, C_2 <= 1$], ensuring that the system's heat transfer is not over-predicted. If the system undergoing design has less than 20 pin fin rows in the longitudinal (downstream) direction, then the C_2 term must be added; otherwise, this term can get removed from Eq. 4.5. Pr and Pr_s are the Prandtl number of the fluid and fin surface, respectively.

Convection Coefficient: After calculating the Nusselt number, the convection coefficient gets calculated next. This coefficient is a critical parameter that describes how well the cold plate transfers heat from the solid body into the coolant. This convection coefficient (h) gets calculated using:

$$h = \frac{NuK}{D}, \tag{4.6}$$

where K and D are the fluid's thermal conductivity and the pin fin diameter, respectively. The convective coefficient value will be compared between pin fin configuration to investigate which design exhibits superior cooling performance. The higher the convection coefficient value, the more heat will be extracted from the devices and transferred into the coolant.

Weight: Besides heat transfer, several other critical parameters still need to be calculated to accurately assess the cold plate's performance, including weight, pressure

drop, and pumping power. First, the weight is calculated by determining the entire cold plate volume and multiplying this by the density of the material used. Aluminum properties were used in this design; however, other materials can be added in future iterations.

Pressure Drop: Another critical parameter to calculate is the pressure drop. This parameter is vital since having a significant pressure drop may impede flow or cause unfavorable flow characteristics. Contrarily, a small pressure drop will decrease fluid velocity, negatively impacting heat transfer. Therefore, this pressure drop (ΔP) gets calculated using:

$$\Delta P = N_L \chi \left(\frac{\rho V_{max}^2}{2} \right) f, \tag{4.7}$$

where N_L is the number of rows in the longitudinal (downstream direction), χ is the correction factor, and f is the friction factor. The correction and friction factors are determined based on the literature's empirical curves [98]. It is essential to realize that this is a baseline pressure drop. It does not incorporate entrance or exit effects since there is a wide variability based on each individual design. Additionally, the increased pressure drop due to manifolds and splitters is not accounted for, again due to significant variability in potential design strategies.

Pumping Power: Pumping power (W_{pump}) is directly related to pressure drop and gets calculated using:

$$W_{pump} = \frac{\Delta P \, \dot{m}}{\rho}, \tag{4.8}$$

where $\dot{m}$ and ρ are the mass flow rate and fluid density, respectively. Again, the pumping power is directly related to the size and energy consumption of the pump.

The higher the pumping power, the stronger the pump must be and the higher the associated energy costs will be to operate it. A larger pump also inevitably means additional weight and higher initial costs to purchase. Small weight savings in cold plate weight will be negligible if the pump size increases, thus increasing the net weight of the system.

4.1.2 Aligned Configuration

The aligned configuration is almost identical to the staggered configuration calculations (section 4.1.1). The primary difference is the changes to the V_{max} calculation. In this case, there is only one location where V_{max} will occur, which is the transverse plane A_1 (Fig. 4.2). At this location the V_{max} gets calculated using Eq. 4.2. For both the aligned and staggered configurations, equations for a bank of tubes/fins get used to calculate the average convection coefficient. Tube bank equations must get incorporated since the fluid flow, and heat transfer will change throughout the fin array. For example, the first row in the tube bank will have a lower convective coefficient approximately equivalent to a single pin fin in crossflow. As the fluid progresses through the fin array, fins in subsequent rows will benefit from induced turbulence created by the first several rows. This effect will continue for approximately five rows, after which this effect is negligible. For this reason, an average convective coefficient is used for the calculations to ensure optimal accuracy.

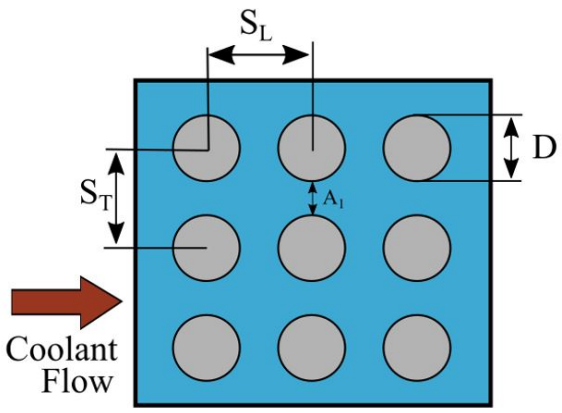

Figure 4.2: Top View - Aligned Configuration

4.2 Toolbox

A MATLAB cold plate design tool was created in this thesis to automate the cold plate design process. This tool dramatically reduces design time by proposing a baseline design given some generic inputs. This baseline design can then be refined based on packaging constraints and specific device layout for each application. This tool was designed to be intuitive and user-friendly, making it suitable for various applications. In this thesis, the design tool proposed a baseline cold plate design for a DC-DC converter application. The subsequent sections explore the design process, all the way from conception to the proposed cold plate design.

To begin the design process, the user must input several generic parameters. These include the number of heat sources on each side and the power dissipated from each heat source. This code can be adjusted for both single-sided and double-sided cooling; single-sided was used in this thesis. Next, the user sets the fluid properties based on the type of coolant used at an initial temperature. These properties include density, heat capacity, dynamic viscosity, thermal conductivity, and Prandtl number.

Next, the cold plate material density and thermal conductivity will be set, depending on the material. Then the volumetric flow rate and inlet temperature are set by the user. Lastly, the outer dimensions of the cold plate get set based on the maximum allowable package size.

4.3 2D Thermal Model

A vital part of the MATLAB tool is obtaining accurate temperature values for the various interface layers within the electronics package. These temperature values allow the user to ensure that the power devices are not exceeding their critical junction temperatures, resulting in component failure. Additionally, the user can use this information to source parts. For example, suppose a significant spike in temperature occurs over the thermal interface material layer. In that case, this could indicate that the designer should explore alternate TIM solutions such as a pad or grease with lower thermal resistance.

To create a thermal network to capture this temperature distribution, a 2D resistance circuit is created. This circuit contains a series of resistances that simulate the different layers in the mechanical setup. These layers include the resistor die, thermal interface material (TIM), and the aluminum cold plate. The heat flow through the package is relatively straightforward. The heat is generated from the resistors and transferred through the thermal pad into the cold plate. From here, the heat is transferred through the fins into the coolant through convection. The circuit in Fig. 4.3 and Fig. 4.4 show all resistances used. The first resistance to consider is R_{die}, which is the resistor's internal (die) resistance. This value is given in the product specifications by the manufacturer. If no specifications are provided, in-house testing

is the next best thing.

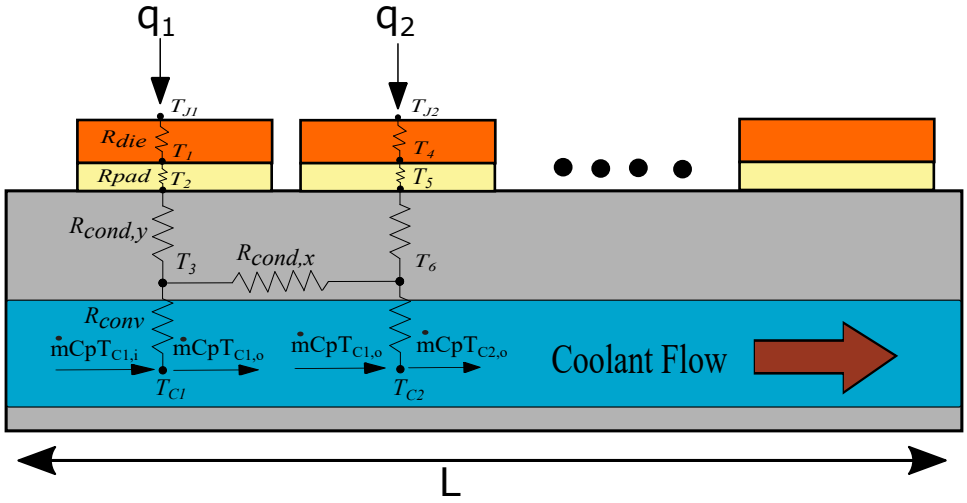

Figure 4.3: Cold Plate Side View With Overlayed Thermal Network

Next, it is essential to calculate the resistance due to the TIM. For this paper, thermal pads are used and are denoted as R_{pad}. Lastly, Fig. 4.3 and Fig. 4.4 show both the conductive ($R_{cond(x,y)}$) and convective resistances (R_{conv}) used in the resistance circuit. Conduction occurs within the cold plate body and is highly dependent on the material used. For this thesis, conduction in the x (parallel to fluid flow) and y (perpendicular to fluid flow) will occur and get denoted as $R_{cond(x,y)}$. Due to limited heat transfer via conduction in the z-direction and the high uniformity of the cold plate, the z-direction was deemed negligible. This simplification reduced the complexity and number of calculations significantly while accurately capturing the system's temperature distribution.

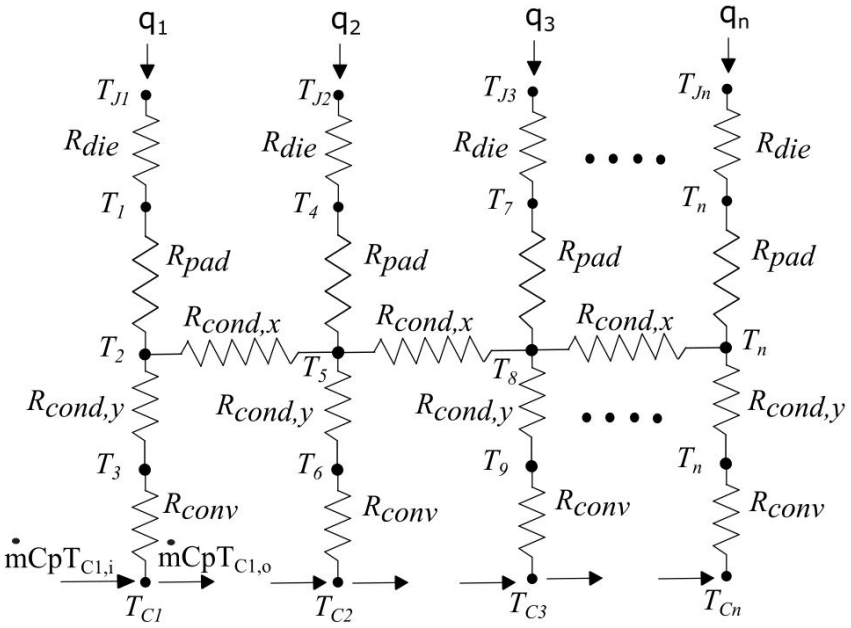

Figure 4.4: Expanded Resistance Circuit - n Resistors

To calculate the temperature distribution throughout the cold plate, the cold plate is discretized into nodes. Then the energy balance at each node is formulated using energy conservation principles. For example, the energy balance at node T_{J1} gets calculated using the principle of 'heat in equals heat out' (q_{in} - $q_{out} = 0$). Therefore, for node T_{J1} the energy balance is formulated as:

$$q_1 = \frac{T_{J1} - T_1}{R_{die}} \tag{4.9}$$

where q_1 is the heat dissipation from the first resistor, and T_{J1} and T_1 are the junction temperature one, and temperature at node one, respectively. Since we know the losses of the resistor, q_1 is a known variable. A similar procedure gets conducted to create the second row of the matrix. The only difference is that the energy balance now

occurs at node one. The resulting equation is as follows:

$$\frac{T_{J1} - T_1}{R_{die}} = \frac{T_1 - T_2}{R_{pad}} \tag{4.10}$$

Since q_{in} - $q_{out} = 0$ for all nodes, Eq. 4.10 can be rearranged to form:

$$\frac{T_{J1} - T_1}{R_{die}} - \frac{T_1 - T_2}{R_{pad}} = 0 \tag{4.11}$$

This exact process gets conducted for nodes T_{J1}, T_1, T_2, T_3, and T_{C1} as depicted in Fig. 4.3. Node T_{C1} is noteworthy since it considers the fluid's mass flow rate and heat capacity and has two equations. The energy balance at node T_{C1} is:

$$\frac{T_3}{R_{conv}} - \frac{T_{C1}}{R_{conv}} = \dot{m} C_p (T_{C1,outlet} - T_{C1,inlet}) \tag{4.12}$$

Also at node T_{C1}, it is known that the coolant outlet temperature is an average of the inlet and outlet temperatures. The following equation shows this relationship:

$$T_{C1} = \frac{1}{2}(T_{C1,inlet} + T_{C1,outlet}) \tag{4.13}$$

Once all equations are formulated, the system of equations gets put into matrix form. The left sides of the equations are combined to form the 'A' matrix, whereas the right-hand side of the equations forms the 'B' vector. The vector of unknown temperatures in the thermal network get denoted by the 'T' vector. 'A', 'B', and 'T' get combined into standard form for linear equations of $Ax = B$, where 'x' is the 'T' vector in this situation.

$$\underbrace{\begin{bmatrix} \frac{1}{R_{die}} & \frac{-1}{R_{die}} & 0 & 0 & 0 & 0 \\ \frac{1}{R_{die}} & \frac{-1}{R_{die}} - \frac{1}{R_{pad}} & \frac{1}{R_{pad}} & 0 & 0 & 0 \\ 0 & \frac{-1}{R_{pad}} & \frac{1}{R_{condy}} + \frac{1}{R_{pad}} & \frac{-1}{R_{condy}} & 0 & 0 \\ 0 & 0 & \frac{1}{R_{condy}} & \frac{-1}{R_{condy}} - \frac{1}{R_{conv}} & \frac{1}{R_{conv}} & 0 \\ 0 & 0 & 0 & \frac{-1}{R_{conv}} & \frac{1}{R_{conv}} & \dot{\mathbf{m}}C_p \\ 0 & 0 & 0 & 0 & 2 & -1 \end{bmatrix}}_{\mathbf{A}}$$

$$\underbrace{\begin{bmatrix} T_{J1} \\ T_1 \\ T_2 \\ T_3 \\ T_{c1,i} \\ T_{c1,o} \end{bmatrix}}_{\mathbf{T}}$$

$$\underbrace{\begin{bmatrix} q_1 \\ 0 \\ 0 \\ 0 \\ \dot{\mathbf{m}}C_pT_i \\ T_i \end{bmatrix}}_{\mathbf{B}}$$

To solve for the temperature 'T' vector, the system of linear equations must be solved simultaneously. Within MATLAB, this can be completed via a '\' operation, which outputs the resultant 'T' vector. This 'T' vector gives the temperature at each

node in the thermal network.

$$\begin{bmatrix} A \end{bmatrix} \begin{bmatrix} T_{J1} \\ T_1 \\ \vdots \\ T_{c1,o} \end{bmatrix} = \begin{bmatrix} B \end{bmatrix} \tag{4.14}$$

4.3.1 Thermal Resistance

Thermal resistance is vital to consider when designing cold plates and reporting their cooling ability. This property is a measurement of a material's resistance to heat flow. The higher the thermal resistance, the less heat passes through (i.e., the material is a better insulator). The thermal resistance is simply the temperature change (ΔT) divided by the total heat generated between any given two points. The entire cold plate thermal resistance ($R_{th,j-a}$) can be an essential metric to track. This metric outlines the expected performance of the cold plate and is calculated using:

$$R_{th,j-a} = \frac{T_j - T_a}{Q} - R_{die} - R_{pad} - R_{cond(x)}, \tag{4.15}$$

where T_j, T_a are the device junction temperature and ambient (coolant) temperature, respectively. R_{die}, R_{pad}, and $R_{cond(x)}$ are the interface layers as outlined in Fig. 4.3 and Fig. 4.4. After conducting all experiments, the resultant cold plate thermal resistance vs. flow rate is plotted in Fig. 6.9.

4.4 GA Algorithm

For this MATLAB tool to be beneficial, the tool must include parameter optimization to achieve an optimal design. An optimal design incorporates a favorable weight, junction temperature, and pressure drop trade-off. For this reason, these criteria will serve as the objective functions that must be minimized. These objective functions must be optimized simultaneously, even though some are conflicting objective functions (i.e., if the weight decreases, the temperature will increase since there are fewer fins for heat transfer). Contrarily, as the pressure drop increases, the temperature will decrease due to the addition of fins.

To solve this optimization problem, the three single objective functions (weight, junction temperature, and pressure drop) get converted into a multi-objective function. The paper by Konak et al. explains some standard methods to accomplish this and provides additional references for each method [99]. The multi-objective GA uses the weighted approach to solve the problem in this MATLAB tool. Each function gets evaluated individually, and its fitness value gets recorded. In all cases, the fitness is defined simply as 'the negative of the objective function.' Once the weight, pressure drop, and junction temperature fitness values get calculated, they get combined into a single multi-objective function. This combination gets completed using heuristic coefficients to denote that specific parameter's importance or "weight." These heuristic coefficients will be a positive value if maximizing an objective function; otherwise, the coefficient will be negative. The weight, pressure drop, and temperature will all be minimized for this thesis. Therefore, the combined objective function can be formulated as:

$$Min\ y = -w_1 y_1(x) - w_2 y_2(x) - w_3 y_3(x), \tag{4.16}$$

where $y_1(\mathrm{x})$, $y_2(\mathrm{x})$, $y_3(\mathrm{x})$ are the first, second and third objective functions, respectively. For this problem, the weight w_i must be assigned by the user. This approach is commonly referred to as the priori method since it requires the user to input the weight values prior to running the script. This initialization can be tricky, as it is sometimes unclear what "weight" to assign to each objective function. Therefore, these coefficients must be explored heuristically (i.e., by trial and error) to decide which value of coefficients to use.

For this project, since the cold plate is designed for aerospace applications, the weight will be given primary or 100% importance. Therefore, the user input for the w_i coefficient is 1 within the multi-objective equation (Eq. 4.16). After trying different combinations of pressure drop and junction temperature importance or "weight," both values get set to 75% importance. These settings indicate that the primary objective of the genetic algorithm will be to minimize weight, and the two other functions will have slightly less influence on the function. Therefore w_2 and w_3 coefficients will be 0.75 and 0.075, respectively. The reason w_3 is 10x smaller is because the fitness values from the temperature objective function are an order of magnitude off from the others. If this adjustment does not occur, the temperature function would have the most significant impact on the combined objective function.

The workflow of the genetic algorithm (GA) is shown in Fig. 4.5. First, the user sets the constant parameters of the material and fluid, along with any other known information. Then the population is initialized randomly by generating a set of chromosomes (points). The GA evaluates each point for its respective fitness. Points with higher fitness are optimal since they minimize the objective function more effectively. Then a selection process is carried out, in which parents with higher fitness values

are more likely to reproduce, as is often the case in nature. Next, crossover occurs, where the reproduction between two chromosomes occurs. The concept here is that fitter parents pass their "fit" genes or chromosomes to their children to produce an even fitter population in the second generation.

After completing crossover, a mutation operation will occur to a tiny percentage of the points. This mutation process will randomly alter some of the chromosomes, which will aid in exploring new areas in the parameter space and help avoid local minima.

This entire process will continue in a loop until the current generation equals the maximum number of generations (Fig. 4.5). The optimal points get recorded for each successive generation. These optimal points will have the best weight, junction temperature, and pressure drop trade-off compared to the alternative options. After the algorithm completes, the user decides which point is best, given the project constraints. After picking the best point, the parameters to achieve that performance are used to propose the cold plate design.

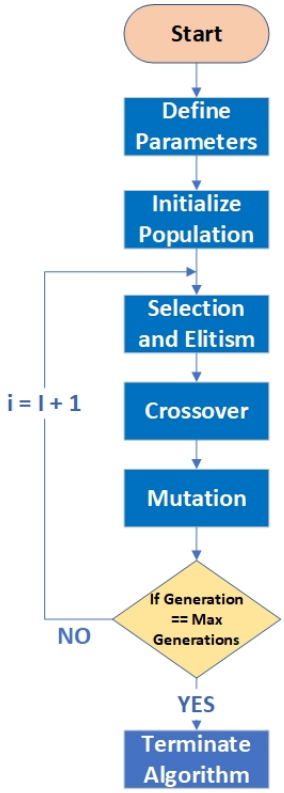

Figure 4.5: Genetic Algorithm Workflow

4.5 Design Requirements

4.5.1 Electrical Layout

The electrical layout used in this paper is loosely based on a high-powered DC-DC converter used for aerospace applications. In a future design, all converter electronics will be cooled on a single cold plate. This cold plate will be much larger and include electronics on both sides of the cold plate that require cooling. However, since the electronic locations and types were not finalized, a temporary, smaller prototype was created to validate the MATLAB tool and all correlations used. Therefore, the

electrical setup was also simplified. This simplified setup includes six total resistors that mimic the converters' MOSFETs. These resistors can dissipate significantly more power, and the power levels can be adjusted easily. A simple electrical circuit was created, putting three resistors in series within two parallel circuits, resulting in six resistors total. A constant voltage will be applied to each parallel path so that all devices will dissipate an equal amount of power. These devices were installed at the middle of the coolant channel and perfectly in line with each other so that testing results will be as accurate as possible. This 'standardized' test setup will allow easier identification of errors/discrepancies within the cooling system.

These resistors are through-hole resistors, with 10 ohms of resistance and power dissipation of up to 50W per device. This power dissipation is adjustable and will be adjusted during testing to verify the cold plate cooling ability. These devices are housed with the TO-220 package with dimensions of 10.1x15mm. These resistors have an operating temperature of -50 to 175°C, higher than the internal maximum set at 125°C. The thermal resistance of $2.3\frac{^\circ C}{W}$ was dictated by the manufacturer's specs and was inputted into MATLAB during evaluation. Further specifications are available on Digi-Key under part number 696-1331-ND.

4.5.2 Volume/ Packaging Requirements

Since thermal management was the last step in the design process, the volume requirements were already set. The outer dimensions of the cold plate must be 0.1524m in length, 0.1903m in width, and 0.018m in height. These dimensions give a total allowable cold plate volume of 5.22e-4m^3. These cold plate volume requirements are necessary to meet the complete converter package volume requirements to make this a

competitive product in the aerospace market. Any larger than this, and the converter will not fit within the confines of the aircraft. Since the outer dimensions of the cold plate are fixed, only the internal channels and fins can be optimized to achieve satisfactory performance. This volume must be reduced as much as possible throughout the design process to minimize the weight.

Packaging constraints dictated that the inlet and outlet must be on the same side and along the 0.1524m side of the cold plate. Unfortunately, this does limit the design possibilities slightly; however, this constraint was implemented during the design process. The inlet/outlet diameter was maximized so that the pressure drop would be reduced and the cold plate thermal performance would be increased.

4.5.3 Weight Requirements

The weights requirements are simple: minimize weight while maintaining cold plate thermal performance. Weight is crucial to the design since any added weight will reduce the carrying capacity of the aircraft. Additional weight will reduce the converter's power density, making it less desirable to consumers.

There are additional considerations regarding the cold plate weight that do not get covered in the weight calculation. First, the tool does not consider any extra fittings/ manifolds and tubing needed to direct the flow as desired. These can quickly increase the weight depending on the size, quantity, and material used. Fasteners are another thing which will increase the overall weight. Even though fasteners are often the easiest solution, these can also increase weight significantly.

Next, the tool does not consider accessory devices like the pump. As discussed

earlier, a larger pump may negate small decreases in a cold plate's total weight. Therefore a cold plate design must have a reasonable pumping power to avoid requiring a large pump. Lastly, the weight of the cold plate is the "dry weight." It is essential to understand that the cold plate cooling system will be heavier during operation due to the added weight of the coolant.

4.5.4 Power Density Requirements

It is integral to the research team at McMaster University to create a DC-DC converter with competitive power density specifications. There are several similarly-sized converters on the market that the group hopes to meet or surpass in terms of performance. The first generation (air-cooled) design created by the group at McMaster University is currently undergoing testing. However, it is on track to achieve better power density for a lighter overall converter than some competitors.

However, an issue with the air-cooled design is the large volume necessary because of the substantial size of the heat sinks. This volume makes it less desirable than some of the other designs on the market. A switch between air-cooled and liquid-cooled is required to reduce the overall package volume. This switch would reduce the volume and weight by eliminating the large off-the-shelf extruded aluminum heatsinks and replacing them with a much smaller cold plate design, which is the basis for this project. Further improvements are achieved by having this cold plate provide double-sided cooling. These changes will result in better overall power density for the converter, making it a more desirable product.

4.5.5 Modularity

Modularity plays a critical role in a cold plate design process. Modularity refers to how components and subsystems can be separated and recombined to form larger assemblies. Often engineers overlook this during the design process, focusing solely on weight and performance improvements. However, several studies investigate a modular cold plate design for automotive electronics cooling.

In the first study, Zhou et al. utilized mini/microchannels and jet impingement to obtain optimal cooling performance. They designed a manifold to optimize the flow distribution between three separated branches by varying the inlet and outlet diameters [100]. Another paper by Zhou et al. attempts to make this initial design more modular and reconfigurable. They split the cold plate into three separate modular components (since three electronic power modules required cooling). These modular components are then attached together using fasteners or snaps. The unique aspect of this study is the ability to reconfigure the flow based on packaging and cooling constraints. The study begins with a baseline case, a standard parallel flow U-shaped configuration with the inlet and outlet on the same side. Using a series of plugs, they altered the flow to create a Z-shaped flow configuration with an inlet/outlet on opposite sides, a serpentine flow, and a combination of series/parallel flow. Each configuration results in different temperatures, flow rates, flow distributions, and pressure drop distributions, making them suitable for various applications. After the design phase, the cold plate was 3D printed using PEEK plastic to reduce weight and improve the overall power density [101] [102].

4.6 Proposed Liquid Cold Plate Design

4.6.1 Base Plate Design

The prototype proposed in this thesis will be a small-scale version of the final cold plate design. This prototype will incorporate two flow channels, with three resistors centered over each channel. Two flow channels were necessary to measure the cooling discrepancies between channels. All devices must be cooled at equal rates since unequal cooling will result in unequal current sharing and reduce the converter performance.

The cold plate was designed in Siemens NX before importing into CFD simulations. First, a block of material was extruded for the base plate. This base plate height must be large enough to accommodate a reasonably sized main inlet/outlet diameter and still allow an o-ring groove to run overtop it, with enough material thickness in between. A $\frac{1}{8}$ NPT ($8.6132mm$) sized hole was selected in NX to be the main inlet and outlet hole diameter based on external fitting limitations. Any larger diameter would interfere with the o-ring, and any smaller than this would result in a very high system pressure drop.

Next, two channels were created directly under the heat dissipating device locations. After creating two channels, the main inlet and outlet were connected to the channels via five smaller inlet and outlet holes. These smaller holes will be referred to as the channel inlets/ outlets, whereas the single larger inlet/outlet will be referred to as the main cold plate inlet/outlet. The diameter of the channel inlet and outlet holes was set to $5mm$ initially. This diameter will be optimized in CFD to push equal (relatively) flow into each channel. This will be discussed in detail in section

5.2.2. These channel inlet/outlet holes were drilled at an angle from the top end of the cold plate. To accomplish this, the inlet/outlet face of the channel was chamfered at approximately 35 degrees from vertical. This chamfered face will allow a five-axis CNC machine to drill the 5x inlet/outlet holes perpendicular to this face.

Fin Configuration, Spacing, and Diameter: Once the base plate shape begins to take form, it is necessary to populate the inside of the channels with fins. These fins are the primary source of cooling for the cold plate. This process is completed using the tool created in MATLAB for this purpose. When all parameters were inputted into MATLAB, the code was run to compare the aligned and staggered configurations. All dimensions, velocity inputs, and fluid/material properties can be found in Table 4.1. It is important to note that the parameters in Table 4.1 are for the small-scale simplified geometry that is simulated in section 5.1.

A genetic algorithm (GA) was used within the MATLAB tool to determine the fins' optimal number and arrangement. First, the population size and the number of generations were set to 20,000 and 5, respectively. These parameters mean that 20,000 randomly generated points will be created between the upper and lower bounds of the dimensionless pitch (P_T) and the diameter (D). This high number of points will ensure that the values converge within a reasonable number of decimal places. The GA will run for five generations, and the best possible results for each successive generation will be recorded.

By incorporating the constraints of the dimensionless pitch (P_T) and the diameter (D), the fin efficiency is inherently incorporated into the calculations. Additional constraints within the MATLAB tool ensured that the flow rate and Prandtl number were within acceptable bounds to use the proposed correlations. Any result that did

not fall within the acceptable parameter bounds would be deemed an unsatisfactory design.

	Water Ethylene-Glycol	
Parameter	**Value**	**Units**
Density	1061	$\frac{kg}{m^3}$
Dynamic Viscosity	9.7725e-4	$\frac{Ns}{m^2}$
Thermal Conductivity	0.40	$\frac{W}{mK}$
Prandtl Number	8.7097	[ ]
Volumetric Flow Rate	5e-5	$\frac{m^3}{s}$
Specific Heat Capacity	3565	$\frac{kJ}{kgK}$
Coolant Inlet Temperature	30	°C
	Aluminum Cold Plate	
Parameter	**Value**	**Units**
Density	2710	$\frac{kg}{m^3}$
Thermal Conductivity	167	$\frac{W}{mK}$
Cold Plate Length	0.1144	m
Cold Plate Width	0.0800184	m
Cold Plate Height	0.018	m

Table 4.1: Simulation Parameters

After running the code, the results are shown in Table 4.2 for both the aligned and staggered configurations. For the first generation, the MATLAB results for the optimal aligned configuration are a 13x9 array of fins, with 13 fins in the downstream and 9 fins in the cross-stream direction. The pins are $3.7mm$ in diameter with a pitch of $7mm$ between the fins (center-to-center) distance. Similarly, for the staggered design, MATLAB suggests a 12x8 array of fins, with a fin diameter and pitch of 3.9 and $7.8mm$, respectively. The pin fins span the entire channel height for both configurations, initially giving them a $6mm$ height. This pin fin height gets reduced later in the design process to $5.5mm$ to ensure manufacturing intolerances do not result in inadequate sealing (section 6.1.1). Each successive generation result can be

found in Table 4.2. Note that the table values don't change between generations since the results have converged to an optimal solution.

ALIGNED CONFIGURATION				
Generation	**Pitch(m)**	**Fin Diameter(m)**	**Fins Longitudinal**	**Fins Transverse**
1	0.007	0.0037	13	9
2	0.007	0.0037	13	9
3	0.007	0.0037	13	9
4	0.007	0.0037	13	9
5	0.007	0.0037	13	9
STAGGERED CONFIGURATION				
Generation	**Pitch(m)**	**Fin Diameter(m)**	**Fins Longitudinal**	**Fins Transverse**
1	0.0078	0.0039	12	8
2	0.0078	0.0039	12	8
3	0.0078	0.0039	12	8
4	0.0078	0.0039	12	8
5	0.0078	0.0039	12	8

Table 4.2: Best Geometry Design - Aligned vs. Staggered Configurations

Lastly, the cold plate performance metrics that MATLAB calculated are recorded in Table 4.3. Each generation will result in specific values for weight, pressure drop, convection coefficient, and surface temperature. For example, the best possible results for the first generation of the aligned configuration correspond to a weight, pressure drop, convection coefficient, and surface temperature of $0.348kg$, $76Pa$, $4877\frac{W}{m^2K}$, and $31.052°C$, respectively. Across the generations, there are only slight variances in the values since the results have converged (within three or four decimal places). Additional generations and population points can be added; however, this is sufficiently accurate for this design. All results for each of the five generations for both configurations are found in Table 4.3. Extra decimal places were kept in the table to show the slight variances between the results of the five generations in MATLAB.

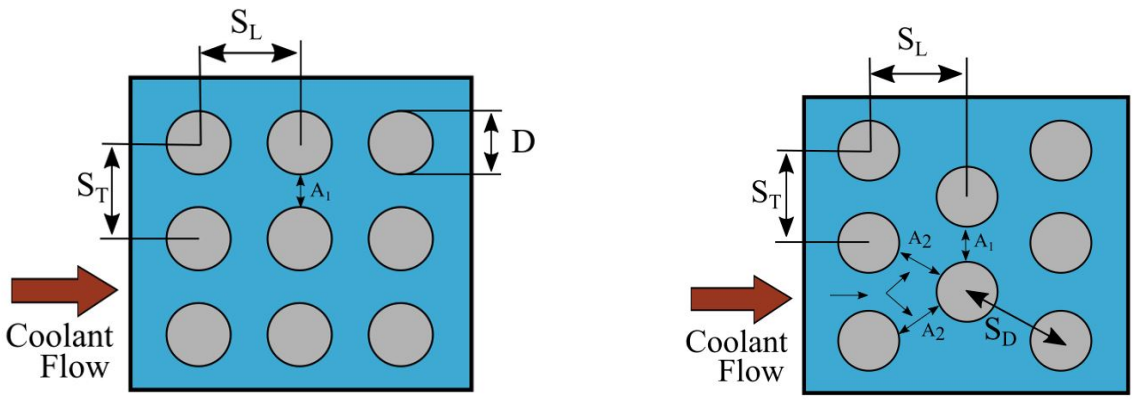

(a) Aligned Configuration (b) Staggered Configuration

Figure 4.6: Top View of Aligned/ Staggered Configurations

Aligned vs. Staggered Fin Comparison: After comparing the staggered and aligned configurations, the aligned configuration is chosen for the design. This decision is based on the numerical results of the MATLAB tool. First, the pressure drop is more significant for the staggered configuration. This increase is because the staggered design increases the resistance to the flow by having more fins obstructing fluid flow. The staggered configuration would typically increase heat transfer. However, this improvement is not always realized at low flow rates with mostly (or entirely) laminar flow. In this scenario, the fluid flow within the channel regions will be predominantly laminar at the pin fins where the heat transfer would occur. For this reason, the aligned configuration performs better under laminar flow conditions.

These results are clearly illustrated in the staggered configuration's convection coefficient and surface temperature values. The convection coefficient is lower, meaning less heat is being transferred from the devices into the fluid, resulting in slightly higher surface temperatures. Some very slight weight advantages are seen for the staggered configuration due to every other row having one less fin due to the offset nature of the

fin arrangement. An illustration of the proposed aligned fin configuration is shown in Fig. 4.6a.

ALIGNED CONFIGURATION				
Gen	**Weight (kg)**	**Pressure Drop (Pa)**	**Convection Coefficient($\frac{W}{m^2K}$)**	**Surface Temp (°C)**
1	0.3480	76	4877	31.052
2	0.3482	77.4	4888.5	31.048
3	0.3478	75.9	4882.1	31.049
4	0.3478	75.9	4882.8	31.049
5	0.3479	75.7	4877.2	31.052
STAGGERED CONFIGURATION				
Gen	**Weight (kg)**	**Pressure Drop (Pa)**	**Convection Coefficient($\frac{W}{m^2K}$)**	**Surface Temp (°C)**
1	0.3450	180.9	4613.4	31.490
2	0.3450	179.8	4608.3	31.494
3	0.3450	179.4	4604.9	31.491
4	0.3449	179.8	4608.8	31.494
5	0.3450	179.3	4604.3	31.492

Table 4.3: Best Parameter Results - Aligned vs. Staggered Configurations

Therefore, the final MATLAB results, which will be compared to CFD results, will be an average of each of the five generations for each parameter. After calculating this average, the cold plate design should maintain the surface temperature at $31.1°C$ at peak power dissipation. The convection coefficient expected for this cold plate is $4881.5\frac{W}{m^2K}$. This design results in a cold plate weighing $0.348kg$, with a pressure drop of $76.2Pa$.

Therefore, thirteen fins will be added to the 3D model in the longitudinal (downstream) direction and nine fins in the transverse (cross-stream) direction. These fins will have a pitch and diameter of $7mm$ and $3.7mm$, respectively. However, only half the fins will be added to the base plate, while the other half will be added to the cover

plate. This discrepancy occurs because the full-sized cold plate will have devices on both the top and bottom of the cold plate, requiring double-sided cooling. This double-sided cooling requires an equal number of fins on both surfaces; otherwise, one side will have superior or inferior cooling performance.

Fluid Flow Considerations: After populating the channel with pin fins, it is essential to consider the fluid flow as it travels throughout the system. This consideration resulted in chamfering the entrance and exit of the channels to remove any recirculation zones, which will inevitably occur in the corners. Also, any sharp edges in the channels were removed to have a smooth, unobstructed coolant flow.

One additional constraint provided by the machine shop is that all pins fins were $> \frac{3}{16}$" from the wall since this is a commonly used milling bit. Therefore several fins needed to be removed to accommodate this constraint. Two fins from each of the four sides of the channel were removed, resulting in sixteen total pin fins. This fin removal will slightly reduce the system's heat transfer but will make the machining process much quicker. It is possible to machine gaps smaller than $\frac{3}{16}$"; however, this requires a tool switch and longer machining times since less material is being removed per pass.

O-ring Calculations: One remaining critical design aspect of the cold plate is the o-ring seal. If the cold plate doesn't seal, the whole design is null and could have catastrophic consequences. For this reason, seal calculations were completed to ensure no leakage would occur. Face seal calculations were conducted since there would be no gap between sealing surfaces (i.e., the o-ring is contained within the groove). Based on online resources, tables exist with the optimal channel width, depth, and

corner radii for proper sealing [103]. In this case, since height is a serious concern for the cold plate, the smallest o-ring cross-section available was used (0.070"). Before implementation, several checks still need to be made to ensure proper o-ring fitment and sealing. One such check is the compression ratio. This compression ratio is calculated as:

$$Comp\ Ratio\ (CR) = \frac{C_{s,\,o-ring} - Gland\ Height}{C_{s,\,o-ring}}, \tag{4.17}$$

where C_s is the starting diameter of the o-ring (uncompressed) and gland height is the height of the groove where the o-ring will be inserted. Three calculations must be conducted to check the minimum, nominal, and maximum sealing values. These calculations will ensure that the seal will hold under the most extreme tolerances. The minimum compression ratio equation uses the minimum tolerance of the o-ring and the maximum tolerance of the channel. This design will have the smallest amount of compression applied if these two extremes are realized. Using Eq. 4.17, the calculated compression ratios are 14.9%, 20%, and 24.7% for the minimum, nominal, and maximum compression ratios, respectively. Standards suggest the compression ratio values should fall between 10-35%, which they do, so these calculations are acceptable.

Next, calculations for gland fill must be completed. These calculations consider concerns such as thermal expansion, swell, and manufacturing tolerances. To calculate the gland fill, the seal cross-sectional area must be found first. This cross-section is found using Eq. 4.18.

$$Seal_{cross-sectional\ area} = \Pi\Big(\frac{C_s}{2}\Big)^2, \tag{4.18}$$

$$Gland\ Fill\ (\%) = \frac{Seal_{cross-sectional\ area}}{Gland\ Depth * Groove\ Width}, \tag{4.19}$$

Eq. 4.19 is used to calculate the minimum, nominal and maximum gland fill percentages and resulted in values of 61.13%, 66.7%, and 72.56%, respectively. Since these all fall within the 50-85% range, the cold plate's groove dimensions will work. Therefore the final dimensions of the o-ring groove are 0.056", 0.103", 0.01" and 0.005" for the gland depth (D), gland width (W), gland corner radii R_1, and R_2, respectively. All these parameters were inputted in the 3D cold plate model in NX.

Fasteners: After the o-ring calculations, threaded M5 holes were added to the base plate. These holes will be used to fasten the cover plate to the base plate. M5 fasteners were used since enough force must be generated to adequately compress the o-ring and securely seal the two sections together. Eighteen fasteners were used to ensure that absolutely no leakage would occur, which was likely excessive. Additional structural analyses and calculations may be conducted to find the optimal amount of fasteners to prevent leakage but not increase the weight significantly. These considerations will be important for the final cold plate design; however, they are not critical for this prototyping stage. All fasteners were positioned outside the cooling loop (o-ring) to avoid leakage.

Weight Reduction: Lastly, weight reduction must be considered for the cold plate. This step consisted of rounding off any unnecessary corners and removing unnecessary material. Additionally, a large cutout was made solely for weight reduction to the underside of the cold plate. Any weight reductions in this design phase will directly correlate to increasing the converter's power density.

4.6.2 Cover Plate Design

After creating the base plate, the design was essentially mirrored to create the cover plate to ensure all dimensions matched up. All parts that needed to fit together were given a clearance of 0.012" ($0.3048mm$) around the perimeter to ensure a proper fit. Since only half of the total fins were added to the base plate, the remaining half were added to the cover plate. As mentioned earlier, this was done to ensure equal amounts of cooling to the top and bottom surfaces.

After this, fastener locations were mirrored from the base plate to the cover plate to ensure proper alignment between the two parts. The fastener heads were countersunk to avoid adding any additional height to the cold plate since this is a critical dimension. The countersunk fitment was set to "loose" to allow a marginal amount of space in case of manufacturing discrepancies.

4.6.3 3D Cold Plate Assembly and Bill of Materials

The finalized 3D model as described in sections 4.6.1 and 4.6.2 is shown here. All components are shown in an exploded 3D assembly view to provide a detailed overview with all critical components. A complete bill of material (BOM) is provided to clarify the components used. Manufacturers' part numbers are provided in case more information about a particular component is desired. The reference number in Table 4.4 is the corresponding number in the 3D view (Fig. 4.7).

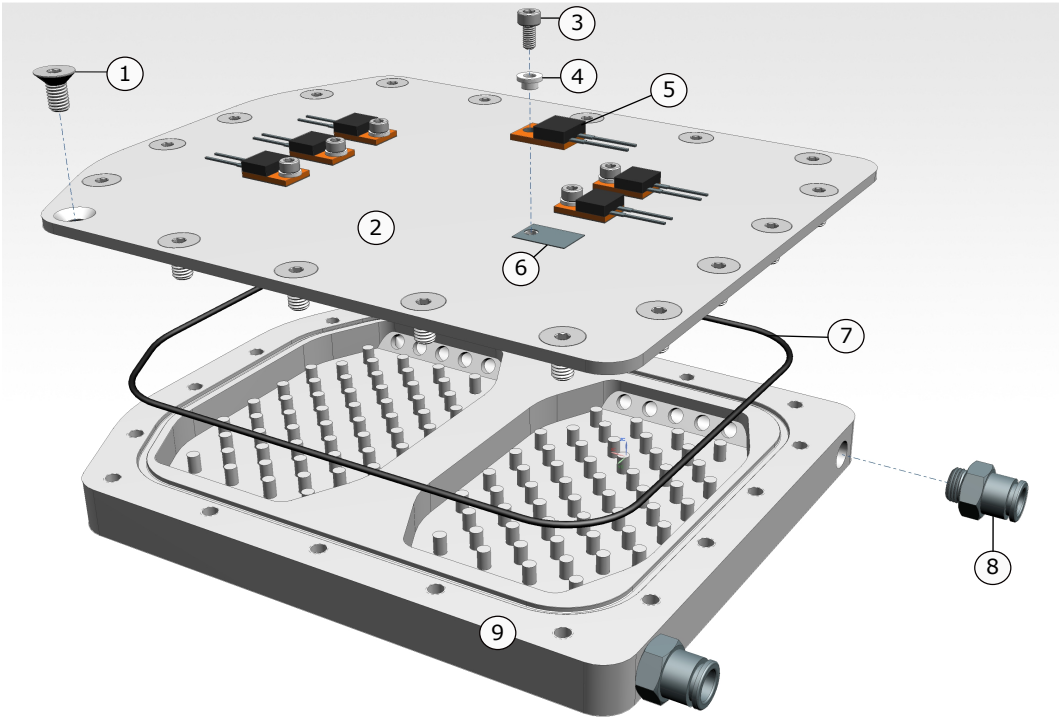

Figure 4.7: Proposed Full-Sized Prototype Cold Plate Assembly

Part Description	**Supplier**	**Part Number**	**Reference Number**	**Quantity**
M5x0.8 SS Fasteners	Mcmaster CARR	92125A208	1	18
Base Plate	N/A	N/A	2	1
M3x0.5 SS Fasteners	Mcmaster CARR	91292A111	3	6
Electrical Insulating Sleeve Washer	Mcmaster CARR	91145A319	4	6
Resistor 10 Ohm 50W TO220	Digi-Key	PF2205-10RF1	5	6
Thermal Pad	Digi-Key	SP600-90	6	6
1/16” O-ring Stock	Mcmaster CARR	3867T362	7	1
1/8” NPT Push-to-Connect Fitting	Mcmaster CARR	7397N29	8	2
Cover Plate	N/A	N/A	9	1

Table 4.4: 3D Model Bill Of Materials

Chapter 5

Design Verification

5.1 CFD Simulations - Convection Coefficient Verification

After completing all calculations and analytical work and proposing an initial design, this design requires simulation to verify all calculations and correlations. A commonly used simulation software is computational fluid dynamics (CFD). CFD is a way to mathematically model a particular system's flow, in this case, a cold plate. It uses numerical analysis and data structures to analyze the flow and resulting temperature and pressure distributions. It is critical to do this before the prototyping and testing stage to verify whether the analytical calculations are valid. All simulations were conducted using ANSYS software, including ANSYS Workbench, Design Modeler, ANSYS Mesher, CFX-Pre, and CFX-Post.

The first series of simulations aimed to compare the calculated convection coefficient between MATLAB and CFD simulations. If these coefficients match, this will verify that the Zukauskas correlation, which was used for the calculations (Eq. 4.5) is valid for the system.

To do this, the geometry was simplified to include only a single channel. For the entire cold plate prototype simulations, refer to section 5.2. Having only one channel mimics the "ideal flow" situation, which is how the MATLAB tool conducts its calculations. The MATLAB tool does not include the entrance and exit effects of the inlet and outlet since there is wide variability of potential combinations. Therefore this tool remains a general guide for design; refinements are added later. If simplified geometry were not used, the CFD results would be much worse than the MATLAB results since the MATLAB uses this "ideal flow," whereas the CFD would include the entrance/exit effects. The most critical parameter calculated within this section is the convection coefficient (heat transfer coefficient) since the temperature and pressure drop will change with the full-sized prototype (section 5.2). However, the temperature and pressure drop will still be monitored to ensure that the system operates as expected.

5.1.1 MATLAB Tool Proposed Design

Two different fin configurations were run in MATLAB to determine the optimal design. These include the staggered and aligned pin fin configurations. The input parameters remained constant throughout all MATLAB calculations. Additionally, all fluid and aluminum (cold plate material) properties remained constant. All input and output parameters are shown in Table 4.1 and Table 4.2. The suggested channel

design can be found in the output parameter section for both the aligned and staggered configurations. As discussed in that section, the aligned configuration will be used due to better performance metrics.

5.1.2 Geometry - Design Modeler

Once MATLAB has given the baseline pin fin design, it is essential to simulate this assembly in CFD to see if CFD and MATLAB results agree. If both software agree, the results should be trustworthy, and a prototype can be created based on these results. The simplified CFD geometry is constructed in Design Modeler, part of the ANSYS software, and is shown in Fig. 5.1. The geometry is very simple, consisting of an aluminum rectangular block. This aluminum block has a width, length, and height of $0.0800184m$, $0.1144m$, and $0.018m$, respectively. This aluminum block has a rectangular coolant channel with width, length, and height of $0.0700184m$, $0.1044m$, and $0.006m$, respectively. There is a 13x9 array of aligned pin fins within the aluminum block, as recommended by the MATLAB tool. Since this simulation looks at the "ideal flow," the inlet and outlet are identically sized cross-sections as the channel, thus negating any detrimental entrance or exit effects. This constant cross-section will also limit any induced internal turbulence that the geometry entrance or exit may create in the system.

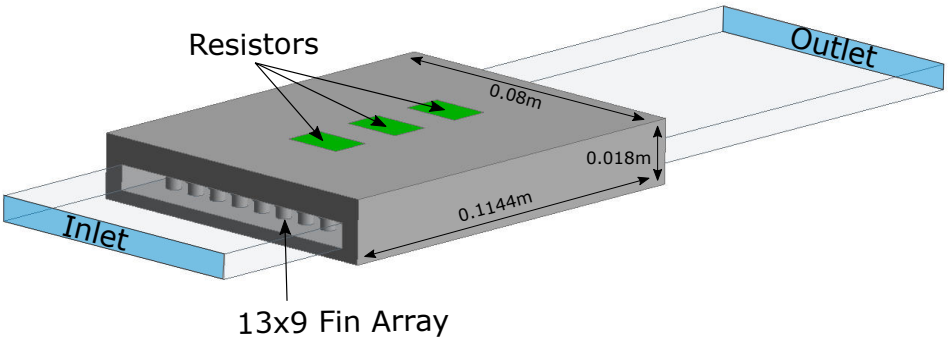

Figure 5.1: Simplified Geometry (Design Modeler)

In terms of power dissipation, as outlined in the MATLAB input parameters, three resistor locations will be centered over the channel, each dissipating $8.1W$ of power. This dissipation was added to the simulation as a heat flux, applied across the resistors' footprint (Fig. 5.1). The heat flux value was calculated using:

$$q = \frac{Q}{A_{resistor}}, \tag{5.1}$$

where Q and $A_{resistor}$ are the power dissipation and area of a single resistor. These values are $8.1W$ and $0.0001515m^2$, respectively. Subbing these into Eq. 5.1 results in a heat flux of $53{,}465.35\frac{W}{m^2}$ for each device. Next, the fluid inlet and outlet regions were extended to avoid recirculation issues during simulation.

5.1.3 Meshing

When meshing, care must be taken to create a fine enough mesh to capture the boundary layer effects while maintaining a reasonable node count. Too many elements/nodes will result in an unreasonable amount of computational time. Inflation layers were added at both sides of the fluid-solid interface to capture boundary layer

effects and maintain mesh quality. A tradeoff between the number of inflation layers and mesh quality must be obtained to have a solvable mesh and accurate results. To determine the size of the first inflation layer, ΔY was calculated.

Before calculating ΔY, the Reynolds number is calculated using Eq. 4.4 where ρ and μ are the density and dynamic viscosity of the coolant used, respectively. The velocity term in this situation is calculated using:

$$v = \frac{\dot{V}}{A_C}, \tag{5.2}$$

where $\dot{V}$ is the volumetric flow rate, and A_C is the cross-sectional area of the channel. After inputting all variables, the calculated Reynolds number is 1428.01, implying that the flow will be within the laminar region. Finally, ΔY can be calculated using:

$$\Delta Y = (Y+)L\sqrt{72}Re^{(-13/14)}, \tag{5.3}$$

where $Y+$ is a non-dimensional distance from the wall to the first mesh node, L is the diameter of the inlet, and Re is the calculated Reynolds number. The L value used in this case is the hydraulic diameter of the channel. This hydraulic diameter is calculated using:

$$D_h = \frac{4A_c}{P}, \tag{5.4}$$

where A_c is the cross-sectional area and P is the perimeter of the rectangular channel. After inputting the Reynolds number into Eq. 5.3, $Y+$ is set to its ideal value of 1, which may be changed later, depending on the resulting mesh quality. When all values were plugged into Eq. 5.3, the resulting value is $1.1034e^{-4}$m. This value was inputted in CFX as the first layer thickness in the CFD mesh and was adjusted afterward for

finer meshes in future iterations.

5.1.4 Mesh Independence Study

A grid/mesh independence study is conducted to ensure numerically accurate results. This study ensures that the results are independent of the mesh size. Increasing the number of nodes in the grid beyond this point of independence would not significantly affect the results. However, it would adversely affect the computational time and memory required to run a simulation.

Three different mesh sizes were used to investigate where mesh idependence is achieved for these simulations. For the coarse mesh, an element size of $0.001m$ was used for both the fluid and solid domains. Since inflation layers are critical at the boundary layer, six layers were added to both the solid and fluid sides of the solid-fluid interface. The first layer thickness of the inflation layer was set to $1.2e^{-4}m$ as calculated using Eq. 5.3, with a growth rate of 1.2. This growth rate dictates that the inflation layers increase in size by 20% each time. All quality metrics, node count, and element count can be found in Table 5.1. Both the medium and fine mesh specifications are also given in this table.

Mesh	**Nodes (N)**	**1/N**	**Elements**	**Orthogonal Quality**	**Element Quality**	**Aspect Ratio**	**Skewness**
Coarse	685,760	$1.5e^{-6}$	1,992,613	0.72	0.57	4.11	0.28
Medium	2,352,977	$4.2e^{-7}$	7,729,633	0.76	0.66	3.2	0.24
Fine	6,762,030	$1.5e^{-7}$	24,666,932	0.78	0.71	2.85	0.22

Table 5.1: Mesh Metrics

During each refinement process, the element size decreased, the first layer thickness decreased, and the number of inflation layers increased. Table 5.1 shows that the orthogonal quality, element quality, aspect ratio, and skewness improve at each successive mesh refinement. After conducting all simulations, three parameters were focused on for the mesh independence study: convection coefficient, surface temperature, and pressure drop.

All calculated surface temperatures, pressure drops, and convection coefficients for each respective mesh are shown in Table 5.2. To find the mesh independent solution, first, $\frac{1}{N}$ is calculated, where N is the number of nodes used. As this $\frac{1}{N}$ value approaches 0, the results converge to a mesh-independent solution. This mesh independent solution can be found by plotting the values in Excel and finding the y-intercept on the graph by plotting the trendline and using the trendline equation calculated by Excel. The Excel graph, trendline, and corresponding equation are shown in Fig. 5.2 for the convection coefficient. Similar plots for surface temperature and pressure drop were obtained but are not shown here. The calculated mesh independent results for surface temperature, pressure drop, and convection coefficient are $32.6°C$, $75.7Pa$, and $4757.8\frac{W}{m^2K}$, respectively.

Mesh	**Surface Temperature (°C)**	**Temp Error (%)**	**Pressure Drop (Pa)**	**Pressure Error (%)**	**Convection Coefficient ($\frac{W}{m^2K}$)**	**Convection Error (%)**
Coarse	32.5	0.4	113.1	49.32	5474.9	15.07
Medium	32.5	0.25	88.9	17.45	5205	9.40
Fine	32.6	0.06	77.8	2.79	4658.4	2.09
MATLAB	31.1	4.81	76.2	0.67	4881.5	2.60
Mesh Independent	**32.6**		**75.7**		**4757.8**	

Table 5.2: Mesh Independence Study Results

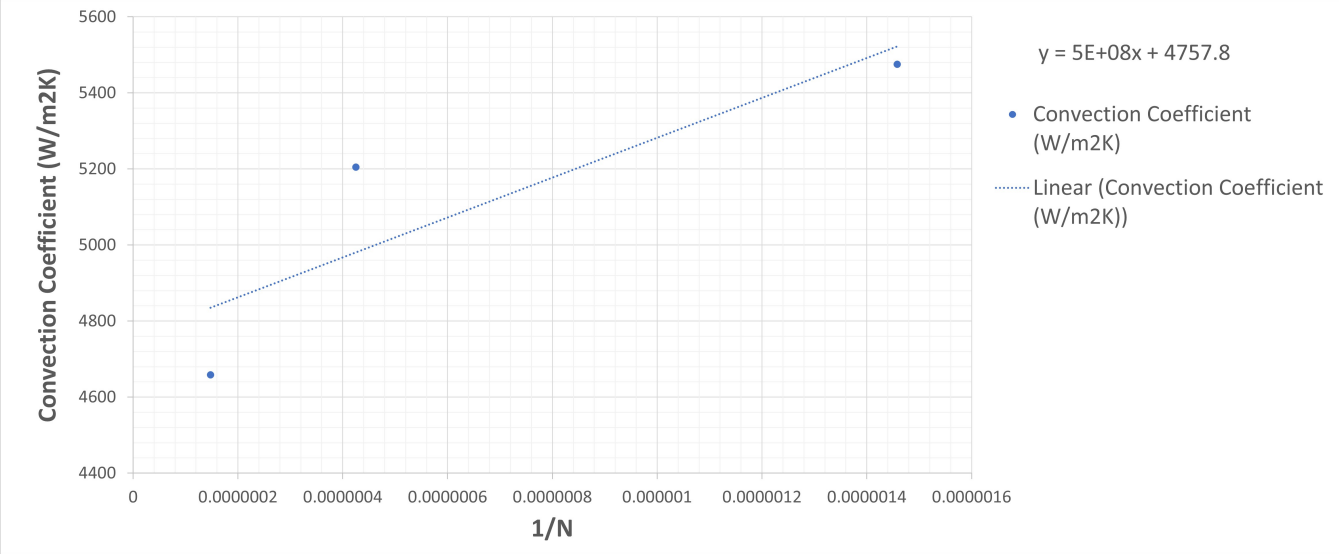

Figure 5.2: Mesh Independence - Convection Coefficient

Lastly, the percentage error of each parameter was calculatrror for the pressure drop and convection coefficient parameters only drop below 5% when using the fine mesh. The error compares each mesh's results with the mesh-independent solution. The error must be less than 5% for results to be considered mesh independent. In these simulations, the temperature remains consistently within this 5% range. However, the error for the pressure drop and convection coefficient parameters only drop below 5% when using the fine mesh. Therefore, the fine mesh results will be considered the mesh independent solution and used for further analysis.

Matlab vs. CFD Comparison: Next, it is essential to compare the CFD mesh independent results to the MATLAB results, obtained in Table 4.3. Values of $31.1°C$, $76.2Pa$, and $4881.5\frac{W}{m^2K}$ were calculated in MATLAB for the surface temperature, pressure drop, and convection coefficient, respectively. When comparing these, percentage errors of 4.81%, 0.67%, and 2.6% were obtained. Since all these values are

within the 5% acceptable margin of error, these results were determined to be trustworthy.

It is crucial to realize that these CFD and MATLAB values will not match the experimental results since these calculations use "ideal geometry" and an "ideal flow" situation. Instead, these results aim to verify that the MATLAB calculations match the CFD results. The surface temperature, pressure drop, and convection coefficient using the complete cold plate geometry will represent the experimental results more accurately. These results can be found in section 5.2.

5.1.5 Boundary Conditions Setup and Inputs

When setting up the project in CFX-PRE, the turbulence model was set to laminar flow because the calculated analytical Reynolds number was 1428.01, which would make the fluid fall within the laminar region. Any value below a Reynolds number of 2300 should exhibit laminar flow according to the literature. The next step within the CFX setup was to apply the inlet velocity. This velocity was calculated using Eq. 5.2 to be $0.119\frac{m}{s}$. This inlet velocity was applied to the entire inlet cross-sectional face. Outlet pressure of 0 pascals was applied to the corresponding outlet face. The thermal conductivity used was $167\frac{W}{mK}$ for all simulations. This thermal conductivity will be significant within the simulations to determine how the heat will travel through the aluminum cold plate.

Lastly, a time step calculation must be conducted for the simulations. This time step value is important with the overall system convergence. Often the automatic setting is not optimal for solving. If set manually, this value is dictated by the

equation:

$$\Delta T = f\tau_{res}, \tag{5.5}$$

where f is some fraction of τ_{res}, and is typically within the range of $0.1 < f < 2.0$. τ_{res} is found using:

$$\tau_{res} = \frac{L_c}{V_c}, \tag{5.6}$$

where L_c is the characteristic length and V_c is the characteristic speed of the flow. The hydraulic diameter was used as the characteristic length, and the inlet velocity was used as the characteristic speed. An initial f value of 0.25 is set. This value can be adjusted manually depending on the rate of convergence. If this f value is set too small, the system may take forever to converge or may never converge. However, if this value is too large, the residuals may oscillate uncontrollably and never converge or result in inaccurate results. Several test cases are conducted to see if the time step influences the results significantly.

5.1.6 Sources of Error

Numerical Error The first significant source of error in CFD simulations is the numerical error. This type of error can be subcategorized into three sections. The first of these subcategories is the iterative convergence error. This type of error comes from how the solver iterates through each data point to determine the solution. This iterative process plays a critical role in obtaining accurate results. Due to the iterative nature of the CFD software, an actual residual value of zero is impossible. For this reason, the residual values of $1e^{-6}$ were set within CFX Pre for the continuity equations. These residuals measure the local imbalance of the conserved variable

within a specific control volume. For CFD simulations, the closer the residual is to 0, the better since this will result in the most accurate results possible.

The second important component of numerical error is the truncation (round-off error). This type of error exists since the solver and computer are limited by the number of decimal places they can store. These rounding errors are not significant at first but can become compounded through every solver iteration to influence the final results significantly. To investigate the impact of this error, both single and double precision numerics are used for simulations. Double precision will undoubtedly take longer to simulate, but it is vital to explore if it significantly alters the results. After simulating both cases, the changes between the two were insignificant (below 0.25% change), implying that double-precision numerics are not required for accurate results.

The most critical and often most significant source of numerical error is called the discretization error. This error results from the governing equations being solved within a discrete domain with a finite number of grid points. As the number of grid points increases and the spacing between the grid points decreases (i.e., the mesh is refined), the resultant discretization error will converge to zero. However, adding grid points will also increase the computation time and memory required for simulation. This type of error is mitigated through the mesh independence study conducted in section 5.1.4.

Modeling Error The second significant source of error is the modeling error. This type of error comes from uncertainties regarding the physical model used in the simulations. These include situations where the thermal designer may not have all the parameters, thus forcing them to make certain assumptions. Any assumptions made will inherently introduce uncertainty into the system. Typically, the model will be

simplified to reduce computation costs when running simulations. Doing so will introduce some variability into the design, affecting the results. It is essential not to remove any critical components which will significantly affect the fluid/ heat flow of the system. This simplified model is straightforward (on purpose), aiming to mitigate or eliminate all modeling errors by using an "ideal flow" situation. Therefore, this is not a significant concern for this model.

Systematic Error The third and final major source of error within CFD simulations is the systematic error. This type of error stems from the differences between the simulations and experimental data. Obviously, the simulations have limitations that reduce the accuracy of the results. There are several potential sources for this type of error, depending on the setup. Possible sources include assuming material uniformity throughout the aluminum workpiece and assuming pressure and velocity conditions are constant at the boundaries. A constant velocity and pressure condition were used in all simulations run at the cold plate's inlet and outlet. Also, the properties of the 50-50 water-ethylene glycol (WEG) coolant were assumed to be constant throughout the simulations might may affect the results.

5.1.7 Solution Residuals

Since it has been determined that the fine mesh is required to obtain a mesh-independent solution, the results from the fine mesh will be explored further. The first thing to look at is the residual monitors. These values need to be at or below the $1e^{-6}$ criteria that were specified during setup, which is the case. All mass and momentum residual values converge between $1e^{-7}$ and $1e^{-8}$. The closer these values are to zero, the better, so these results look promising. Next, there are the H-energy

and T-Energy equations. These are both below the $1e^{-5}$ mark, which is a sufficient level of accuracy. Some oscillations are observed in the H-energy equation, which can often be attributed to the timestep. For this reason, several simulations were run using various timesteps.

5.1.8 Parameter Monitors

Although the primary objective of these simulations is to verify the convection coefficient, some additional parameters are helpful to monitor and ensure that the system is behaving as expected. These parameters include the systems' pressure drop, the mass flow rate of the fluid, and the surface temperature of the aluminum. To ensure that our system has reached a steady state, we want to see whether these variables have stopped oscillating between iterations. If these monitored parameter values flat line, the results have usually converged to a meaningful result. If these parameters continue to oscillate, this could indicate that the system has not reached a steady state, and there could be an issue with the setup.

Steady-state is achieved for pressure drop at a value of $77.8Pa$. Next, the maximum surface temperature monitor was investigated to see whether it had reached a steady-state. Similarly, this reached a steady state at a value of $32.6°C$. Lastly, the cold plates' mass flow rate entering and leaving the system is monitored. This parameter can give us insight into whether the system is performing as expected since the mass flow in must equal the mass flow out based on the law of conservation of mass. This constraint is upheld, and the mass flow in and mass flow out remains constant at a value of $0.053042\frac{kg}{s}$.

5.1.9 Flow Distribution

After ensuring that CFD has converged to a meaningful solution, it becomes essential to analyze the results. The first thing to look at is the fluid velocity vectors to see whether the fluid enters, exits, and flows through the system as expected. In this case, since the inlet velocity is applied evenly across the inlet face, there should be an even distribution of flow entering the system. Indeed this is the case, with the fluid flowing between the fins in streamlined flow (Fig. 5.3). If a staggered configuration were used, the flow in the pin fin region would be much more turbulent. In this case, there are some recirculation effects near the exit of the fluid domain. This effect is most likely due to the low flow rate of the fluid. Additionally, some fluid may be re-entering the system in the form of backflow. However, since this only occurs after the pin fin array, it will not influence the results significantly. In an earlier step, the outlet was extended to mitigate this recirculation's effect on the cooling occurring within the pin fin array.

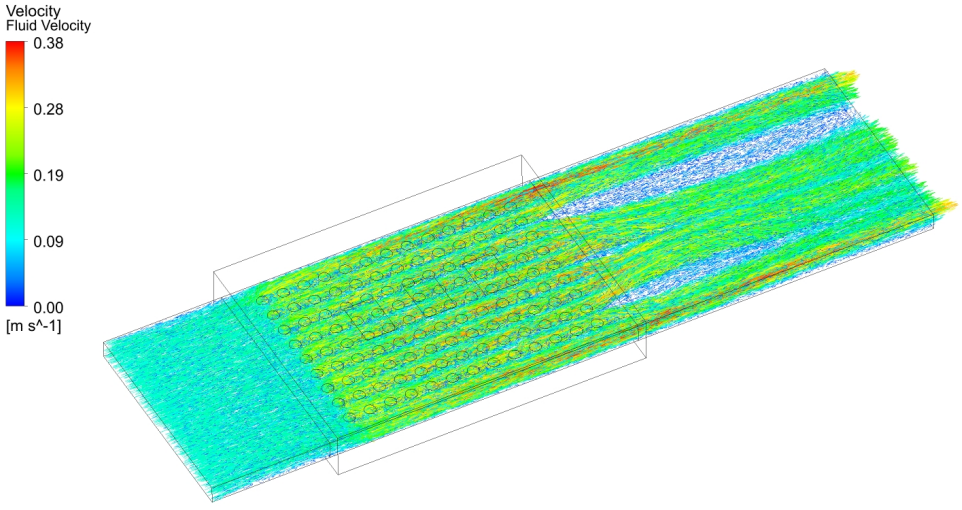

Figure 5.3: Velocity Vectors

5.1.10 Temperature Contours

Next, the temperature contours for the cold plate's solid and fluid domains will be investigated. As expected, local hotspots are observed under where the devices would sit (Fig. 5.4). There are several significant trends to understand from the figure regarding the three resistors. First, the first resistor in the series would have the lowest temperature since the coolant is the coldest at that point. Next, the last resistor will be the second coolest since the coolant will have picked up heat from the two proceeding devices. Lastly, the middle device will be the hottest since the coolant picks up heat from the first device, and lateral conduction occurs between the two surrounding resistors due to their close proximity. All these trends are verified in Fig. 5.4.

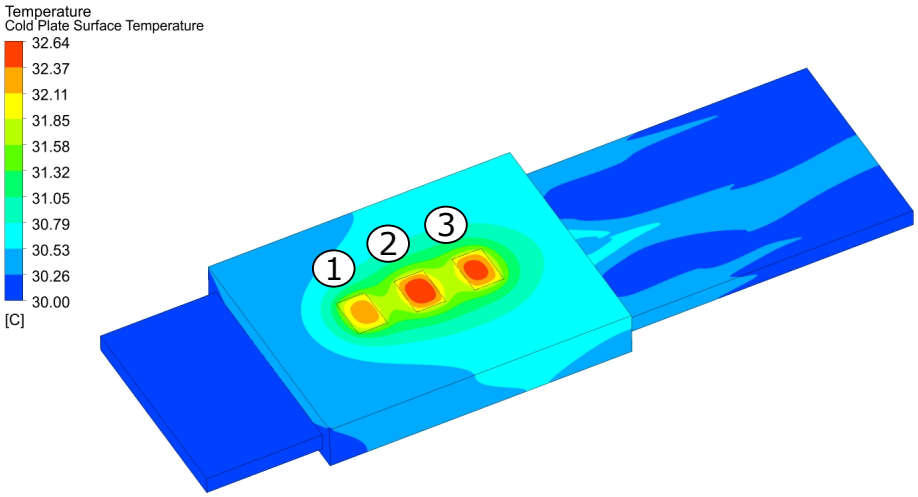

Figure 5.4: Temperature Contours

To investigate this heat transfer in more detail, a cross-section is taken at the middle of the cold plate. Both the solid and fluid domains are shown in this cross-section. Underneath the resistor locations, the highest temperatures (shown in red)

are experienced. The blue sections are the coolant channels that have the lowest temperature. Suppose we zoom into the coolant channel regions. In that case, we see a temperature gradient around each aluminum pin fin as the heat is transferred from the fin into the coolant (Fig. 5.5). This figure clearly illustrates the convective heat transfer occurring at the fins. This gradient would become even more pronounced if we increased the heat dissipation from the devices. In this scenario, the coolant would pick up more heat from the devices and dissipate it into the coolant.

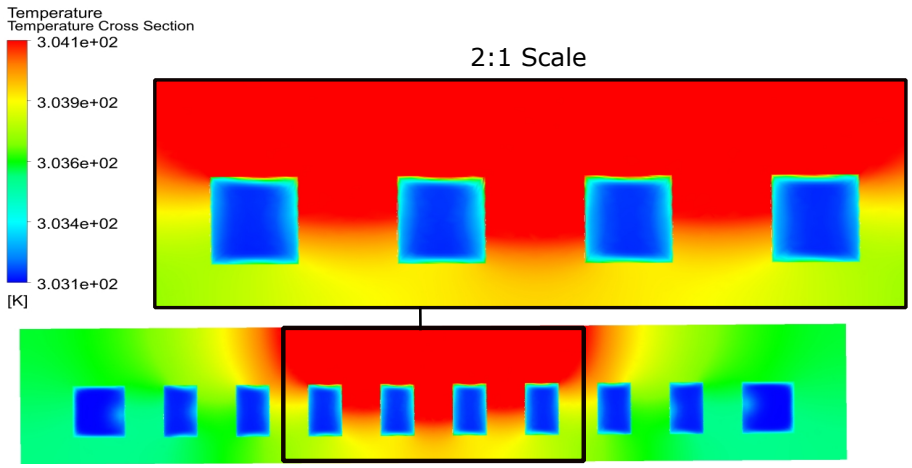

Figure 5.5: Cross-Sectional Temperature Gradients

5.1.11 Pressure Distribution and Pressure Drop

Lastly, the system's static pressure and pressure drop are analyzed to ensure the system is behaving as expected. Fig. 5.6 shows a linear gradient of pressure drop occurring as the fluid moves between the inlet and the outlet. This linear behavior is expected since there is no inlet or outlet to create local areas of high pressure or pressure losses due to sudden constriction or expansion. For this reason, much higher static pressure and pressure drop are expected for the full cold plate prototype

simulations. The system's pressure drop is calculated using the area-averaged pressure at the inlet minus the area-averaged outlet pressure. This definition results in a total pressure drop of $77.8Pa$ for the fine mesh simulation. This pressure drop will determine how much pumping power will be required to push coolant throughout the system.

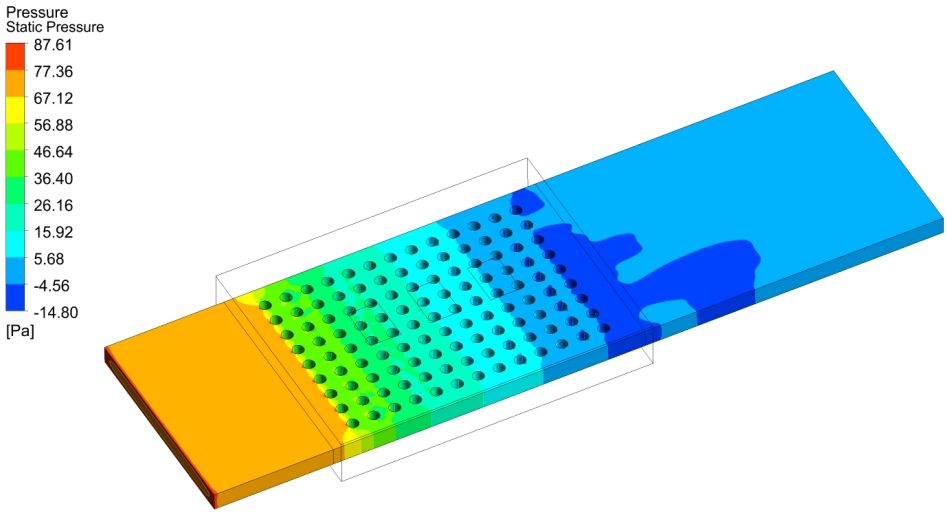

Figure 5.6: Static Pressure Contours

5.1.12 Convection Coefficient Calculation

When comparing the convection coefficient (heat transfer coefficient) values obtained from MATLAB to CFD, the values from the fine mesh are used since this was determined to be the mesh-independent solution. The focus here is on the heat convection and its several definitions. For one, it can be calculated through empirical correlations as completed in MATLAB. Contrarily, it can be calculated in CFD using:

$$h = \frac{q}{\Delta T A_{conv}}, \tag{5.7}$$

where q is the total power dissipation from all resistors, and ΔT is the change in temperature between the solid interface and the coolant via convection. This ΔT is found by measuring the temperature at the convective heat transfer area (A_{conv}) and subtracting the reference temperature. The reference temperature of the coolant is $30°C$, which is the inlet coolant temperature.

Lastly, A_{conv} is the convective area (or heat transfer surface area) through which the heat transfer will occur. The heat transfer surface area is commonly referred to as the "wetted surface area," which helps us visualize which area to use. Any aluminum area in contact with the coolant will transfer heat from the aluminum into the coolant. However, since heat dissipating devices are only on the top surface, the channel's two sides and bottom faces will not be added to the heat transfer surface area.

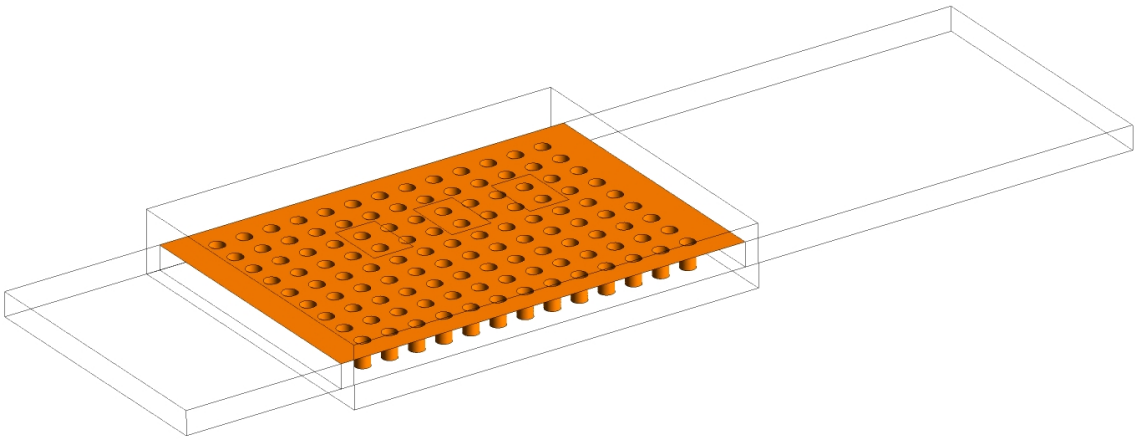

Figure 5.7: Heat Transfer Area

Therefore, the heat transfer surface area used in the simulations is the pin fin surface area plus the top face of the coolant channel. This surface area is depicted in orange in Fig. 5.7. The majority of the heat will be transferred through these

surfaces into the coolant. A certain amount of heat will also be dissipated into the ambient air, but this is negligible for the simplified simulations.

When all values are inputted into Eq. 5.7 the resultant convection coefficient value is $4658.4\frac{W}{m^2K}$. This value coincides very well with the calculated coefficient from MATLAB, which is $4881.5\frac{W}{m^2K}$. When calculating the percentage error, the following simple equation is used:

$$\%\, Error = \frac{Calculated\, Result - Simulated\, Result}{Simulated\, Result}, \tag{5.8}$$

where the calculated result is the value retrieved analytically from MATLAB, and the simulated result is the value obtained from the CFD via post-processing. After plugging in the values obtained, the percent error obtained is 4.79%. This percentage error means that the MATLAB analytical results are 4.79% higher than the CFD results, or in other words, the MATLAB results overpredict the cold plate performance by 4.79%. This discrepancy is reasonable since MATLAB is purely analytical calculations and does not consider real-life flow conditions. The CFD results should typically be more accurate since they account for real-life flow conditions. In this case, the analytical and CFD results match very well, so it is assumed that the convection coefficient calculated in MATLAB is valid. Therefore, all correlations used to calculate this coefficient in MATLAB are verified and are used for the validation case.

5.2 CFD Simulations - Full Cold Plate Design

The final CFD simulations use the entire cold plate prototype design as outlined in section 4.6.3. The primary objective of these simulations is to get a more accurate view of the actual expected convection coefficient value, temperature distributions, and pressure drop within the cold plate. These values will be compared to the experimental results to validate agreement between CFD simulations, MATLAB, and the experiments. This three-pronged approach to heat transfer problems is the most comprehensive way to have feasible, reliable results. This approach allows us to compare analytical (best case scenario) with simulated and real-life results (worst case scenario).

5.2.1 Geometry - Design Modeler

The full-sized prototype cold plate geometry was dictated by MATLAB and is explained in more detail in section 4.6. As an overview, the full plate design incorporates two fluid channels which run under the six resistors being cooled (three per channel). Each channel has an internal array of 13 fins in the downstream and 9 fins in the cross-stream direction. The cold plate was designed in two sections for ease of manufacturing; the base plate and cover plate.

Firstly, the cold plate geometry was simplified in Design Modeler. Any geometry that was not critical to the flow distribution was removed to improve meshing. These modifications included removing exterior fillets on the cold plate aimed at weight reduction and aesthetic appeal. These changes won't negatively affect the systems' coolant flow or heat transfer but will improve mesh quality. The top cover and base plate were also merged into one piece. This merging would eliminate any small gaps

where leakage or meshing errors may arise.

5.2.2 Inlet/Outlet Optimization

The next step is to optimize the two channels' inlet/outlet diameters. These diameters refer to the 5x holes per channel for both the inlet and outlet, for a total of 20 holes (Fig. 5.8). From literature, it is understood that if all diameters for the channel inlets/outlets are the same, more flow will travel through the first channel. This effect occurs because the fluid will take the path of least resistance to find its way from the main inlet to the outlet. The diameter of all channel inlet and outlet holes was set to $5mm$ initially. After simulating this baseline scenario, as expected, the results showed that the first channel received $0.0038\frac{kg}{s}$ (0.23LPM) more flow than the second channel.

This difference in flow rates is problematic because the resistors over the first channel will be cooled better than those over the second channel. In the production DC-DC converter, this effect will result in unequal current sharing between modules, negatively impacting the converter's performance. An optimization was run to determine the diameter of holes that would allow equal flow distribution between channels to mitigate this issue.

To accomplish this optimization, the inlet hole diameters were set as a modifiable input parameter within Design Modeler. A separate parameter was created for channel one and channel two so that these parameters could be modified independently. The outlets for both channels were set to mirror their respective inlet diameters. Therefore, the 5x inlet diameters and corresponding 5x outlet diameters of channel one would be set to one value (D_1), whereas channel two would have a

different diameter for its 10x inlet/outlet (D_2). Channel two's hole diameter must also be larger than channel one's to push more fluid into this channel. To illustrate these dimensions, reference Fig. 5.8.

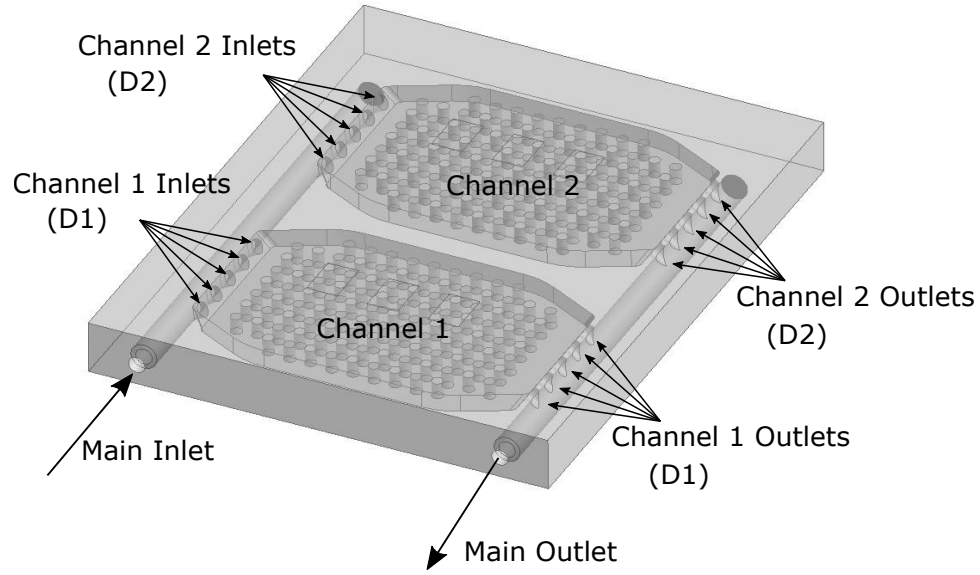

Figure 5.8: Channel Inlets/Outlets Used in Optimization

Next, to determine how much mass flow rate each channel was receiving, a face was created at the midpoint of each channel using the 'slice' feature. The mass flow rate was calculated at each face within CFD Post. Lastly, the mass flow rate variance was calculated by dividing the total mass flow rate by two (two channels) and subtracting each channel's calculated mass flow rate. This mass flow rate variance parameter was then set as an output parameter for the optimization.

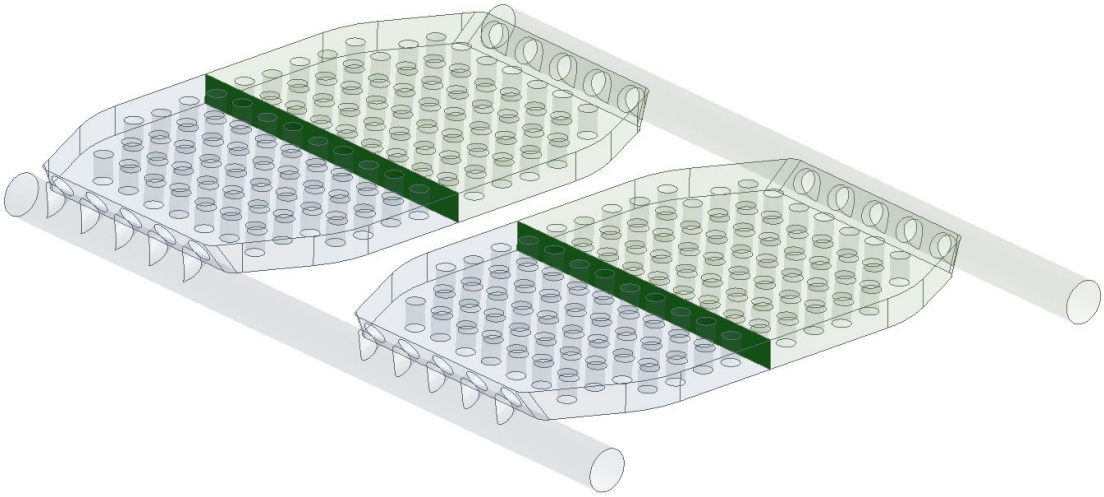

Figure 5.9: Midpoint Channel Face for Optimization (Fluid Domain)

With everything set, a 'Direct Optimization' block was used, which is built into ANSYS workbench. The simulation objectives used were that the mass flow rate variance in channels one and two equals 0 (or as close to it as possible). Then the input parameters (D_1 and D_2) received their upper and lower bounds. For this case, the geometry dictated that the diameter must be less than $5.5mm$ and larger than $4.5mm$. Any smaller than $4.5mm$ would cause unnecessary flow restriction and increase the pressure drop, which was not desired. Therefore, a single constraint was added, ensuring that the inlet and outlet diameters in the 2nd channel (D_2) were larger than the 1st channel (D_1).

Once setting all inputs and constraints, the optimization was run. Based on the results, a theoretical hole diameter of $4.9609mm$ and $5.2266mm$ was selected for the five inlet and outlet holes for channels one and two, respectively. This combination resulted in a mass flow rate variance of $7.2494e^{-6}\frac{kg}{s}$ and $7.242e^{-6}\frac{kg}{s}$ for channels one and two, respectively. For confirmation of equally distributed flow, the mass flow rate of channel one and channel two are identical until the 5th decimal place.

Finally, what does this value mean for our cold plate design? The last step is to find the drill bit size as close to this theoretically optimal hole diameter as possible. After checking drill charts, a #9 and #5 drill bit will be used for channels one and two, respectively. These drill bits result in an actual diameter of $4.9784mm$ for channel one and $5.2197mm$ for channel two. After inputting these values and rerunning the simulations, there is a much better flow distribution meaning that this optimization functioned as desired. All pre-optimized and post-optimized values of flow rate and velocity are shown in Table 5.3. Also shown is the variance (difference) between the flow rates and velocity before and after optimization. These results show that the mass flow rate difference could be reduced by $0.0027\frac{kg}{s}$ (0.16LPM) after optimization. This results in a 71% decrease in variance for both the mass flow rate and the velocity which shows significant improvements. This difference could be reduced further if more iterations were run; however, this was sufficient accuracy for this thesis.

		Pre - Optimization	**Post - Optimization**	**Units**	**Improvement**
Channel 1	Diameter (D1)	5	4.9609	mm	/
	Mass Flow Rate	0.0705	0.0692	$(\frac{kg}{s})$	/
	Velocity	0.137	0.135	$(\frac{m}{s})$	/
Channel 2	Diameter (D2)	5	5.2266	mm	/
	Mass Flow Rate	0.0667	0.0681	$(\frac{kg}{s})$	/
	Velocity	0.130	0.133	$(\frac{m}{s})$	/
	Mass Flow Rate Variance	0.0038	0.0011	$(\frac{kg}{s})$	**$0.0027\frac{kg}{s}$ (71.1%)**
	Velocity Variance	0.007	0.002	$(\frac{m}{s})$	**$0.005\frac{m}{s}$ (71.4%)**

Table 5.3: Channel Inlet/Outlet Optimization Results

5.2.3 Meshing

Meshing is conducted similarly to the smaller simplified model 5.1.3, except that four levels of mesh refinements are performed. The element size, first layer thickness, and inflation layers are modified to get four different meshes (coarse, medium, fine, and finer). For the coarse mesh, the first inflation layer thickness was again set to $1.2e^{-4}m$ to start. The element size was set to $0.0013m$, and six inflation layers were used. Like before, the element size and first inflation layer thickness will decrease, and the number of inflation layers will increase at each mesh refinement level. All quality metrics, node count, and element counts can be found in Table 5.4.

Mesh	**Nodes (N)**	**1/N**	**Elements**	**Orthogonal Quality**	**Element Quality**	**Aspect Ratio**	**Skewness**
Coarse	1,646,345	$6.1e^{-7}$	7,221,750	0.74	0.68	3.83	0.26
Medium	3,430,866	$2.9e^{-7}$	15,451,041	0.76	0.72	3.36	0.24
Fine	6,486,434	$1.5e^{-7}$	29,919,357	0.77	0.72	3.19	0.23
Finer	9,341,585	$1.1e^{-7}$	39,252,528	0.78	0.75	2.82	0.22

Table 5.4: Mesh Metrics

5.2.4 Mesh Independence Study

Similarly to section 5.1.4, the mesh independent solution is found using Excel, using $27.78W$ as the device power dissipation level for all simulations. The Excel graph, trendline, and corresponding equation are shown in Fig. 5.10 for the convection coefficient. Similar plots for the surface temperature and pressure drop were obtained but are not shown here. The calculated independent mesh results for surface temperature, pressure drop, and convection coefficient are $34.4°C$, $103{,}243Pa$, and $1973.3\frac{W}{m^2K}$, respectively.

Lastly, the percentage error of each parameter was again calculated for each mesh. The error must be less than 5% for results to be considered mesh independent. In these simulations, the surface temperature and pressure drop error remain below this 5% range for all meshes. However, the convection coefficient parameter error only drops below 5% when using the fine or finer meshes. Since the results are insignificantly different between the fine and finer meshes, the fine mesh will be used to reduce computational time. This lack of change dictates that the mesh size (above the fine mesh) does not significantly impact the system results. A 'finest' mesh was also conducted with a higher level of mesh refinement, but the resultant parameter values changed insignificantly. Therefore, the fine mesh results will be considered the mesh independent solution and will be compared to the experimental results in a later section.

Mesh	**Surface Temperature ($^\circ$C)**	**Temp Error (%)**	**Pressure Drop (Pa)**	**Pressure Error (%)**	**Convection Coefficient ($\frac{W}{m^2K}$)**	**Convection Error (%)**
Coarse	35.0	1.83	96,955	6.09	1678.3	14.95
Medium	34.8	1.05	98,170	4.91	1755.5	11.04
Fine	34.5	0.41	102,529	0.69	1925.1	2.44
Finer	34.5	0.32	102,235	0.98	1930.2	2.18
Mesh Independent	**34.4**		**103,243**		**1973.3**	

Table 5.5: Mesh Independence Study Results

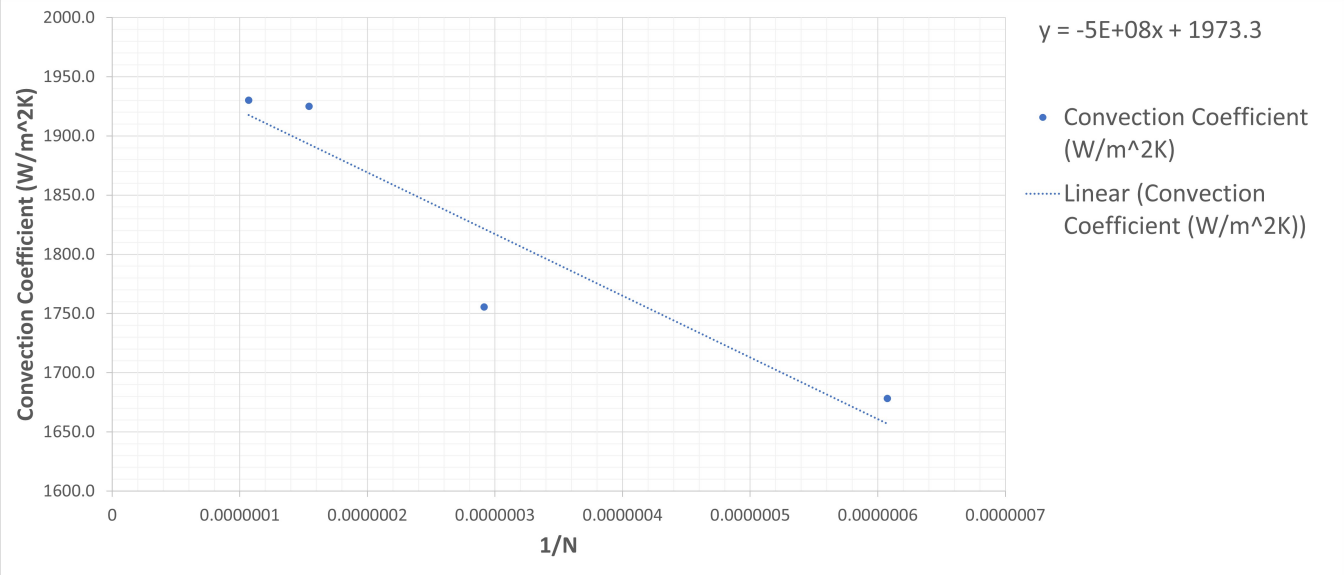

Figure 5.10: Mesh Independence - Convection Coefficient for Full Cold Plate

5.2.5 Boundary Conditions and Inputs

Several boundary conditions have been updated between the simplified geometry and the full-sized prototype cold plate simulations. These modifications were made to replicate the experimental setup to compare and analyze results between the CFD and experiments.

The first modified boundary condition is the heat flux. Since there are now six devices, six heat fluxes are applied to the top face of the aluminum cold plate. The heat flux will be modified for different power levels for the five various power dissipation levels ($8.1W$, $17.78W$, $27.78W$, $37.38W$, $48.4W$).

Next, a low convection coefficient was added into the simulation to mimic the heat loss into the ambient air around the exterior of the cold plate. Therefore five faces (top, four sides) had a heat flux of $5\frac{W}{m^2K}$ applied to them. The bottom face did not experience convection to the ambient since it was resting on the work desk during

the experiments. This heat flux was not applied in the simplified simulation since the convection coefficient was much higher, and this $5\frac{W}{m^2K}$ would have a negligible effect on the results. However, the convection coefficient is much lower for the full cold plate due to entrance/exit effects, and this heat flux may slightly affect the results. Also, since the area available for convective heat transfer into the air is much more significant for the full plate, this convection is vital to consider. After testing this theory, the results still changed insignificantly, reducing the maximum temperatures at the heat fluxes by about 0.1-0.2$°C$.

The next modified boundary condition was the inlet velocity. Ideally, a flow rate of 12 liters/minute (LPM) would be used; however, the setup at McMaster maxed out at 9.54 LPM (2.52 gallons/min). Therefore, this flow rate was used to calculate the inlet velocity, resulting in $8.097\frac{m}{s}$.

Due to the increased velocity and the circular channel inlets/outlets being added into the simulation, the fluid will experience areas of turbulence within the flow channels. Therefore a turbulent flow model was used instead of the laminar one used in section 5.1.5. The shear stress transport model was selected due to its broad applicability.

Next, the inlet coolant temperature had to be modified from the original 30$°C$. Again, limitations within the lab setup prevented this temperature from being used. Instead, the temperatures recorded from the experimental results were used as the simulation inputs in Table 6.3.

Lastly, a sand grain roughness of $2.1916e^{-5}\mu m$ was added to the solid-fluid interface inside the cold plate due to the sandblasting done in the manufacturing stage. This roughness may alter the results slightly, and this boundary condition was added

since high accuracy was required. For a full breakdown of how this value was obtained, see section 6.1.1.

5.2.6 Sources of Error

Numerical Error The same considerations were made as in section 5.1.6 concerning the numerical error. Residual values were set to $1e^{-6}$ within CFX PRE to ensure the accuracy of the results. Double precision numerics were also compared to single precision, with insignificant changes occurring between the two cases. Again, the discretization error is mitigated through the mesh independence study, which can be found in section 5.5.

Modelling Error Modeling error within the simulations is mitigated by keeping the cold plate simulation geometry as close to the experimental geometry as possible. The only difference in the simulation was that the two parts were merged to avoid small elements or gaps during meshing, which could cause issues. Besides that, all channel and fin dimensions remained constant between the simplified simulations, prototype simulations, and the manufactured cold plate.

Systematic Error As mentioned in section 5.1.6, one possible source of systematic error includes assuming material uniformity throughout the aluminum workpiece. This effect was mitigated by running several simulations with varying properties to study the impact of these properties on the solution. The results were not significantly impacted when changing the material properties. Another source of numerical error is assuming pressure and velocity conditions are constant at the boundaries. A constant/uniform velocity and pressure condition were used in all simulations run at the

cold plate's inlet and outlet. Also, the properties of the 50-50 water-ethylene glycol (WEG) coolant were assumed to be constant throughout the simulations might may affect the results. However, the coolant temperature did not increase dramatically; therefore, this should not affect the results significantly.

5.2.7 Solution Residuals

The residual monitors were investigated using the fine mesh case (since this was determined to be the mesh independent solution), starting with the mass and momentum equations. All these equation residuals reached a convergence of $1e^{-6}$ or lower, which is a sufficient level of convergence for simulations, but more checks are required before the results can be verified. The next check investigates the convergence levels of the H-energy and T-energy equations. These equations have reached $<1e^{-4}$ and $1e^{-6}$, respectively, which are well within the acceptable range for convergence. There are no severe oscillations in any of the residuals, which could indicate poor convergence or an inaccurate solution.

Next, the maximum residuals were investigated, which correlates to specific nodes often with worse mesh quality than those surrounding them, creating a higher residual value. Most of these max residual locations fall within the channels at the solid-fluid interface at the pin fins. This location makes sense because it is often hard to mesh rounded surfaces, especially small pin fin geometry. This small geometry often results in worse quality mesh at the pin fin interface. Additional inflation layers were added at this solid-fluid interface to mitigate this issue as much as possible.

5.2.8 Parameter Monitors

Besides heat transfer, several additional parameters were monitored to investigate whether the system behaved appropriately. These parameters include a pressure drop, surface temperature, and mass flow monitor as in section 5.1.8. All parameters were investigated to ensure that they reached a steady state. For the case using $27.78W$ of power dissipation for each resistor, steady-state was achieved at values of $34.5°C$, $102{,}529Pa$, and $0.2011\frac{kg}{s}$ for surface temperature, pressure drop, and mass flow rate, respectively.

5.2.9 Flow Distribution

After simulating the entire cold plate flow, the following results are obtained in CFX Post. First, the velocity vectors are analyzed. These vectors in Fig. 5.11 illustrate how the flow is traveling throughout the cold plate. The scale was locally modified (0-1$\frac{m}{s}$) to show the velocity vectors within the channels better. Areas in red can have a much higher velocity than $1\frac{m}{s}$. This scale emphasizes that the inlet and outlet areas have high velocity and turbulence, while the flow will be primarily laminar within the channels. This effect is due to the small diameter of the inlet and outlet channels.

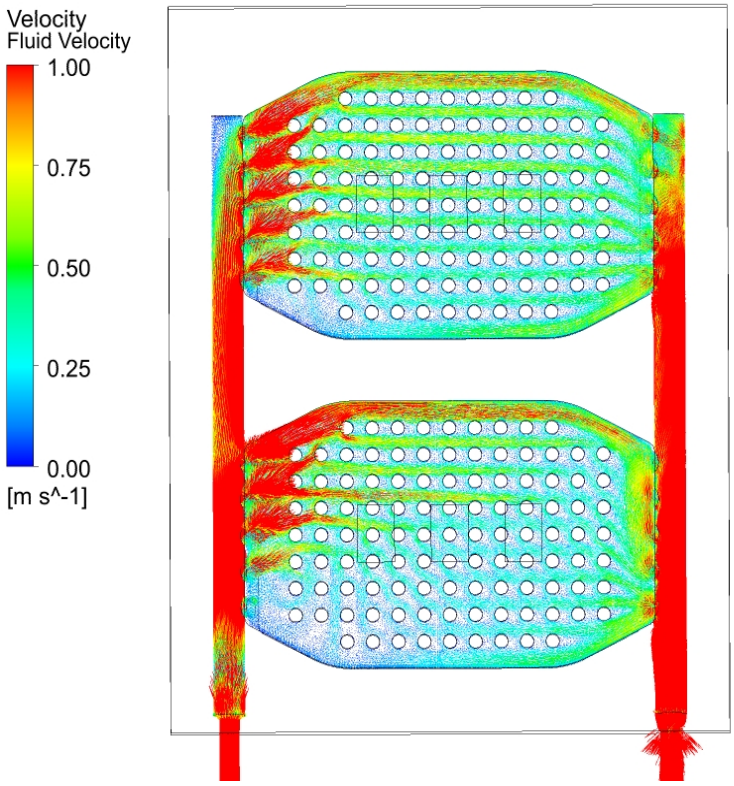

Figure 5.11: Full Cold Plate - Fluid Velocity

Unfortunately, the flow distribution is less uniformly distributed as expected based on earlier simulations. Two main factors caused this discrepancy. Firstly, the flow is streamlined at the inlet as it speeds up to fit through the small inlet fitting. This fitting was not considered in the initial optimization since parts were not finalized at that point. Unfortunately, this reduction in cross-section area increases the coolant velocity forcing the liquid to partially bypass the 1st and 2nd (of 5) channel inlets of the first channel, which is not desired. Secondly, the flow rate was lower than what it was designed for (9.54 vs. 12 LPM); therefore, the flow behavior is not equal between the two channels as expected. The calculated mass flow rates for channels one and two are $0.10388\frac{kg}{s}$ and $0.119528\frac{kg}{s}$, respectively. However, when looking at

the surface temperature change (Table 6.2), the temperature differences between the resistors over channels 1 and 2 are negligible. These tiny temperature changes will not negatively impact the converter's performance.

5.2.10 Temperature Contours

Temperature contours for the full cold plate are shown in Fig. 5.12. Here it shows that the leftmost device of both channels is the coolest since the coolant is at its lowest temperature at this point. After the coolant passes the first device, it picks up heat before reaching the second and third devices. For this reason, the third device in the series is the second hottest. Therefore, the middle device is the hottest since it also picks up heat from the two surrounding devices via conduction through the aluminum.

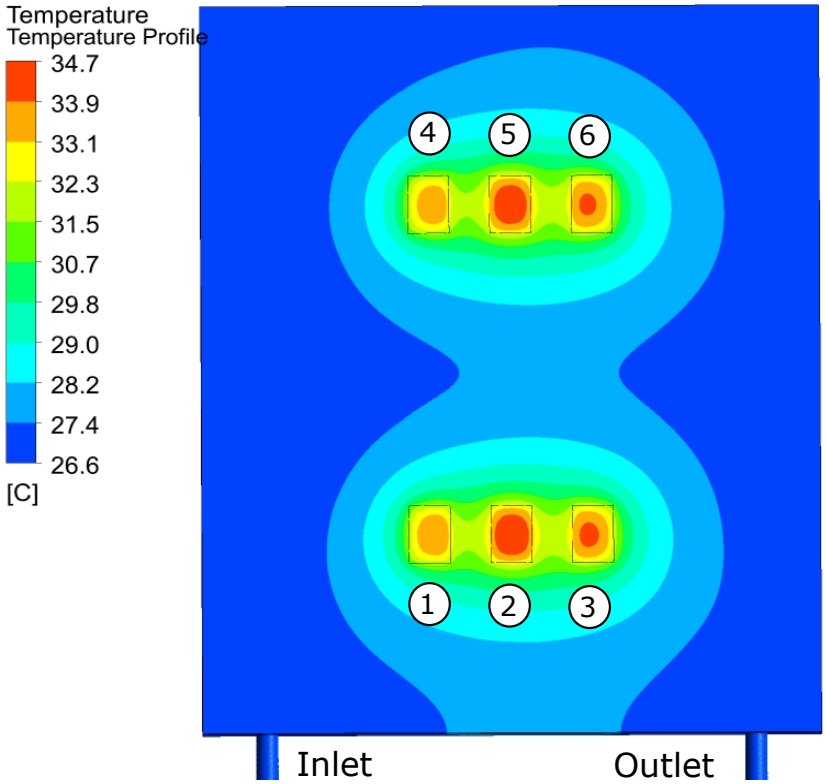

Figure 5.12: Full Cold Plate - Temperature Contours

Next, a cross-section of the cold plate at the middle resistor was investigated to look at the heat transfer into the fluid. The temperature scale was modified from 299.5 to 302K (26.35 to 28.85°C) to illustrate the heat transfer occurring between the aluminum cold plate and the coolant. There are several essential things to note in Fig. 5.13. Firstly, only half the fins are red since half of the fins are attached to the top plate; the other half are connected to the baseplate and would not assist with heat transfer since there are no devices on the bottom side. Secondly, when looking closely at Fig. 5.13, there is a gradient of temperatures (colors) occurring at the interface between the solid (red) and fluid (dark blue) as the heat leaves the aluminum and is transferred into the coolant. This gradient clearly illustrates the

convective heat transfer occurring at this solid-fluid interface.

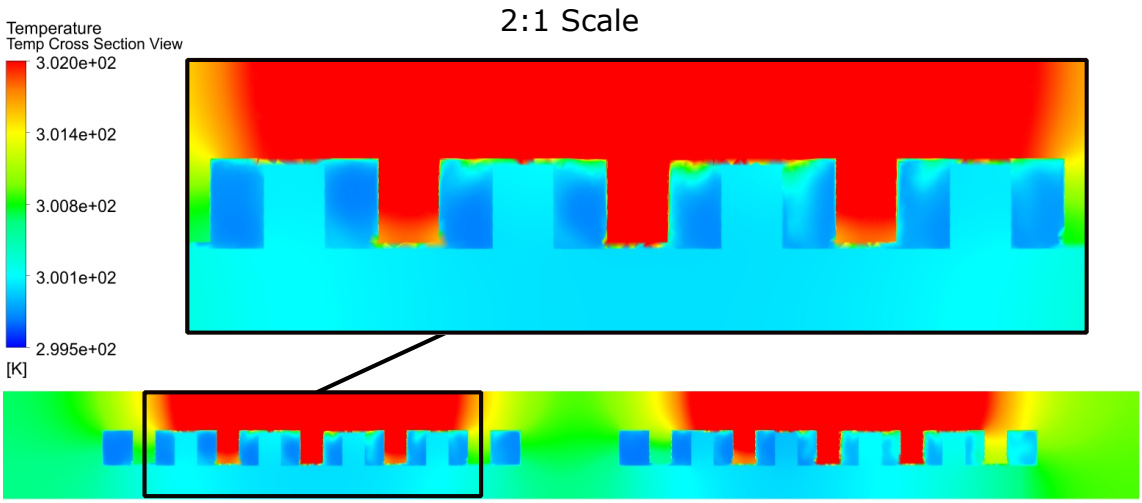

Figure 5.13: Full Cold Plate - Temperature Close Up

5.2.11 Pressure Distribution and Pressure Drop

Next, the systems' static pressure distribution is analyzed and calculated. Firstly the static pressure contours are shown in Fig. 5.14. Pressure drop is critical since it will push the fluid from high to low-pressure areas throughout the cold plate. Here the maximum pressure is 102,529Pa, with the minimum pressure being 0Pa (set in CFX-PRE as the outlet condition). This results in a total pressure drop of 102,529Pa, which will later be compared to the experimental results (section 6.2.3).

In Fig. 5.14 the scale was modified from 80,000 – 95,000Pa to more accurately investigate what is happening within the fluid channels. Here, pressure recovery is evident; as the fluid velocity decreases, the static pressure increases along the length of the main inlet. This phenomenon is understandable, considering that pressure and velocity are inversely related.

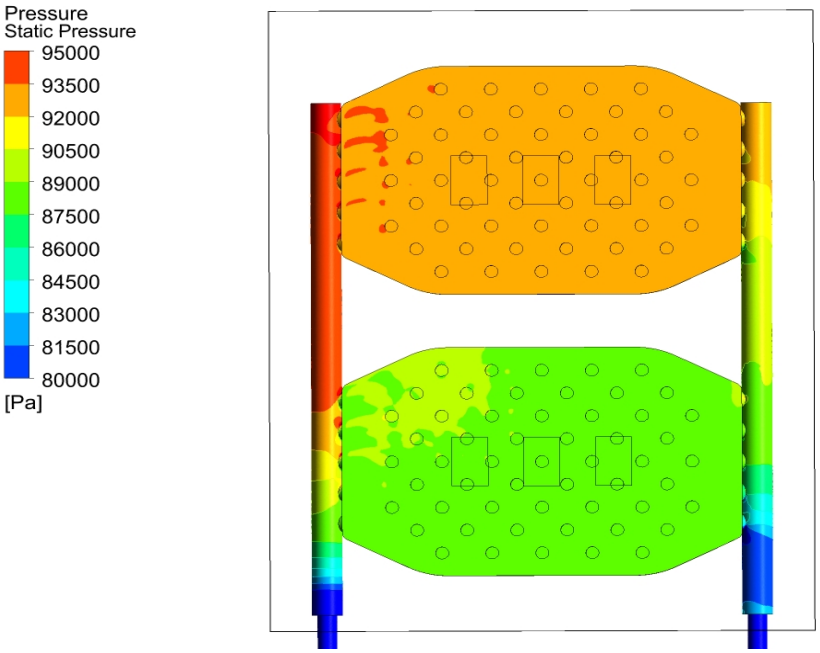

Figure 5.14: Full Cold Plate – Static Pressure

5.2.12 Convection Coefficient Calculation

The heat transfer coefficient is calculated using the same method as in section 5.1.12. Five different coefficients are calculated, one for each power dissipation level. These levels are 8.1, 17.78, 27.78, 37.38, and 48.4 watts. Each power dissipation will be multiplied by the number of devices (six) to give the q in Eq. 5.7. The ΔT will be obtained from the simulations using T_{wall} - T_{Inlet}, where T_{wall} is the area-averaged temperature obtained at the top surface of the coolant channel. This T_{wall} (Fig. 5.15) was used to calculate the convection coefficient, which will later be compared with the experimental results in Table 6.10. T_{wall} is essentially the temperature at the base of the fins since calculating the exact temperature at the fin walls would be very difficult for the experimental setup. The A_{conv} used is shown in Fig. 5.16 which includes the

top face of the channels and half of the pin fin faces (since only half of the fins are attached to the cover plate and would be involved in the heat transfer). Using Eq. 5.7, the resultant convection coefficient is calculated for each power dissipation level and is shown in Table 5.6.

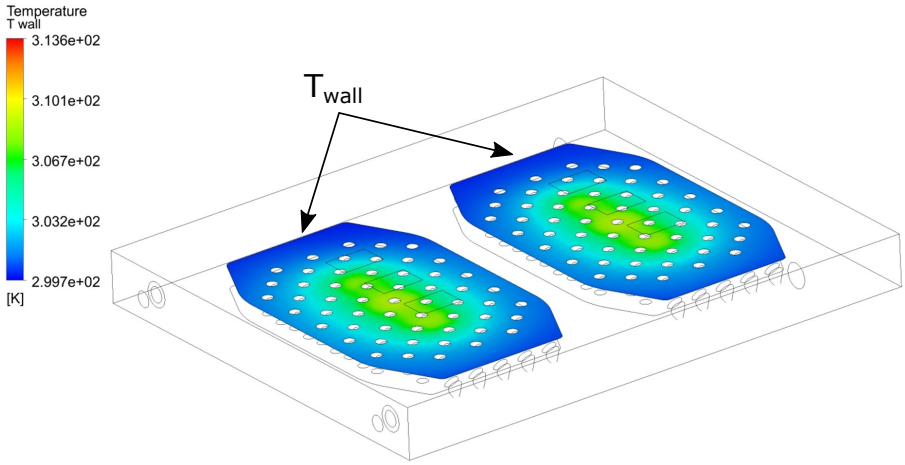

Figure 5.15: Temperature Measurement Location (T_{wall})

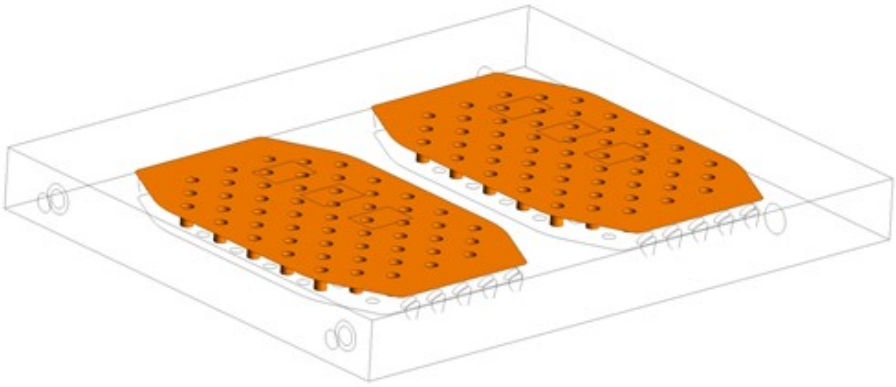

Figure 5.16: Heat Transfer Area (A_{conv})

Total Power Dissipation (W)	**Wall Temperature (°C)**	**Inlet Temperature (°C)**	**ΔT (°C)**	**Convective Area (m^2)**	**Convection Coefficient ($\frac{W}{m^2K}$)**
48.6	27.8	26.3	1.5	0.01985	1705.7
106.7	29.1	26.4	2.7	0.01985	1985.3
166.7	30.6	26.4	4.2	0.01985	1997.8
224.3	33.3	26.5	6.8	0.01985	1677.5
290.4	34.1	26.6	7.5	0.01985	1935.9

Table 5.6: Convection Coefficients

These convection coefficient values will only be directly compared to the experimental results in Table 6.10 to investigate whether the results agree. It is important to note that the convection coefficient values in Table 5.6 are much smaller than the original values of $4658.4\frac{W}{m^2K}$ (CFD) and $4881.5\frac{W}{m^2K}$ (MATLAB) in Table 5.2. These results cannot be directly compared for a variety of reasons. First, this is due to the introduction of the inlet and outlet, which introduces pressure losses and negatively impacts flow uniformity. Secondly, the fluid must turn 90 degrees after entering the inlet to travel through the channels, after which it must turn another 90 degrees to exit the cold plate. Each turn reduces the fluid velocity and increases the system's pressure drop. Lastly, the simplified simulations consider all fins and use a fin height of $6mm$. In contrast, the full cold plate simulations consider only half the fins with a fin height of $5.5mm$ for manufacturing reasons.

Chapter 6

Prototyping And Testing

6.1 Prototype Manufacturing

6.1.1 Manufacturing Process

Manufacturing The cold plate prototype material was sourced from 6061 aluminum. This type of aluminum exhibits good mechanical strength, thermal conductivity, and weldability. Typical thermal conductivity for 6061-T6 aluminum at $25°C$ is $167\frac{W}{mK}$ therefore, this value will be used for all simulations [104]. The cold plate was designed to be manufactured in two pieces. A single-piece design was also explored since this could minimize weight; however, 3D printing would drastically increase costs and lead time, which is not desirable. Also, the cold plate was designed to be built in-house at McMaster University. Manufacturing the cold plate at McMaster would radically reduce the costs and provide a valuable manufacturing experience. However, this slightly limits some design aspects since McMaster does not have all the

sophisticated equipment some state-of-the-art manufacturing shops have. For example, many shops may have a four or five-axis CNC machine, allowing greater design flexibility and more complicated designs. Therefore, instead of creating a chamfered face like the proposed prototype design has (Fig. 4.7), the 5x inlet/outlet holes were drilled at an angle relative to the vertical face of the channels (Fig. 6.1a). Unfortunately, this may have introduced some variability in the precise hole locations and angles, but it is sufficient for this prototype.

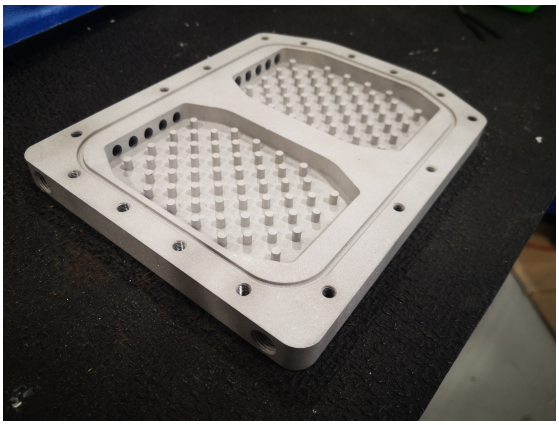

(a) Base Plate

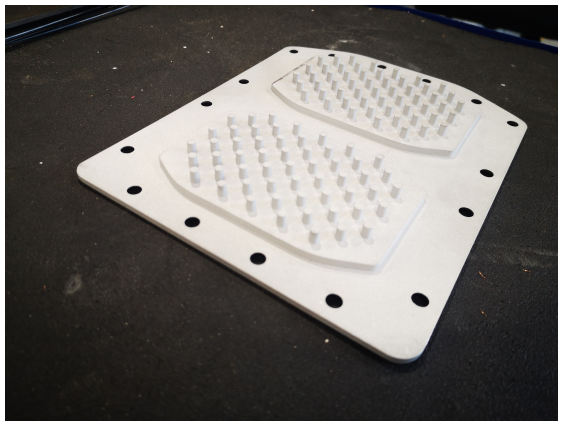

(b) Cover Plate

Figure 6.1: Manufactured Cold Plate Prototype

Another limitation was that the machine shop did not have a specialty long drill bit that could drill the main inlet/outlet its entire depth in one pass. Therefore, to remedy this, a matching hole was drilled from the front and back of the cold plate. Both the front and rear ends were tapped to a $\frac{1}{8}$" NPT thread size. The back of the cold plate received a $\frac{1}{8}$" NPT plug to eliminate leakage, whereas the front received the $\frac{1}{8}$" NPT fitting for the coolant inlet.

To ensure adequate cold plate sealing, the pin fins were given a height of $5.5mm$ within the $6mm$ internal channel. This $0.5mm$ discrepancy ensured that even if

manufacturing tolerances were out, the cold plate would still be able to close and seal properly without any fins causing interference.

The cold plate was successfully manufactured out of an aluminum block, primarily using a manual mill. Operations include milling the channel sections and drilling all inlet/outlet holes. Then drilling and tapping the $M5$ threaded fastener locations was completed. Then the top plate was manufactured using similar techniques. $M5$ countersunk clearance holes were added to the cover plate so that the fastener heads would not protrude from the surface. Lastly, $M3$ tapped holes were added to the top of the cold plate to secure the resistors to the cold plate. Both manufactured pieces are shown in Fig. 6.1.

Finishing - Sandblasting After the cold plate was manufactured, it was sandblasted to give it an aesthetic surface finish. Besides just the aesthetic appeal, sandblasting would add roughness to the interior channel and pin fins, theoretically improving the system's heat transfer. Before testing began, any sand residue was removed since residue could cause clogging or fouling. This manufactured prototype will be used in all experimental testing moving forward.

To calculate an appropriate surface roughness to use for the CFD simulations, a profilometer was used to measure the average surface roughness (R_a) of the sandblasting finish. First, the profilometer was calibrated using the high precision measuring block designed for tool calibration. After this, eight samples were taken to ensure an accurate approximation of the surface roughness. All values are found in Table 6.1.

Measurement	Supplier	Units
1	4.049	μm
2	4.013	μm
3	3.102	μm
4	3.640	μm
5	3.601	μm
6	3.734	μm
7	3.923	μm
8	3.516	μm

Table 6.1: Surface Roughness (R_a) Measurements

Next, the highest and lowest measurement values (#1&3) were removed since they seemed to be outliers. The six remaining surface roughness values were averaged to give $3.738\mu m$. This value was converted to sand grain roughness using the method outlined in the paper by Adams et al. [105]. This conversion is done using:

$$\epsilon = 5.863 R_a, \tag{6.1}$$

After conversion, the resultant sand grain roughness value (ϵ) is $2.1916e^{-5}m$, which will be used in the full cold plate CFD simulations (section 5.2.5).

6.1.2 Cold Plate Assembly Process

6.1.2.1 Mechanical Assembly

First off, the o-ring installation process was vital to the successful operation of the cold plate. First, the o-ring stock was purchased from McMaster CARR. The issue with this product is that the o-ring had to be cut to length since it was not a standard size. The problem with cutting the o-ring is that where the two ends meet will result

in a leak potential. A gasket maker is used at the connection point to eliminate this leakage. As an extra precaution, the gasket maker was also installed along the entire inside perimeter of the o-ring channel (Fig. 6.2). This gasket will provide a second layer of defense along with the o-ring to prevent any possible leakage. The type of gasket maker used is Permatex – anaerobic 518 gasket maker. This gasket maker is explicitly designed for aluminum, steel, and iron parts. It can fill gaps up to 0.015", which is perfect for this application. The gasket maker application is shown in Fig. 6.2 where the red is the gasket, which only hardens in the presence of metal (or the absence of oxygen).

Figure 6.2: O-ring/Gasket Installation Process

After applying the gasket maker, the base plate and top cover were joined together using $M5$ fasteners to secure the assembly. The fasteners were torqued to 5 lb-ft (pound-foot), the standard tightening torque for $M5$ coarse fasteners (grade 8.8).

This torque was delivered using a digital torque wrench and a crisscross torquing pattern. This crisscross pattern ensures that all fasteners are equally torqued and that the cold plate is correctly secured together.

The next issue within the mechanical assembly was an unexpected one. The sandblasting, which was beneficial within the channels for added surface roughness, proved to be an issue when securing the resistors to the cover plate. The added surface roughness from sandblasting will introduce air pockets that impede heat transfer from the resistors into the cold plate. Additionally, securing thermocouples to the surface may give inaccurate readings due to poor surface connection. Therefore, the top face of the cover plate was sanded up to 3000 grit sandpaper.

Once the face has been sanded, the resistors which mimic the MOSFETs were installed. Under the resistors are thermal pads designed for the same TO-220 package. The thermal resistivity for the thermal pads is $0.35\frac{^\circ C}{W}$ which was inputted into the MATLAB code during the design phase. The resistors and the thermal pads were attached to the cover plate surface via $M3$ fasteners. Before this occurs, a nylon electrically insulating sleeve washer is inserted into the fastener location. This washer will ensure electrical isolation between the resistor and the cold plate; otherwise, the fastener would cause a short.

The next critical assembly component was the surface thermocouple setup. The thermocouples used for this project are probe bead type K thermocouples. As per the manufacturer, these thermocouples are capable of reading temperature from -40 to $260^\circ C$ with an accuracy of +-$1.1^\circ C$. This error will be reduced to $0.2^\circ C$ through the thermocouple calibration process outlined in section 6.2.8.

These six thermocouples need to capture the surface temperature at each resistor

accurately; however, having the thermocouple directly underneath the devices is not viable for this setup. If underneath, these thermocouples would prevent the resistors from making good contact with the aluminum surface. This effect would influence the heat transfer negatively, which is not desirable. Instead, the thermocouples were placed on the top surface of the aluminum, as close to the resistors as possible. This location will allow the most accurate reading without disrupting the system's heat transfer. Before attaching the thermocouples, a small dab of the thermal joint compound from Wakefield was used. This compound fills micro air gaps between the thermocouple tip and the aluminum surface. This material has an excellent thermal resistance of $0.05\frac{^\circ C}{W}$ for a 0.001-inch film. After applying the compound, the thermocouple is attached and secured using Kapton tape. Additionally, a transparent plastic plate is clamped to the cold plate to apply downward force to the thermocouples to ensure strong contact and accurate readings. These thermocouples will be hooked into the 8-channel Data Acquisition Module (DAQ) to convert the voltage to a temperature reading. The finished cold plate experimental setup with the resistors, electrical components, and thermocouples is shown in Fig. 6.3.

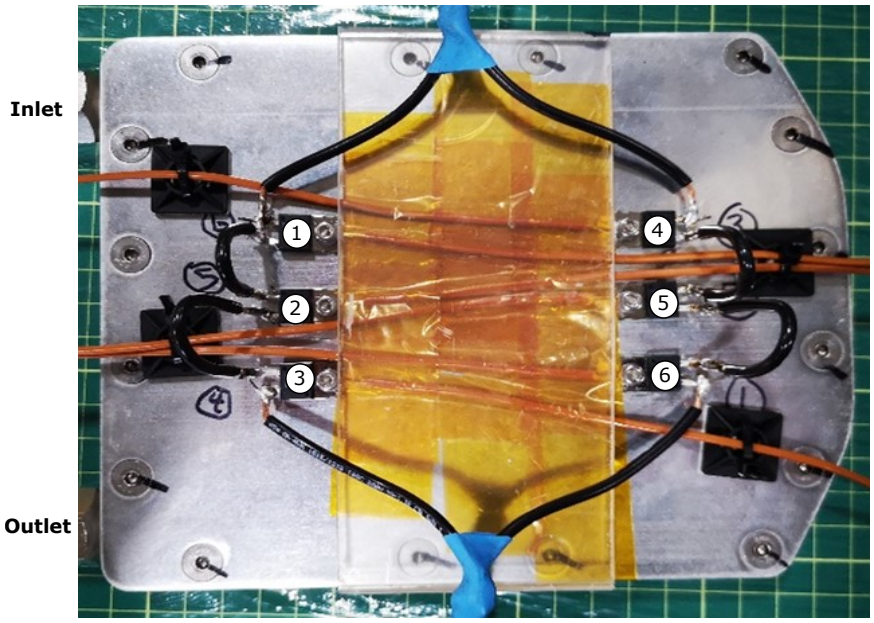

Figure 6.3: Thermocouple Placement

6.1.2.2 Electrical Assembly

A schematic of the electrical circuit is shown in Fig. 6.4a. This diagram shows how the six resistors are split up into two parallel paths with three devices in series. The voltage applied will be distributed equally into each of the resistors. Therefore, the same voltage will be applied across each resistor, resulting in equal power dissipation for all devices. This schematic was implemented in the test setup as shown in Fig. 6.4b. Not pictured here is that the two leads on the left and the two on the right will be connected together, and then a single voltage will be applied to all devices. All connections were soldered, ensuring a robust and durable connection. Minimal wire lengths were used to reduce power and heat losses along the wires.

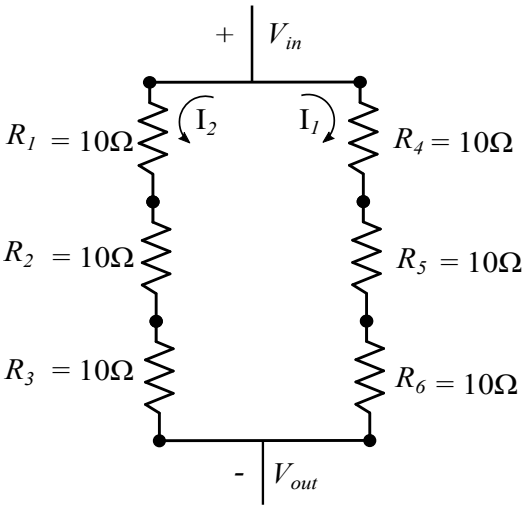

(a) Schematic

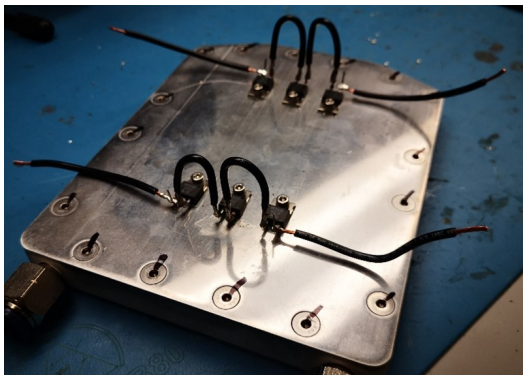

(b) Experimental Setup

Figure 6.4: Electrical Assembly - Schematic and Experiemental Test Setup

6.2 Experimental Testing Procedure

6.2.1 Theoretical Setup

Before any testing took place, both a theoretical and real-life test setup was created. The complete theoretical setup is shown in Fig. 6.5 with all required components. These components include big-ticket items like the pump, control valve, and mass flowmeter to monitor the flow and ensure the proper amount of coolant enters the cold plate.

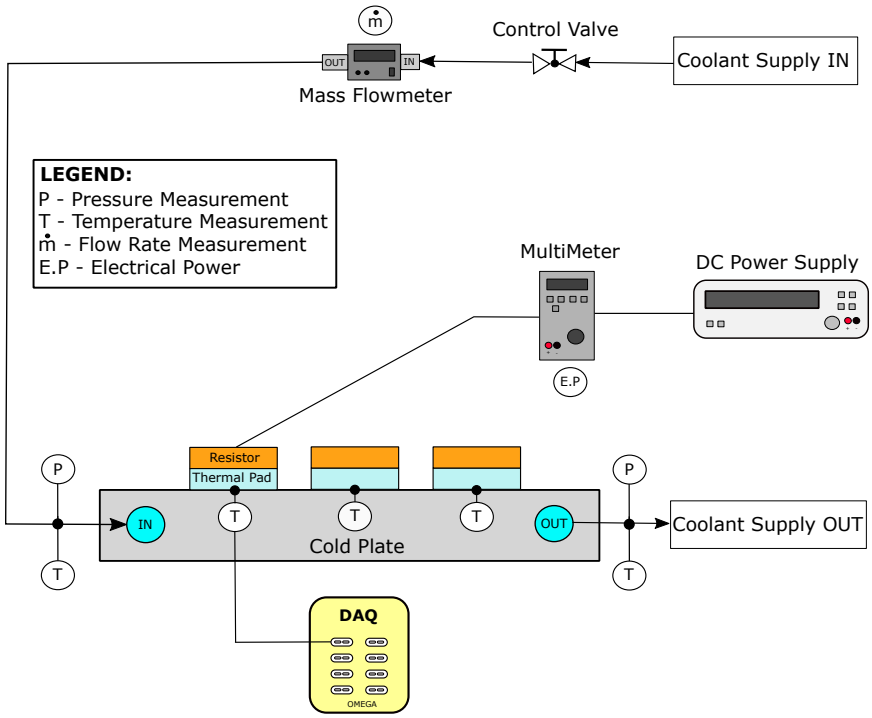

Figure 6.5: Experimental Setup - Theoretical

After going through the flowmeter, the fluid enters and exits the cold plate. An inline pressure gauge monitors the coolant pressure before entry and upon exit. These pressure gauges will allow the pressure drop to be calculated by subtracting the exit pressure from the entry pressure. Besides measuring pressure, the coolant temperature will also be measured before entering and after leaving the cold plate. Instead of a temperature gauge, an inline thermocouple is used for more precise temperature readings. A thermocouple is necessary since the temperature increase will be very minimal due to the low power dissipation of the devices. These thermocouples will be hooked into the Data Acquisition Module (DAQ), which will translate the voltage into a temperature value. The DAQ being used is an 8-channel USB thermocouple DAQ, capable of reading eight temperatures simultaneously. This DAQ will work

perfectly for the thermal setup since, besides the coolant temperature readings (x2), each resistor will also have a thermocouple (x6). These thermocouples will measure the aluminum surface temperature and can be used to back-calculate the device junction temperature.

The last section of the thermal test setup is the DC Power supply which will supply a voltage to the resistors, creating power dissipation in the form of heat. This voltage will be regulated to various levels during testing to explore the effects on heat transfer. Measurements were taken with a multimeter to ensure the correct voltage was being supplied at all times.

6.2.2 Experimental Test Setup

Once the theoretical setup was completed, all parts needed to be sourced in real-time. All components outlined (pump, control valve, flowmeter, multimeter, power supply, pressure gauges, and thermocouples) were either found in the lab or purchased for the thermal setup. The complete experimental setup is shown in Fig. 6.6. This setup is exactly the same as the theoretical setup. Not pictured is the laptop which connects to the DAQ. The DAQ will transmit a voltage to the laptop, which will be converted to a temperature value using PicoLog. This software will measure, record, and graph all temperatures for later use.

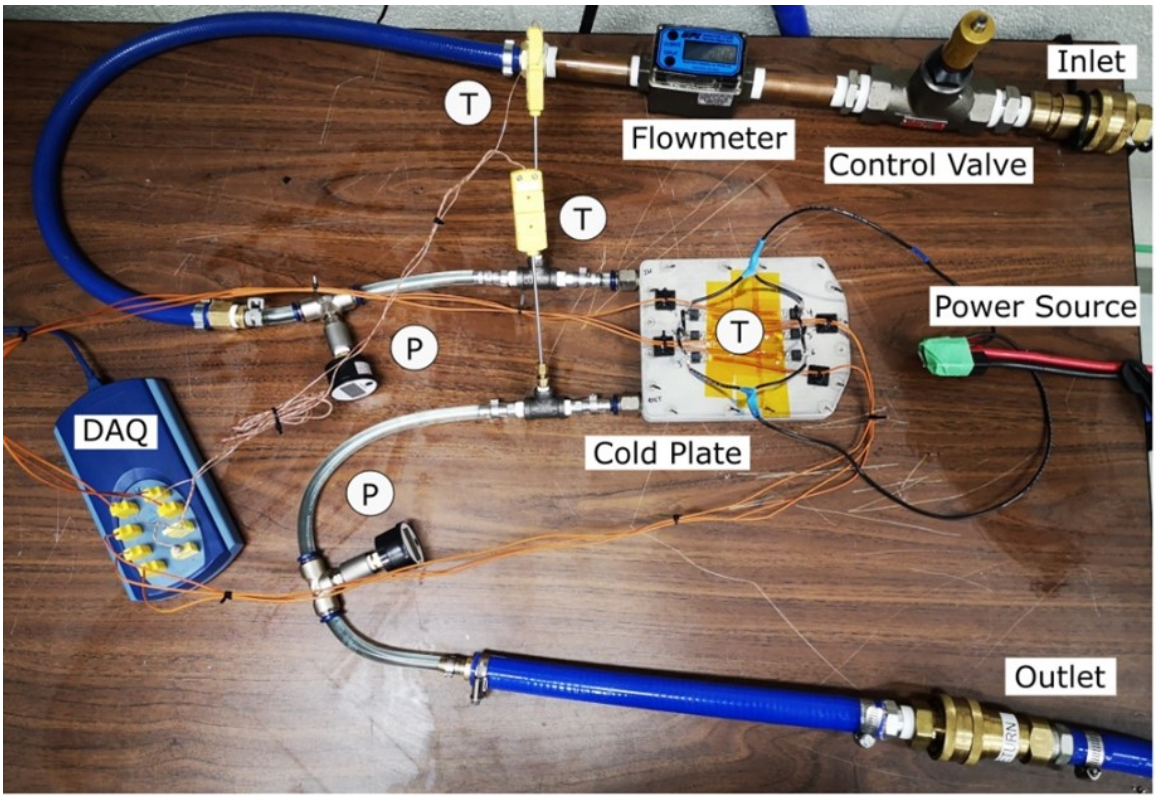

Figure 6.6: Experimental Setup

6.2.3 Experimental Results

Varying Power Dissipation Test Two basic tests were conducted to investigate the performance of the cold plate. The first test will look at the power dissipation levels of the devices. The cold plate was designed with $8.1W$ of power dissipation input and a flow rate of 12LPM. However, since this is a very low power dissipation, it will likely need to be increased to see more significant temperature changes. In this case, 8.1W will be the starting point which will be raised by roughly 10 watts at each successive test point using a 200A/80V power supply. Since the resistor can handle up to 50W (with appropriate cooling), the power input will be ramped from 8.1 to

17.78, 27.78, 37.38, and 48.4W to test the resistors' entire power range.

The cold plate will be required to reach a steady state at each power increase. A steady-state is defined as a temperature that is not changing +-0.3°C over a period of 30 minutes. Measuring to a higher precision than this would be very difficult since the temperature readings have an error of 0.2°C as calculated in Table 6.7. If this condition is met, the power dissipation will be increased to the next level. If not, measurements must be retaken at the next 30-minute interval.

The temperatures recorded follow the expected trends predicted in the full cold plate simulations (Fig. 5.12). These trends include resistors 1-3 being slightly hotter than resistors 4-6. This discrepancy goes back to the differences in fluid velocity as observed in section 5.11. This section shows that the second channel has a slightly higher fluid velocity, resulting in marginally better heat dissipation. However, this tiny temperature difference can be hard to measure accurately without specialized equipment.

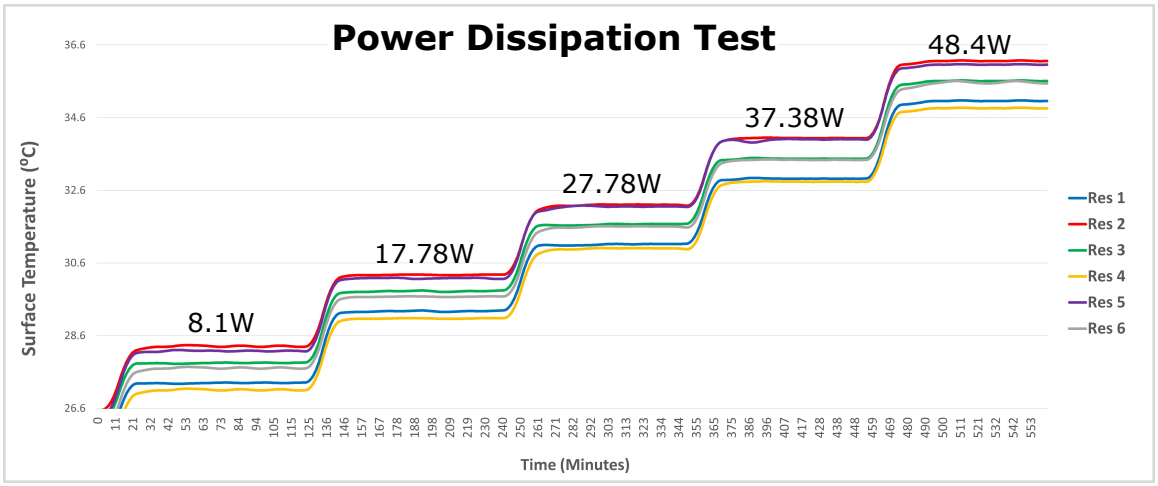

Figure 6.7: Power Dissipation Test

Channel 1 Surface Temperature (°C)			**Channel 2 Surface Temperature (°C)**			**Surface Temperature Change (°C)**		
Res 1	**Res 2**	**Res 3**	**Res 4**	**Res 5**	**Res 6**	**Res 1 & 4**	**Res 2 & 5**	**Res 3 & 6**
27.3	28.3	27.8	27.1	28.2	27.7	0.2	0.1	0.1
29.3	30.3	29.8	29.1	30.2	29.7	0.2	0.1	0.1
31.1	32.2	31.6	31.0	32.2	31.6	0.1	0.0	0.0
32.9	34.0	33.5	32.8	34.0	33.4	0.1	0.0	0.1
35.1	36.2	35.6	34.9	36.1	35.6	0.2	0.1	0.0

Table 6.2: Results - Varying Power Dissipation Test

The next trend to notice in Fig. 6.7 and Table 6.2 is that resistors 1 and 4 are typically the coldest, followed by resistors 3, 6, and then 2, 5. Resistors 3 and 6 are slightly warmer because the coolant has picked up heat from upstream resistors. Resistors 2 and 5 are the hottest because 1) the coolant has picked up heat from resistors 1 and 4, and 2) the surrounding resistors also transfer heat through the aluminum via conduction, creating a local hotspot at these resistors.

The next thing to consider is the changes in temperatures between resistors overtop of channels one and two. Resistors 1 & 4, 2 & 5, 3 & 6 will be compared to each other since they are in identical locations on the cold plate and should experience relatively equal amounts of cooling if the channel optimization is successful (section 5.2.2). However, for example, comparing resistors 1 and 6 would not be helpful since it is expected that resistor 6 would be hotter than resistor 1 because of the heat picked up from upstream resistors.

Therefore, Resistors' 1 & 4, 2 & 5, 3 & 6 temperatures must be kept relatively equal; otherwise, unequal current sharing may occur. When looking at the temperature changes between these sets of resistors, all temperature changes are $0.2°C$ or below. Anything under $2°C$ will be sufficient for this design, so the design passes this

check easily.

The coolant inlet and outlet temperatures were also recorded via the inline thermocouples. These temperatures can be found in Table 6.3. Since the cooling setup being used is a closed system, the coolant temperature slightly increases when higher amounts of power are being dissipated.

Power Dissipation (W)	**Inlet Temperature (°C)**	**Outlet Temperature (°C)**	**Temperature Increase (°C)**
8.1	26.3	26.5	0.2
17.78	26.4	26.6	0.2
27.78	26.4	26.7	0.3
37.38	26.5	26.9	0.4
48.4	26.6	27.1	0.5

Table 6.3: Coolant Temperatures

Flow Rate Test For the second test, the power dissipation will be held constant at $48.4W$, whereas the flow rate will be decreased from $\approx$ 2.5 to 0.5 gallons per minute (9.46 to 1.89LPM) in approximate 0.5GPM (1.89LPM) increments. Higher flow rates were desired; however, 9.54LPM was the maximum flow rate for this specific pump and setup. This test will study the flow rate's effect on the cooling ability of the cold plate. The cold plate resistor temperature values must stabilize at each flow rate before increasing the flow rate. Like before, a steady state is defined as a temperature that is not changing +-0.3 $^{\circ}C$ over a period of 30 minutes. If this criterion is met, the fluid will be decreased by an increment of $\approx$ 1.89LPM. Exact 1.89LPM increments were difficult to achieve due to the accuracy of the control valve. In several instances, the fluid decrease was also overshot due to the control valve sensitivity.

All surface temperature results from the flow rate test are shown in Table 6.4.

Fig. 6.8 clearly illustrates that decreasing the flow rate can significantly increase the surface temperatures. The difference in average temperature between the first case (1.82LPM) and the final case (9.54LPM) is $4.3°C$. Similar trends to Fig. 6.7 are observed in terms of which resistors are the coolest and hottest.

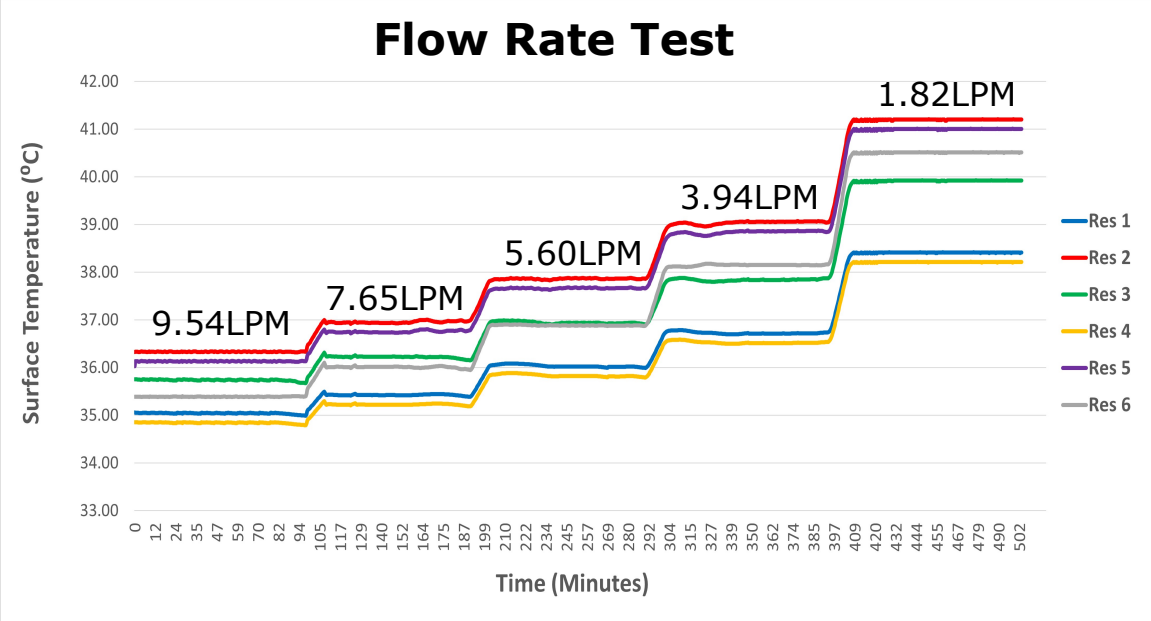

Figure 6.8: Flow Rate Test

As shown in the power dissipation test, resistors 1-3 are expected to be marginally warmer than resistors 4-6 due to a slightly lower flow rate in the first channel. Fig. 6.8 shows that this is the case for most measurements; however, resistor 6 becomes hotter than resistor 3 at high power dissipations. This effect could be due to discrepancies with the measurement system (thermocouples, connections, DAQ) or could be due to device loss of performance at high junction temperatures. These results clearly show that flow rate significantly impacts the device temperature. Therefore, for the full-sized DC-DC converter design, the flow rate will be optimized to save power while at the same time not overcooling the system (i.e., wasting energy).

Flow Rate (Litres/min)	**Channel 1 Surface Temperature (°C)**			**Channel 2 Surface Temperature (°C)**		
	Res 1	**Res 2**	**Res 3**	**Res 4**	**Res 5**	**Res 6**
9.54	35.1	36.3	35.8	34.9	36.1	35.4
7.65	35.4	37.0	36.2	35.2	36.8	36.0
5.60	36.0	37.8	36.9	35.8	37.6	36.9
3.94	36.7	39.1	37.8	36.5	38.9	38.2
1.82	38.4	41.2	39.9	38.2	41.0	40.5

Table 6.4: Results - Varying Flow Rate Test

Next, the junction temperatures are back-calculated based on the surface temperatures. This calculation is done using the thermal resistances of the thermal pad and the resistors (die-case). These values are $0.35\frac{^\circ C}{W}$ and $2.3\frac{^\circ C}{W}$, respectively. All junction temperatures are shown in Table 6.5. For the maximum power dissipation case, the resistors' junction temperatures reach $166.6^\circ C$, nearing their theoretical $175^\circ C$ limits. If considering the actual die-case resistance of the MOSFETs that will be used in future iterations, the resistance is $0.4\frac{^\circ C}{W}$, resulting in an actual maximum junction temperature of $72.5^\circ C$, well below the internal limit of $125^\circ C$.

6.2.4 Thermal Resistance

To calculate the total cold plate thermal resistance for the manufactured prototype, the junction temperatures were calculated using the surface temperatures obtained in Table 6.4. Then an average junction temperature for the six resistors was calculated. Using Eq. 4.15 the total cold plate thermal resistance values are calculated and shown in Table 6.5. These values are plotted against flow rate in Excel, and the resultant curves are shown in Fig. 6.9. This plot shows that the thermal resistance decreases when the flow rate increases since the cooling will improve at

higher fluid velocities. Plots such as this allow consumers to see if a particular cold plate will be adequate for their desired application, given a specific flow rate.

Flow Rate ($\frac{Litres}{min}$)	**Junction Temp** ($^{\circ}C$)	**Inlet Temp** ($^{\circ}C$)	**Power Dissipation (W)**	R_{j-c} ($\frac{^{\circ}C}{W}$)	R_{pad} ($\frac{^{\circ}C}{W}$)	R_{cond} ($\frac{^{\circ}C}{W}$)	**Thermal Resistance** ($\frac{^{\circ}C}{W}$)
1.82	166.6	26.6	48.4	2.3	0.35	0.00291	0.240
3.94	164.6	26.6	48.4	2.3	0.35	0.00291	0.198
5.60	163.6	26.6	48.4	2.3	0.35	0.00291	0.177
7.65	162.8	26.6	48.4	2.3	0.35	0.00291	0.162
9.54	162.3	26.6	48.4	2.3	0.35	0.00291	0.151

Table 6.5: Thermal Resistance Calculations

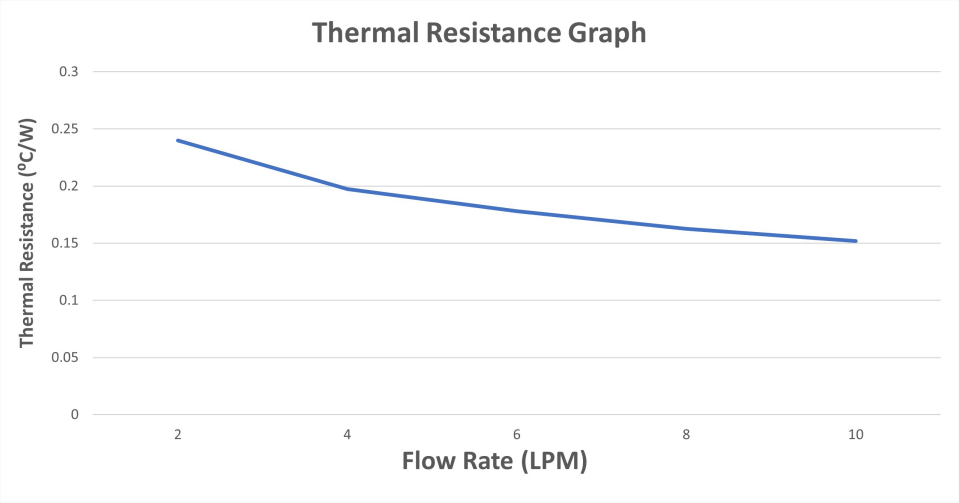

Figure 6.9: Thermal Resistance vs. Flow Rate

6.2.5 Convection Coefficient Calculation

To increase the results' accuracy and to ensure comparability between experimental and CFD results, the heat transfer coefficient was defined the same as in section

5.1.12. There were several steps taken to accomplish this calculation. First, the resultant surface temperature values were recorded, and the average surface temperature was calculated. Since in section 5.1.12 the wall temperature (T_{wall}) was used for the convection coefficient calculation, this temperature needs to be calculated. This temperature is calculated by finding the conductive resistance in the aluminum using:

$$R_{cond} = \frac{L}{KA_{cond}}, \tag{6.2}$$

where L is the thickness of the aluminum, K is the thermal conductivity of the aluminum, and A_{cond} is the conductive area through which the heat will transfer through the aluminum. The A_{cond} used in this case was the area corresponding to the top face of the channels (i.e., the base of the fins), shown in Fig. 5.15. This area must be identical to the one used for the CFD calculations; otherwise, the results could have substantial error.

Next, this conductive resistance is multiplied by the total power dissipation of the cold plate to give the temperature change. This temperature change varied for each respective power dissipation level simulated. Then the wall temperature (T_{wall}) is calculated using the average surface temperature minus this calculated temperature change. Then, this wall temperature (T_{wall}) has the inlet temperature (T_{in}) subtracted from it to find the ΔT.

Finally, the same convective area (A_{conv}) that was used in Eq. 5.1.12 was used to maintain consistency between the CFD and experimental convection coefficient definitions. Therefore, using the experimentally calculated ΔT, total power dissipation (q) and the convective heat transfer area (A_{conv}), the convection coefficient (h) can be calculated. For all power dissipation levels, the convection coefficient was calculated

and is shown in Table 6.6. An average of the five convection coefficients is calculated to give a final value of $1807.2\frac{W}{m^2K}$.

Total Power Dissipation (W)	**Wall Temperature (°C)**	**Inlet Temperature (°C)**	**ΔT (°C)**	**Convective Area (m^2)**	**Convection Coefficient ($\frac{W}{m^2K}$)**
48.6	27.6	26.3	1.3	0.01985	1899.9
106.7	29.4	26.4	3.0	0.01985	1763.8
166.7	31.1	26.4	4.7	0.01985	1780.0
224.3	32.8	26.5	6.3	0.01985	1798.7
290.4	34.7	26.6	8.1	0.01985	1793.4

Table 6.6: Experimental Convection Coefficient Calculation

6.2.6 Pressure Drop

The inline pressure gauges monitored the system's pressure drop throughout testing. The pressure drop was calculated at the 'P' points in Fig. 6.6. Additional tests had the inline pressure gauges and inline thermocouples exchange places to ensure the thermocouple fittings did not influence the pressure drop. This change ensured that the pressure drop within experiments and simulations was as close in definition and resultant values as possible. The simulations used the inlet diameter of the fittings to account for the pressure drop induced due to these fittings.

Since the flow rate remained constant throughout the heat dissipation tests; theoretically, the pressure drop should also remain constant. However, the measured inlet pressure value varies slightly between 17.8 to 18PSI (pounds per square inch). This discrepancy is likely due to pressure gauge inaccuracies since this measurement reading is limited to 0.1PSI increments. This 0.1PSI equates to approximately $689Pa$ of

pressure variations; however, since the pressure drop is ≈100,000, this slight discrepancy is negligible. The outlet pressure remains constant at 3.6PSI. These pressure values result in a pressure drop of 14.2 to 14.4PSI, equating to 97906 to 99285Pa. For all pressure drop results, see Table 6.10. This pressure drop parameter is critical since it will assist in sourcing a pump, tubing, and other components necessary for the cooling system. The higher the pressure drop, the larger the pump must be to supply the required fluid throughout the system.

6.2.7 Experimental Results vs. Simulation Results

All resistor surface temperatures from CFD simulations and the experimental tests are recorded and compared in Table 6.10. This table also compares the simulated results and the experimental results for the convection coefficient and pressure drop. For all three parameters (convection coefficient, surface temperature, and pressure drop), the resultant relative error between the two is calculated and shown in Table 6.10.

From Table 6.10, all resistor surface temperature errors fall below 10%, which is acceptable for heat transfer problems. The pressure drop error remains below 5% for all cases analyzed since the experimental pressure drop did not change for the five power levels and remained constant (relatively) during simulations. The error within the convection coefficient is higher for most cases ranging from 7.4 - 11.4%. This error occurs due to the difficulty in accurately measuring/calculating the wall temperature (T_{wall}) within the experiments. Additionally, tiny temperature changes can drastically affect this convection coefficient value, making it hard to calculate precisely. All potential reasons for the errors experienced in the results are outlined

in detail in section 6.2.8. Anything below 15% is acceptable for thermal problems; therefore, these results will be considered accurate and reliable.

		Resistor Surface Temperature (°C)						Convection Coefficient ($\frac{W}{m^2K}$)	Presssure Drop (Pa)
		Res 1	Res 2	Res 3	Res 4	Res 5	Res 6		
Simulated (CFD)	8.1W	28.4	28.6	28.4	28.3	28.6	28.4	1705.7	102528
Experimental		27.3	28.3	27.8	27.1	28.2	27.7	1899.9	99285
	Difference	1.1	0.3	0.6	1.2	0.4	0.7	194.1	3243
	Relative Error (%)	3.8	1.0	2.1	4.3	1.5	2.5	11.4	3.2
Simulated (CFD)	17.78W	30.5	31.1	30.7	30.5	31.1	30.7	1985.3	102528
Experimental		29.3	30.3	29.8	29.1	30.2	29.7	1763.8	97906
	Difference	1.3	0.8	0.9	1.4	0.9	1.0	221.5	4622
	Relative Error (%)	4.1	2.5	2.9	4.7	2.9	3.3	11.2	4.5
Simulated (CFD)	27.78W	32.7	33.6	33.0	32.7	33.6	33.0	1925.1	102529
Experimental		31.1	32.2	31.6	31.0	32.2	31.6	1780.0	98595
	Difference	1.6	1.4	1.4	1.7	1.4	1.4	145.1	3934
	Relative Error (%)	5.0	4.2	4.3	5.2	4.3	4.3	7.5	3.8
Simulated (CFD)	37.38W	34.9	36.0	35.3	34.8	36.0	35.2	1677.5	102516
Experimental		32.9	34.0	33.5	32.8	34.0	33.4	1798.7	98595
	Difference	2.0	2.0	1.8	2.0	2.0	1.8	121.2	3921
	Relative Error (%)	5.6	5.5	5.1	5.7	5.6	5.1	7.2	3.8
Simulated (CFD)	48.4W	37.3	38.8	37.9	37.3	38.8	37.8	1935.9	102528
Experimental		35.1	36.2	35.6	34.9	36.1	35.6	1793.4	98595
	Difference	2.3	2.7	2.2	2.4	2.8	2.2	142.5	3933
	Relative Error (%)	6.1	6.8	5.9	6.4	7.1	5.9	7.4	3.8

Figure 6.10: Results - CFD vs. Experiments

While 7.4 - 11.4% is an acceptable error for heat transfer problems, the convection coefficient can be averaged between the five power levels ($8.1W$, $17.78W$, $27.78W$, $37.38W$, and $48.4W$) to reduce any potential noise from the experimental measurements. This averaging results in an average convection coefficient of $1807.2\frac{W}{m^2K}$ for the experiments. After averaging, the simulated convection coefficient is $1860.5\frac{W}{m^2K}$, which gives a 2.9% error between the simulations and experiments.

Therefore, since the MATLAB and simplified CFD results match very closely (section 5.1.12), and the same methodology and boundary condition types were used in the full-sized prototype cold plate simulations, the CFD results were taken to be reliable and trustworthy. Since the full-sized prototype CFD simulations matched the experimental results well (within 12%), this verifies that the CFD, MATLAB, and experimental results all match reasonably well. Therefore this verifies (through CFD)

and validates (through experiments) the baseline cold plate design tool generated in MATLAB. As mentioned multiple times, this tool is a baseline design tool. As shown in the work of this thesis, the proposed design must be modified and optimized for the specific boundary conditions, electronic layout, and fastener locations of each particular design.

6.2.8 Uncertainty Analysis

6.2.8.1 Temperature Measurement

The thermocouples used for all experiments were calibrated using the new 9142 series calibrator. Calibration will ensure the accuracy of the results by minimizing measurement uncertainty over the range of -25°C to 150°C. The thermocouples used for measurement were all standard K-type thermocouples. All thermocouples and their wires, connectors, and other components were connected to the DAQ. Calibration then took place to simultaneously compensate for errors within the thermocouples, wire connections, and the DAQ measurement tool. The remaining errors to consider are within the RTD measurement, RTD drift, and the calibration curves.

RTD Uncertainty The manufacturer's specifications determined this uncertainty to be +-0.01°C. These results are determined based on internal testing during production.

RTD Measurement Uncertainty The manufacturer's specifications dictated that this uncertainty is +-0.01°C. These results are determined based on internal testing during production.

RTD Drift Uncertainty The paper by Drnovsek et al. details calibration methods and reducing measurement uncertainties. The paper suggests an annual drift of +- 0.0075°C in the RTD measurement [106]. The total drift is calculated over a period of 18 years, resulting in a value of +-0.135°C [107].

DAQ Uncertainty Before calibration, the DAQ has an accuracy up to 0.2% of the reading. However, this error will be compensated within the calibration process, thus eliminating it from the uncertainty analysis.

Calibration Curves Uncertainty All data was fitted in Excel during the calibration process using linear trendline equations. Other fitting methods, including polynomial and cubic fitting, were attempted, but the linear fitting proved to result in the smallest error value (R^2). This R^2 value dictates how well the trendline fits the calibrated data. A value of 0.99999 was obtained for this R^2 value (thermocouple one), which means that the output equation in Excel can correct the temperature values to a very high level of accuracy. When finding the uncertainty, the R^2 value of 0.99999 is multiplied by the maximum thermocouple one temperature within experiments (38.41°C). After subtracting this result from the original value of 38.41°C, the uncertainty for thermocouple one is 0.00004°C. Table 6.7 does not include the calibration error for the total uncertainty calculation since all values were so tiny that they were negligible. The total uncertainty within the temperature measurements is calculated to be 0.155°C. This value will be rounded up to 0.2°C, which is sufficient accuracy for this thesis.

Uncertainty	**T1** (°C)	**T2** (°C)	**T3** (°C)	**T4** (°C)	**T5** (°C)	**T6** (°C)	**T7** (°C)	**T8** (°C)
RTD Bias	0.01	0.01	0.01	0.01	0.01	0.01	0.01	0.01
RTD Measurement Bias	0.01	0.01	0.01	0.01	0.01	0.01	0.01	0.01
RTD Drift	0.135	0.135	0.135	0.135	0.135	0.135	0.135	0.135
Total Uncertainty	0.155	0.155	0.155	0.155	0.155	0.155	0.155	0.155

Table 6.7: Uncertainty Analysis

6.2.8.2 Fluid and Material Properties

Some experimental error was undoubtedly introduced into the system using water-ethylene glycol (WEG). Parameters within MATLAB and CFD assumed this coolant to be a constant 50-50 mix; however, it is difficult to tell if this was precisely the case. Although coolant was added at a 50-50, there was possibly some residue coolant in the lines changing the ratio slightly. Also, debris or other contaminants may have been present in the system, invisible to the naked eye.

Besides the coolant, the aluminum cold plate material properties may differ from those predicted/set during simulations. The distributer marketed the material as 6061 aluminum; however, it is possible this was inaccurate. Additionally, the specific properties of each piece of aluminum may vary based on the material's microstructure, so there could be some discrepancies here as well.

6.2.8.3 Flow Rate Measurement

The flow rate used for the experiments may also introduce discrepancies in the system. This flow meter is an industrial-grade FLOWMEC G2 Series Turbine Meter. This flow meter uses an internal turbine to assess the flow rate at any given time

accurately. The inaccuracy (percentage of reading) would be +-1.5% if the measurement relied only on the turbine. However, this turbine is coupled with a calibrated computer which drops this inaccuracy to +-1% of the reading.

Chapter 7

Conclusions and Future Work

This thesis aimed to take a cold plate design process from conception to completion. This process was completed successfully, and all aspects of the design, simulations, manufacturing, assembly, and experiments, are outlined in this thesis. This thesis focuses on the cold plate design tool created in MATLAB and its design capabilities. This tool can output a baseline design meant to be used as a starting point for a cold plate design. Inputs for this tool include basic parameters available to most thermal engineers before undertaking a project. These include flow rate, power dissipation, device location, number of devices, fluid and material properties, and more. After inputting these values, the tool undergoes a GA optimization process to minimize weight, pressure drop, and junction temperature and outputs an optimal pin fin configuration. The design must be refined after this based on the users' thermal knowledge, fluid dynamic principles, and applicable simulations.

In section 5.1.12, the MATLAB correlations are verified using simplified CFD simulations. In particular, the convection coefficient was the primary parameter of interest for this section. The simulated convection coefficient results match the proposed

MATLAB results to within 5%. These same boundary conditions and methodology are used to create and manufacture a full-size, prototype cold plate, which is validated experimentally. Section 6.2.3 shows that the experimental and simulated results for the convection coefficient match within 12%. The pressure drop relative error remains below 5% for all cases. Lastly, all resistor surface temperature errors remain below 8%. Therefore the MATLAB tool could be verified through CFD and validated experimentally. This three-pronged approach is an effective and robust method to solve heat transfer problems.

7.0.1 Future work

There are many different avenues to build onto the work completed within this thesis. The baseline MATLAB design tool is still in the early stages of development, and many more modifications are possible. Some possible improvements include adding additional pin fin geometry such as elliptical fins, diamond fins, tear-drop fins, and more. Also, different types of cooling methods are possible to add to the design tool. These could include straight fins, micro-channels, jet impingement, or any of the standard cooling methods discussed in chapter 2.

Another improvement to the MATLAB design tool would be to create a 3D heat transfer model instead of the current 2D model. This improvement would allow for more design flexibility and make the tool applicable for a broader range of situations. The design tool could also be improved aesthetically and with the end-user in mind by adding helpful prompts and commands to walk the user through the design phase. These changes would have been nice to make; however, time did not allow for these improvements.

Throughout the design process and based on feedback from industry professionals, several enhancements are available for the cold plate version 2.0. One improvement would be to have 100% of fins on both the cover and base plates with $\frac{1}{2}$ of the fin height (i.e., $3mm$ instead of $6mm$). This change would replace having $\frac{1}{2}$ of the fins on the cover plate and $\frac{1}{2}$ of the fins on the baseplate, reducing the surface area available for heat transfer. Another potential improvement would include a turbulator at the beginning of the channels to induce turbulence and improve the systems' heat transfer. This change is necessary because the laminar fluid flow limits heat transfer. Additionally, reductions in pressure drop should be explored (especially at the inlet/outlet fittings) to reduce the overall pressure drop and improve the fluid flow.

Future work is already being conducted in another case study for this design tool. As mentioned in the thesis, a full-sized cold plate design for a high-powered converter will be designed next using this MATLAB tool and the methodology outlined in this thesis. This design will not be part of this thesis since it will occur within the weeks/months post-graduation. However, some preliminary design work is being undertaken to create this cold plate design. Already, the functionality and applicability of the MATLAB design tool can be seen. While this design tool creation, implementation, and manufacturing took many months (even years) to create and troubleshoot, with this framework, a complete cold plate design can be completed in a matter of weeks. This streamlined effect will save countless time and money in the design and simulation phases. Additionally, lessons learned throughout manufacturing will allow this process to be refined as well.

References

[1] J. Kolar, U. Drofenik, J. Biela, M. Heldwein, H. Ertl, T. Friedli, and S. Round, "Pwm converter power density barriers," vol. 128, 05 2007, pp. P–9.

[2] A. Sundaram and R. Velraj, "Thermal management of electronics: A review of literature," *Thermal Science - THERM SCI*, vol. 12, pp. 5–26, 01 2008.

[3] E. Sparrow, J. Abraham, and P. Chevalier, "The design of cold plates for the thermal management of electronic equipment," *Heat Transfer Engineering - HEAT TRANSFER ENG*, vol. 27, 08 2006.

[4] A. da Silva Dias, D. B. Cândido, A. P. Almeida, and J. A. Alves, "Cooling Methods Design for Power Electronics Converters," in *2017 Brazilian Power Electronics Conference (COBEP)*, 2017, pp. 1–6.

[5] L. Florio and A. Harnoy, "Combination Technique For Improving Natural Convection Cooling in Electronics," *Internation Journal of Thermal Sciences*, vol. 46, pp. 76–92, 2007.

[6] M. Ahmadi, M. F. Pakdaman, and M. Bahrami, "Pushing the limits of vertical naturally-cooled heatsinks; calculations and design methodology," *International Journal of Heat and Mass Transfer*, vol. 87, pp. 11–23, 2015.

[7] A. Bar-Cohen and M. Iyengar, "Design and optimization of air-cooled heat sinks for sustainable development," *IEEE Transactions on Components and Packaging Technologies*, vol. 25, pp. 584–591, 2002.

[8] C. Hilbert, S. Sommerfeldt, O. Gupta, and D. J. Herrell, "High performance micro-channel air cooling," in *Sixth Annual IEEE Proceedings Semiconductor Thermal and Temperature Measurement Symposium*, 1990, pp. 108–113.

[9] S. S. Kang, "Advanced cooling for power electronics," in *2012 7th International Conference on Integrated Power Electronics Systems (CIPS)*, 2012, pp. 1–8.

[10] S. Song, K. P. Moran, and D. P. Rearick, "Thermal performance modeling and measurements of localized water cooled cold plate," 09 1993, pp. 69–81.

[11] P. N. Raut and P. M. P. Nawathe, "Design and analysis of liquid cooled cold plates using cad modeling," *International Journal of Trend in Scientific Research and Development - (IJTSRD)*, vol. 3, pp. 1273–1277, 2018.

[12] S. Kandlikar and C. N. Hayner II, "Liquid cooled cold plates for industrial high-power electronic devices—thermal design and manufacturing considerations," *Heat Transfer Engineering*, vol. 30, pp. 918–930, 2009.

[13] N. Sameer Mahmoud, H. Mohammad Jaffal, and A. Abdulnabi Imran, "Performance evaluation of serpentine and multi-channel heat sinks based on energy and exergy analyses," *Applied Thermal Engineering*, vol. 186, p. 116475, 2021.

[14] Q. Zhu, K. Chang, J. Chen, X. Zhang, H. Xia, H. Zhang, H. Wang, H. Li, and Y. Jin, "Characteristics of heat transfer and fluid flow in microchannel

heat sinks with rectangular grooves and different shaped ribs," *Alexandria Engineering Journal*, vol. 59, pp. 4593–4609, 2020.

[15] L. Jin, P. Lee, X. Kong, Y. Fan, and S. Chou, "Ultra-thin minichannel lcp for ev battery thermal management," *Applied Energy*, vol. 113, pp. 1786 – 1794, 2014.

[16] Y. J. Lee, P. S. Lee, and S. K. Chou, "Enhanced Thermal Transport in Microchannel Using Oblique Fins," *Journal of Heat Transfer*, vol. 134, no. 10, 08 2012.

[17] N. I. Om, R. Zulkifli, and P. Gunnasegaran, "Influence of the oblique fin arrangement on the fluid flow and thermal performance of liquid cold plate," *Case Studies in Thermal Engineering*, vol. 12, pp. 717–727, 2018.

[18] D.-Y. Lee and K. Vafai, "Comparative analysis of jet impingement and microchannel cooling for high heat flux applications," *International Journal of Heat and Mass Transfer*, vol. 42, pp. 1555–1568, 1999.

[19] C. Harris, M. Despa, and K. Kelly, "Design and fabrication of a cross flow micro heat exchanger," *Journal of Microelectromechanical Systems*, vol. 9, pp. 502–508, 2000.

[20] M. Reeves, J. Moreno, P. Beucher, S.-J. Loong, and D. Bono, "Pushing the limits of liquid cooling: Design and analysis of a direct liquid cooling system for power modules," *PCIM Europe Conference Proceedings*, pp. 519–524, 01 2012.

[21] M. Reeves, J. Quibén, P. Beucher, S.-J. Loong, and B. Dwight, "Investigation on the impact on thermal performances of new pin and fin geometries applied to liquid cooling of power electronics," *International Journal of Microscale and Nanoscale Thermal and Fluid Transport Phenomena*, vol. 3, pp. 1949–4955, 01 2012.

[22] S. J. Kim, D.-K. Kim, and H. H. Oh, "Comparison of fluid flow and thermal characteristics of plate-fin and pin-fin heat sinks subject to a parallel flow," *Heat Transfer Engineering*, vol. 29, no. 2, pp. 169–177, 2008.

[23] C. L. Chapman, S. Lee, and B. L. Schmidt, "Thermal performance of an elliptical pin fin heat sink," 1994, pp. 24–31.

[24] J. Boulares, "Numerical and experimental study of the performance of a drop-shaped pin fin heat exchanger," 2003.

[25] Tien-Yu Lee, "Design optimization of an integrated liquid-cooled igbt power module using cfd technique," *IEEE Transactions on Components and Packaging Technologies*, vol. 23, pp. 55–60, 2000.

[26] A. Al-Damook, N. Kapur, J. Summers, and H. Thompson, "An experimental and computational investigation of thermal air flows through perforated pin heat sinks," *Applied Thermal Engineering*, vol. 89, pp. 365–376, 2015.

[27] J. Schulz-Harder, K. Exel, and A. Meyer, "Direct liquid cooling of power electronics devices," in *4th International Conference on Integrated Power Systems*, 2006, pp. 1–6.

[28] E. Baker, "Liquid immersion cooling of small electronic devices," *Microelectronics Reliability*, vol. 12, pp. 163 – 173, 1973.

[29] S. Wiriyasart and P. Naphon, "Heat spreading of liquid jet impingement cooling of cold plate heat sink with different fin shapes," *Case Studies in Thermal Engineering*, vol. 20, p. 100638, 2020.

[30] ——, "Liquid impingement cooling of cold plate heat sink with different fin configurations: High heat flux applications," *International Journal of Heat and Mass Transfer*, vol. 140, pp. 281 – 292, 2019.

[31] M. Molana and S. Banooni, "Investigation of heat transfer processes involved liquid impingement jets: A review," *Brazilian Journal of Chemical Engineering*, vol. 30, pp. 413–435, 09 2013.

[32] K. Gould, S. Q. Cai, C. Neft, and A. Bhunia, "Liquid jet impingement cooling of a silicon carbide power conversion module for vehicle applications," *IEEE Transactions on Power Electronics*, vol. 30, pp. 2975–2984, 2015.

[33] E. G. Colgan, B. Furman, A. Gaynes, W. Graham, N. LaBianca, J. H. Magerlein, R. J. Polastre, M. B. Rothwell, R. J. Bezama, R. Choudhary, K. Marston, H. Toy, J. Wakil, and J. Zitz, "A practical implementation of silicon microchannel coolers for high power chips," in *Semiconductor Thermal Measurement and Management IEEE Twenty First Annual IEEE Symposium, 2005.*, 2005, pp. 1–7.

[34] X. Tang, A. Meyer, K. Schmidt, U. Voeller, and M. Goetz, "Hybrid substrate - a future material for power semiconductor modules," in *PCIM Europe 2014;*

International Exhibition and Conference for Power Electronics, Intelligent Motion, Renewable Energy and Energy Management, 2014, pp. 1–5.

[35] K. W. Jung, C. R. Kharangate, H. Lee, J. Palko, F. Zhou, M. Asheghi, E. M. Dede, and K. E. Goodson, "Embedded cooling with 3d manifold for vehicle power electronics application: Single-phase thermal-fluid performance," *International Journal of Heat and Mass Transfer*, vol. 130, pp. 1108 – 1119, 2019.

[36] S. Chen, X. Peng, N. Bao, and A. Garg, "A comprehensive analysis and optimization process for an integrated liquid cooling plate for a prismatic lithium-ion battery module," *Applied Thermal Engineering*, vol. 156, pp. 324 – 339, 2019.

[37] R. v. Erp, G. Kampitsis, and E. Matioli, "A manifold microchannel heat sink for ultra-high power density liquid-cooled converters," in *2019 IEEE Applied Power Electronics Conference and Exposition (APEC)*, 2019, pp. 1383–1389.

[38] M. März, A. Schletz, B. Eckardt, S. Egelkraut, and H. Rauh, "Power electronics system integration for electric and hybrid vehicles," in *2010 6th International Conference on Integrated Power Electronics Systems*, 2010, pp. 1–10.

[39] M. Schneider-Ramelow, T. Baumann, and E. Hoene, "Design and assembly of power semiconductors with double-sided water cooling," in *5th International Conference on Integrated Power Electronics Systems*, 2008, pp. 1–7.

[40] C. Wang, L. Zheng, L. Han, H. Fang, and J. Xu, "Thermal performance investigation of three-dimensional structure unit in double-sided cooling igbt module," in *2014 15th International Conference on Electronic Packaging Technology*, 2014, pp. 622–625.

[41] P. Ning, Z. Liang, F. Wang, and L. Marlino, "Power module and cooling system thermal performance evaluation for hev application," in *2012 Twenty-Seventh Annual IEEE Applied Power Electronics Conference and Exposition (APEC)*, 2012, pp. 2134–2139.

[42] J. Schulz-Harder, "Review on highly integrated solutions for power electronic devices," in *5th International Conference on Integrated Power Electronics Systems*, 2008, pp. 1–7.

[43] Y. Sakai, H. Ishiyama, and T. Kikuchi, "Power control unit for high power hybrid system," in *SAE Technical Paper*. SAE International, 04 2007.

[44] *Handbook of Heat Transfer*, 1998.

[45] L. Noel, G. Zarazua de Rubens, B. K. Sovacool, and J. Kester, "Fear and loathing of electric vehicles: The reactionary rhetoric of range anxiety," *Energy Research and Social Science*, vol. 48, pp. 96 – 107, 2019.

[46] *Two-Phase Minichannel Cold Plate for Army Vehicle Power Electronics*, ser. International Electronic Packaging Technical Conference and Exhibition, vol. ASME 2011 Pacific Rim Technical Conference and Exhibition on Packaging and Integration of Electronic and Photonic Systems, MEMS and NEMS: Volume 2, 07 2011.

[47] Xiaojin Wei and Y. Joshi, "Optimization study of stacked micro-channel heat sinks for micro-electronic cooling," *IEEE Transactions on Components and Packaging Technologies*, vol. 26, pp. 55–61, 2003.

[48] R. W. Knight, D. J. Hall, J. S. Goodling, and R. C. Jaeger, "Heat sink optimization with application to microchannels," *IEEE Transactions on Components, Hybrids, and Manufacturing Technology*, vol. 15, pp. 832–842, 1992.

[49] T. M. Ritzer and P. G. Lau, "Economic optimization of heat sink design," *AIP Conference Proceedings*, vol. 316, pp. 177–180, 1994.

[50] Ji Li and G. P. Peterson, "Geometric optimization of a micro heat sink with liquid flow," *IEEE Transactions on Components and Packaging Technologies*, vol. 29, pp. 145–154, 2006.

[51] A. Husain and K.-Y. Kim, "Enhanced multi-objective optimization of a microchannel heat sink through evolutionary algorithm coupled with multiple surrogate models," *Applied Thermal Engineering*, vol. 30, pp. 1683–1691, 2010.

[52] S. Qian, W. Wang, C. Ge, S. Lou, E. Miao, and B. Tang, "Topology optimization of fluid flow channel in cold plate for active phased array antenna," *Structural and Multidisciplinary Optimization*, vol. 57, pp. 2223–2232, 2018.

[53] M. Yu, S. Ruan, X. Wang, Z. Li, and C. Shen, "Topology optimization of thermal - fluid problem using the mmc-based approach," *Struct. Multidiscip. Optim.*, vol. 60, p. 151–165, 2019.

[54] E. Dede, S. N. Joshi, and F. Zhou, "Topology optimization, additive layer manufacturing, and expiremental testing of an air-cooled heat sink," *Journal of Mechanical Design*, vol. 137, 2015.

[55] J. Alexandersen, O. Sigmund, and N. Aage, "Large scale three-dimensional topology optimisation of heat sinks cooled by natural convection," *International Journal of Heat and Mass Transfer*, vol. 100, pp. 876 – 891, 2016.

[56] J. Lv, X. Jiang, G. He, W. Xiao, S. Li, D. Sengupta, and M. M. El-Halwagi, "Economic and system reliability optimization of heat exchanger networks using nsga-ii algorithm," *Applied Thermal Engineering*, vol. 124, pp. 716–724, 2017.

[57] T. A. Khan and W. Li, "Optimal design of plate-fin heat exchanger by combining multi-objective algorithms," *International Journal of Heat and Mass Transfer*, vol. 108, pp. 1560–1572, 2017.

[58] T. Wu, B. Ozpineci, and C. Ayers, "Genetic algorithm design of a 3d printed heat sink," in *2016 IEEE Applied Power Electronics Conference and Exposition (APEC)*, 2016, pp. 3529–3536.

[59] A. Michalak, "Generative design optimization of thermal management systems for high output power electronics," 2019.

[60] B. Ozpineci, L. Tolbert, S. Islam, and M. Chinthavali, "Comparison of wide bandgap semiconductors for power applications," 01 2003.

[61] B. Ozpineci and L. Tolbert, "Comparison of wide-bandgap semiconductors for power electronics applications," 12 2003.

[62] C. J. Wort and R. S. Balmer, "Diamond as an electronic material," *Materials Today*, vol. 11, pp. 22 – 28, 2008.

[63] Y. Liu, *Power Electronic Packaging*.

[64] J. Schulz-Harder, "Advantages and new development of direct bonded copper substrates," *Microelectronics Reliability*, vol. 43, no. 3, pp. 359 – 365, 2003.

[65] M. Schneider-Ramelow, T. Baumann, and E. Hoene, "Design and assembly of power semiconductors with double-sided water cooling," in *5th International Conference on Integrated Power Electronics Systems*, 2008, pp. 1–7.

[66] D. DeVoto, P. Paret, S. Narumanchi, and M. Mihalic, "Reliability of bonded interfaces for automotive power electronics," 07 2013.

[67] D. G. Pahinkar, L. Boteler, D. Ibitayo, S. Narumanchi, P. Paret, D. DeVoto, J. Major, and S. Graham, "Liquid-Cooled Aluminum Silicon Carbide Heat Sinks for Reliable Power Electronics Packages," *Journal of Electronic Packaging*, vol. 141, 05 2019.

[68] Q. Wang, X. Han, A. Sommers, Y. Park, C. T' Joen, and A. Jacobi, "A review on application of carbonaceous materials and carbon matrix composites for heat exchangers and heat sinks," *International Journal of Refrigeration*, vol. 35, pp. 7 – 26, 2012.

[69] M. Smalc, G. Shives, G. Chen, S. Guggari, J. Norley, and R. Reynolds, "Thermal performance of natural graphite heat spreaders," 01 2005.

[70] S. Klaka and R. Sittig, "Reduction of thermomechanical stress by applying a low temperature joining technique," in *Proceedings of the 6th International Symposium on Power Semiconductor Devices and Ics*, 1994, pp. 259–264.

[71] C. Göbl and J. Faltenbacher, "Low temperature sinter technology die attachment for power electronic applications," in *2010 6th International Conference on Integrated Power Electronics Systems*, 2010, pp. 1–5.

[72] S. Narumanchi, Mihalic, K. Kelly, and Eesley, "Thermal interface materials for power electronics applications," 05 2008.

[73] S. S. Kashfi, "Comparitive Analysis of Finned-Type Liquid-Cooled Power Electronic Modules for Electrified Transportation," 2021.

[74] B. A. Jasperson, Y. Jeon, K. T. Turner, F. E. Pfefferkorn, and W. Qu, "Comparison of micro-pin-fin and microchannel heat sinks considering thermal-hydraulic performance and manufacturability," *IEEE Transactions on Components and Packaging Technologies*, vol. 33, no. 1, pp. 148–160, 2010.

[75] Y. A. Altintas and A. R. Ber, "Manufacturing Automation: Metal Cutting Mechanics, Machine Tool Vibrations, and CNC Design," *Applied Mechanics Reviews*, vol. 54, no. 5, pp. B84–B84, 09 2001.

[76] A. Riemer and H. A. Richard, "Crack propagation in additive manufactured materials and structures," *Procedia Structural Integrity*, vol. 2, pp. 1229 – 1236, 2016.

[77] F. H. Kim and S. P. Moylan, "Literature review of metal additive manufacturing defects," *NIST Adv. Manuf. Ser.*, pp. 100–116, 2018.

[78] P. Cova, D. Santoro, D. Spaggiari, F. Portesine, F. Vaccaro, and N. Delmonte, "Cfd modeling of additive manufacturing liquid cold plates for more reliable power press-pack assemblies," *Microelectronics Reliability*, p. 113734, 2020.

[79] K. K. Wong, J. Y. Ho, K. C. Leong, and T. N. Wong, "Fabrication of heat sinks by selective laser melting for convective heat transfer applications," *Virtual and Physical Prototyping*, vol. 11, pp. 159–165, 2016.

[80] G. Kini, C. U. Kim, H. Madanipour, J. Y. Chang, A. Saha, A. Antoniswamy, I. Klein, M. Jorgensen, M. Ha, P. Li, B. Wondimu, and D. Kulkarni, "Corrosion in liquid cooling systems with water-based coolant – part 1: Flow loop design for reliability tests," in *2020 19th IEEE Intersociety Conference on Thermal and Thermomechanical Phenomena in Electronic Systems (ITherm)*, 2020, pp. 422–428.

[81] S. Mohapatra, "An overview of liquid coolants for electronics cooling," *Electronics Cooling*, vol. 12, pp. 1–6, 01 2006.

[82] G. G. Stefani, "Leak isolating apparatus for liquid cooled electronic units in a coolant circulation system," Patent, July 13,1993.

[83] B. Charboneau, "Double-sided Liquid Cooling For Power Semiconductor Devices Using Embedded Power Technology," 2005.

[84] B. Akselband, K. Whitenack, and D. Goldman, "Copper cold plate technology comparison," in *Thermal and Thermomechanical Proceedings 10th Intersociety Conference on Phenomena in Electronics Systems, 2006. ITHERM 2006.*, 2006, pp. 147–150.

[85] S. M. G. Cam, "Recent Developments in Friction Stir Welding of Al-alloys," *Journal of Materials Engineering and Performance*, vol. 23, pp. 1936–1953, 04 2014.

[86] W. Thomas, P. Threadgill, and E. Nicholas, "Feasibility of friction stir welding steel," *Science and Technology of Welding and Joining*, vol. 4, pp. 365–372, 1999.

[87] A. K. Lakshminarayanan, M. Suresh, and M. S. Varshan, "Thermal performance evaluation of friction stir welded and bolted cold plates with al/cu interface," *JOM*, vol. 67, pp. 1032–1044, 05 2015.

[88] H. Hori, N. Seo, and S. Makita, "Development of cold plate produced by friction stir welding," *Welding International*, vol. 25, pp. 749–753, 2011.

[89] G. K. R. M. Kumaran and T. Sornakumar, "Experimental and numerical studies of header design and inlet/outlet configurations on flow mal-distribution in parallel micro-channels," *Applied Thermal Engineering*, vol. 58, pp. 205 – 216, 2013.

[90] R. Chein and J. Chen, "Numerical study of the inlet/outlet arrangement effect on microchannel heat sink performance," *International Journal of Thermal Sciences*, vol. 48, pp. 1627 – 1638", 2009.

[91] M.-C. Lu and C.-C. Wang, "Effect of the inlet location on the performance of parallel-channel cold-plate," *IEEE Transactions on Components and Packaging Technologies*, vol. 29, pp. 30–38, 2006.

[92] H.-L. Wang, H.-C. Wu, S. Kong Wang, T.-C. Hung, and R.-J. Yang, "A study of mini-channel thermal module design for achieving high stability and high capability in electronic cooling," *Applied Thermal Engineering*, vol. 51, pp. 1144 – 1153, 2013.

[93] N. S. P. Gunnasegaran, H.A. Mohammed and R. Saidur, "The effect of geometrical parameters on heat transfer characteristics of microchannels heat sink with different shapes," *International Communications in Heat and Mass Transfer*, vol. 37, pp. 1078 – 1086, 2010.

[94] J. S. Y. E. S. Cho, J. W. Cho and M. S. Kim, "Experimental study on microchannel heat sinks considering mass flow distribution with non-uniform heat flux conditions," *International Journal of Heat and Mass Transfer*, vol. 53, pp. 2159 – 2168, 2010.

[95]

[96] X. Liu and J. Yu, "Numerical study on performance of mini-channel heat sinks with non-uniform inlets," *Applied Thermal Engineering*, vol. 93, pp. 856–864, 2016.

[97] X. Peng, D. Li, J. Li, S. Jiang, and Q. Gao, "Improvement of flow distribution by new inlet header configuration with splitter plates for plate-fin heat exchanger," *Energies*, vol. 13, p. 1323, 03 2020.

[98] F. Incropera, D. Dewitt, T.L.Bergman, and A. Lavine, *Fundamentals of Heat and Mass Transfer*. John Wiley and Sons, 2007.

[99] A. Konak, D. W. Coit, and A. E. Smith, "Multi-objective optimization using genetic algorithms: A tutorial," *Reliability Engineering System Safety*, vol. 91, pp. 992–1007, 2006.

[100] F. Zhou, E. M. Dede, and S. N. Joshi, "A novel design of hybrid slot jet and mini-channel cold plate for electronics cooling," in *2015 31st Thermal Measurement, Modeling Management Symposium (SEMI-THERM)*, 2015, pp. 60–67.

[101] E. M. Dede, "Single-phase microchannel cold plate for hybrid vehicle electronics," in *2014 Semiconductor Thermal Measurement and Management Symposium (SEMI-THERM)*, 2014, pp. 118–124.

[102] F. Zhou, Y. Liu, Y. Liu, S. N. Joshi, and E. M. Dede, "Modular Design for a Single-Phase Manifold Mini/Microchannel Cold Plate," *Journal of Thermal Science and Engineering Applications*, vol. 8, 12 2015.

[103] n.a, "Global o-ring and seal." [Online]. Available: https://www.globaloring.com/o-ring-groove-design/

[104] M. Sedighi, D. Afshari, and F. Nazari, "Investigation of the effect of sheet thickness on residual stresses in resistance spot welding of aluminum sheets," *Proceedings of the Institution of Mechanical Engineers, Part C: Journal of Mechanical Engineering Science*, vol. 232, pp. 621–638, 02 2018.

[105] T. Adams, C. Grant, and H. Watson, "A simple algorithm to relate measured surface roughness to equivalent sand-grain roughness," *International Journal of Mechanical Engineering and Mechatronics*, vol. 1, 01 2012.

[106] J. Drnovsek, I. Pusnik, and J. Bojkovski, "Reduction of uncertainties in temperature calibrations by comparison," *Measurement Science and Technology*, vol. 9, pp. 1907–1911, nov 1998.

[107] Y. Hana, "A Characterization of Flat-Plate Heat Exchangers for Thermal Load Management of Thermoelectric Generators," 2014.